Drew University
College of Liberal Arts
In collaboration with Purdue University

Design and synthesis of novel pyridine-based conjugated ligands for 2D perovskite formation and improved solar cell efficiency

A Thesis in Chemistry

by

Aline Carla Krüger

Submitted in Partial Fulfillment
of the Requirements
for the Degree of
Bachelor in Science
With Specialized Honors in Chemistry

December 2023

Abstract

One of the most pressing needs of the twenty-first century is to explore and optimize the use of renewable energy sources, among them solar energy. Current methods to harvest sunlight into usable electricity come as solar panels, which are made from different semiconductor materials, for example silicon. However, other materials, such as metal-halide perovskites have interesting electronic properties that set apart them as one of the most promising candidates in the next generation of photovoltaics. This thesis focuses on the optimization of such materials so that more efficient solar panels can be produced. Structurally, metal-halide perovskites are composed of a general ABX_3 lattice, in which the A and B sites are small organic and metal cations, respectively, while the X is a halogen. Derived from them is a new class of materials called hybrid or 2D-perovskites that have their A-site occupied by a large and conjugated organic ligand. They have yielded solar cells with better environmental resistance compared to traditional perovskites but still output lower overall power. Thus, one major area of research focuses on the substitution of different ligands to optimize these materials' efficiencies rendering them more attractive in modern solar panels. In this research, a series of four novel pyridine-based ligands was designed and synthesized. And with the desired ligands in hand, 2D-perovskites were assembled and characterized by X-ray diffraction, absorption and emission spectroscopy. The UV absorption spectra displays new peaks, indicating that novel hybrid perovskites were produced which is agreement with photoluminescence and crystallography findings. In addition, solar cell devices were built and their electronic characterization shows promise. These results indicate that the pyridine-based ligands are tolerated in the perovskite lattice and that formation of desired hybrid materials is observed. These new derivatives contribute to the expansion of the ligand library available for 2D perovskites and to the search for the best efficiency of solar cell devices.

Table of contents

List of Figures

List of Tables

Acknowledgements

I would like to express my deepest appreciation to Dr. Letian Dou, in the Department of Chemical Engineering at Purdue University. I am thankful for the opportunity to work in your laboratory in the Summer of 2023 and for your consent that I was allowed to use the data generated there as my undergraduate thesis at Drew University.

But, this journey would not have been possible without Jiaonan Sun, from the Department of Chemical Engineering at Purdue University. I would like to voice my uppermost respect and admiration for your mentoring over the Summer since without your guidance and trust, I would not have been able to produce this thesis. Additionally, I acknowledge her work in fabricating and characterizing the thin films and solar cells devices used in this study and I am thankful that some of the data for these devices was so readily shared. Without them, the synthesis of these novel pyridine-based ligands would suffer from a lack of context, making it harder to understand the significance of this work.

I am deeply indebted to Dr. Brian McKittrick, RISE Fellow at Drew University. Without your patience and advice, I would not have developed the laboratory skills that allowed me to make this project come true. Your presence in this Thesis Committee, even after I decided to switch topics, means more than what words can express.

Lastly, I could not be the chemist I am today without Dr. Mary-Ann Pearsall, Professor of Chemistry at Drew University. I am forever grateful for our many orbital conversations and the skills you've taught me throughout my time at Drew. And thank you so much for making me take Inorganic Chemistry early on. It changed my life for the better.

Glossary

ETL - Electron-Transporting Layer. The electron-rich compounds used to create these layers in solar cell devices work as n-type materials in a p-n junction.

FA - formamidinium ion. A small organic cation whose structure is displayed below.
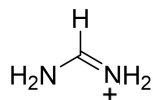
Figure 1: Structure of the formamidinium ion

FF - Fill Factor. See section 2.5 for electrical definition and equations.

HTL - Hole-Transporting Layer. The electron-deficient compounds or highly conjugated polymers used to create these layers in solar cell devices work as p-type materials in a p-n junction.

IPA - isopropyl alcohol

J_{SC} - Short Circuit current density. In physics, J is the letter designated to present current density and has the units of Ampère per square meter. See section 2.5 for electrical definition and equations.

LCAO - Linear Combination of Atomic Orbitals

Ligands - In this study, the term ligand is used to uniquely define the bulkier and conjugated cations that occupy the A-site valence in 2D-perovskites. Note that this is a different definition than what is usually implied by the term ligand in other areas of Chemistry. Figure 2 denotes the placement of the ligands, as defined in this study.

2D perovskite

A site – bulkier and conjugated organic cations
whose organic "tail" is known as **ligand**
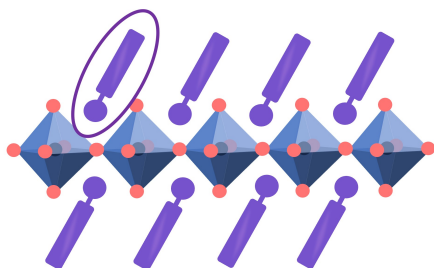
Figure 2: Schematic of what is implied by the term "ligand" in this study. Note that this is a much different meaning of the term compared to other areas of Chemistry.

MA - methyl ammonium. A small organic cation whose structure is displayed below.

$$H_3C-\overset{+}{N}H_3$$
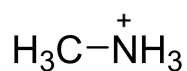
Figure 3: Structure of the methyl ammonium ion

MO - Molecular orbital

NMR - Nuclear Magnetic Resonance

PCE - Power Conversion Efficiency. See section 2.5 for electrical definition and equations.

PL - Photoluminescence. A type of emission spectroscopy technique.

PSC - Perovskite Solar Cell

V_{OC} - Open Circuit voltage. See section 2.5 for electrical definition and equations.

XRD - X-ray diffraction

1 Introduction

1.1 Solar energy

The Industrial Revolution, as fundamental as it was for the development of large-scale production and commercialization of goods, set in motion the exacerbated consumption of non-renewable fossil fuels. At the time, the burning of coal into the atmosphere was the major form of energy generation at the cost of producing concerning amounts of carbon dioxide and other harmful gases. The issue was aggravated in 1875 upon the discovery and subsequent use of another non-renewable and pollutant type of fossil fuel: petroleum.
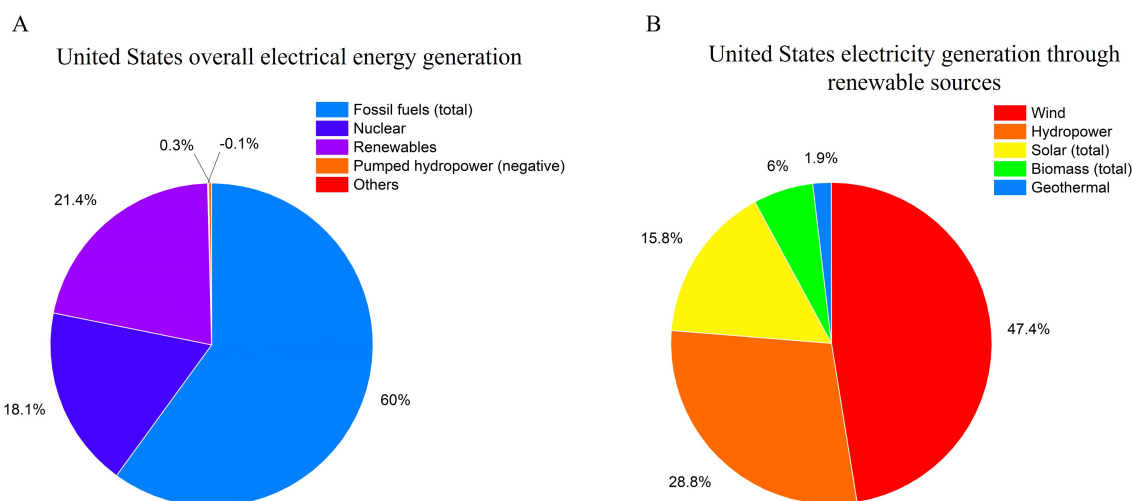
Figure 4: United States electrical energy generation. A) Electrical energy generation distribution of the Unites States. Pumped hydropower is displayed as negative, since they still require more energy input compared to what they can produce. Values add up to around 100 % due to rounding error. B) Breakdown of electricity generated by renewable renewable energy sources only. Solar is composed of both photovoltaics and thermal; biomass is composed of wood, landfill gas, Municipal solid waste (biogenic) and other forms of biomass waste. These percentages are based on 2022 data, lastly updated on February 2023, from the U.S. Energy Information Administration (EIA). [1]

While production systems have significantly changed throughout time, most the materials used to power industry, commerce, aviation, transportation and urban life in general still come from non-renewable sources, among them natural gas, coal and petroleum. For example, the United States, one of the major consumers of energy in the world, has an electricity generation distribution profile mostly based on these energy

sources, as displayed in Figure 4.

The most concerning consequence of consuming pollutant and non-renewable fuels is climate change, as strongly evidenced by research [2, & references therein]. And some of the consequences are the rising of the global temperature, thawing of the glaciers and as demonstrated in August 2023, the worsening of the wildfires in Canada [3, 4]. It is especially frightening to know that July 2023 has been the hottest July ever recorded on the planet to date (November 2023), according to the monthly NASA report [5, 6]. It becomes clear then, that the world faces an energy crisis, since the fuels that provide most of the energy supply world-wide are precisely those that cause the dreadful consequences of climate change. Given this scenario, it is critical to explore and further develop alternative forms of energy supply. Especially, those coming from renewable and greener sources.

Renewable energy can come from several sources, such as the wind, sun, water, leftover organic residues (also known as biomass), atomic collisions (nuclear energy) and even from the heat generated by the Earth (geothermal energy). Most exciting, though, is the fact that these sources are already important contributors to the production of energy globally and their use has consistently increased, likely due to the need to troubleshoot and remediate some of the consequences caused by climate change. For example, in 2020, renewable sources amounted up to 12 % of the United States overall energy usage [7], a percentage that had consistently increased for half a decade.

This work focuses on solar energy, in which sunlight is directly harvested to produce electrical current and usable power. There are many benefits to using this kind of energy but the most important one is the reduction of greenhouse gases production [8]. In addition, other pros are employment generation, due to construction, installation and sales of solar panels, increased property value of facilities, low operational cost compared to fossil fuel-based engines, and even financial benefits are in place. For instance, in the the United States, citizens that installs solar panels in their homes are allowed to file a tax credit form, in which up to 30 % of the solar panel cost is deducted in any leftover tax payments [9]. This is known as Solar Investment Tax Credit (ITC).

However, even with all these benefits, in 2020 only 1.3% of the United States' total energy use came from the sun [7]. Other issues that the solar technology faces is that financial return from the initial investment still takes considerably long to pay off and larger patches of land are often necessary to install the panels, especially if a more robust energy supply is desired [8]. Additionally, solar panels can degrade rapidly due to their constant exposure to unstable weather conditions and there are also negative environmental consequences considering improper battery disposal (required to store the energy produced within the panels). But, the future of solar energy is bright, if taking into account the US Energy Information Administration's prediction that by 2050, it will, alone, produce 20 % of the country's total electricity [10]. Therefore, it is clear that solar energy has a great potential among the other renewable sources, to at least partially substitute fossil fuel usage and contribute to a greener environment.

The idea of using the sun as an energy source, however, is surprisingly old. There are registers of the use of sunlight for heating and cooling of households that can be traced back to Egyptian and Greek societies [11, 12]. These techniques, however, are passive forms of energy use [8] and cannot output any viable work. But, in 1883, the first solar panel, and hence attempt to actively transform sunlight into useful electricity, was developed by the engineer Charles Fritts [12]. The resulting materials, even though underdeveloped, promoted the idea that this intentional energy transformation was possible.

After Fritts, the major push for solar energy started out in the 1950s and was spearheaded by the company Bell Laboratories, in the state of New Jersey, US. There, the physical chemist Calvin S. Fuller, electrical engineer Daryl Chapin and experimental physicist Gerald Pearson created the first silicon-based solar panel that was able to produce viable work, truly harvesting the sun's energy [13]. What was so interesting in their design was precisely the use of a silicon-based material which, as discovered by Fuller, needed to be doped in order to drive current and energy flow. But still, they only achieved small power conversion efficiencies, around 4 %, out of a 30 % theoretical maximum [14].

With time, many of the issues that were faced in the 50s were addressed, and now

solar panels, especially those silicon-based, have reached market quality and are sold world-wide. However, as noted before, they are still expensive and silicon is not the only semiconductor that can be designed to harvest energy from sunlight. Other materials, for instance, hybrid and inorganic perovskites, quantum dots (which won the Nobel prize in 2023!), organic thin films and other semi-metal combinations (GaAs, most famously), have been explored as alternatives to silicon [8]. And it is important to keep researching for more efficient, cheaper and more easily accessible materials, considering the pressing needs of cleaner energy sources in the dawn of the consequences of climate change.

This thesis aims to continue the exploration of one of those candidates: perovskites. They have attracted considerable interest in the field, since their semiconducting properties can be matched to harvest sunlight and have the potential to be more cheaply manufactured in large scale productions [15]. Their electronic and chemical structure, function and all associated chemistry involving shaping this material for better solar energy generation will be detailed in the sections to follow.

1.2   Band structures - derivation and properties

Before jumping into perovskites themselves, a brief introduction to solid state physics (but viewed through the eyes of Chemistry), conductors and semiconductors is necessary. This will allow one to understand the general bonding principles and the behavior of electrons in solids and how these interactions lead to physical and electronic properties that render different materials semiconducting.

Solid state physics faces a big challenge, compared to organic and inorganic chemistries. That is, chemists are more traditionally concerned with individual molecules, the types of bonds that happen within them, possible intermolecular forces and more importantly, the transformations of these bonds in reactions. In solid-state physics this molecular framework is no longer capable of grasping the size of the structures under investigation, since atoms or ions will arrange themselves in a repeating and continuous pattern, called a solid lattice, becoming much larger than a molecule. This recurrent arrangement will lead to a vastly different bonding scheme, known as the band structure. This concept is central to the field of solid state physics (or to any chemist working in materials science), since the electronic properties of different materials will emerge from the different configurations and relative energy of these bands.

However, bands are significantly different from isolated molecular orbitals, with respect to their energy densities, size and properties, hence calling for other models that are capable of handling them. To date, there are two main approaches that can be used to understand this alternate bonding in solids: the tight binding [16, 17] and the nearly free electron [17, 18]. The latter is routinely used by physicists and focuses on the properties of the unit cell, the smallest repeating unit of the solid in real space, its correspondent Brillouin zone (which lives in reciprocal space) and can generate a robust description of the bonding scheme in solids. However, it requires great physical and mathematical sophistication which is not necessary in this study and are less appealing to chemists, as they do not directly use the atomic orbitals or key chemical concepts such as bond

strength and electronegativity. Therefore, the tight binding approach will be used in this study to promote the idea of bonding in solids as an expansion of molecular orbitals, with the recognition that it might not account for all observed phenomena in solid-state materials.

1.2.1 Conductors

It is simpler to begin thinking about and deriving band structures from the perspective of metal conductors, in which the same atoms are arranged side by side in solid state. Therefore, their atomic orbitals are also juxtaposed and will closely interact with each other in the following manner.
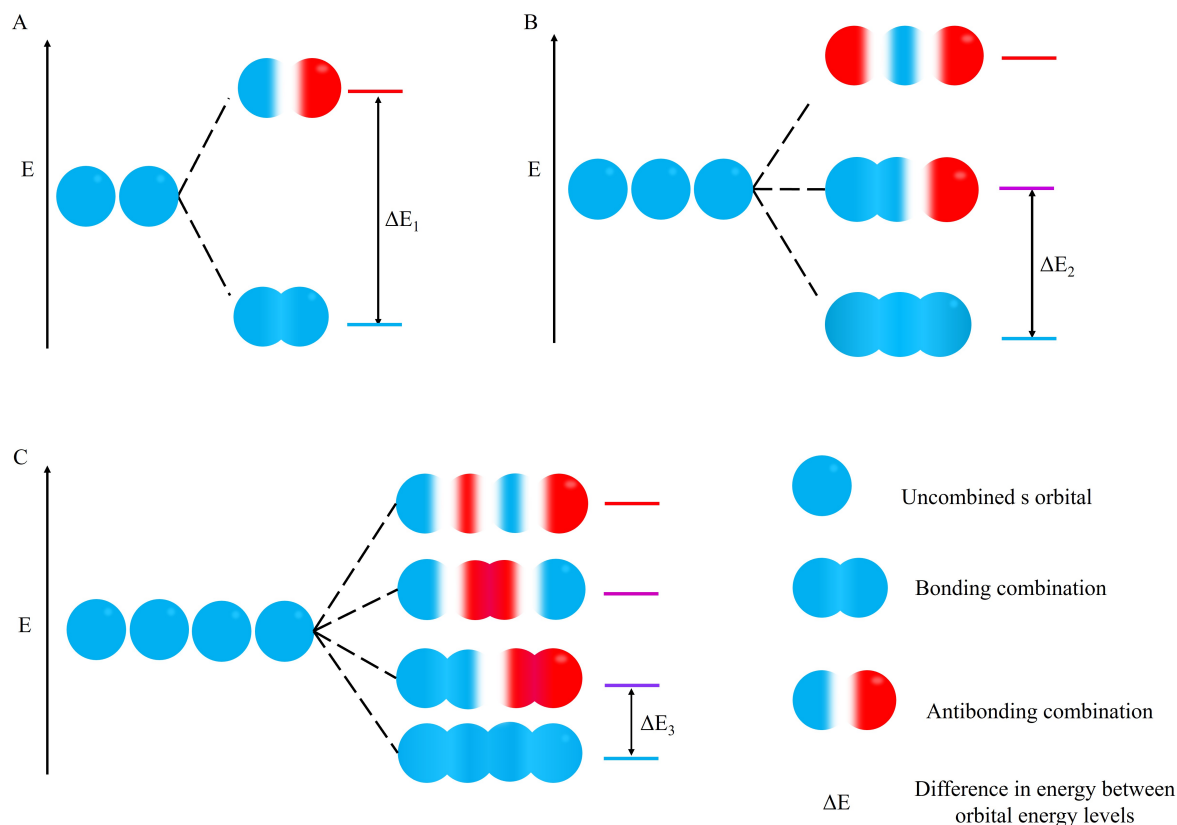
Figure 5: Molecular orbital diagrams showing the consecutive overlap of s atomic orbitals in a conductor [16, 17]. A) Two s orbitals combine to generate 2 molecular orbitals (MOs): one bonding and one antibonding combination with different energy levels, following the principle of the linear combination of atomic orbitals (LCAO). B) Three s orbitals combine to form thee MOs: one bonding, one antibonding and one intermediate in energy, all which occupy discrete energy levels. C) Four s orbitals combine to form four MOs: bonding, antibonding and intermediate combinations also with discrete energy levels. But note that the energy gap between the MOs decreases as more s orbitals are added to the scheme.

Let's take for example, the simple overlap between two of the same s-type orbitals, shown in Figure 5A. As determined by the principle of linear combination of atomic orbitals (LCAO), the two initial s orbitals yield two molecular orbitals (MOs) that have different phases and energy levels [19]. In the first combination, the two orbitals interact

in phase with each other (constructive interference) and yield a MO that is lower in energy, hence stabilized compared to the starting s orbitals. This is known to be the bonding combination. In the second scenario, the orbitals interact out of phase with each other (destructive interference) leading to a node (area in which no electron can be found) in the MO. Since this interaction is not beneficial for electron stabilization, the MO is higher in energy and the electrons are considered destabilized compared to the starting s orbitals. This combination is known as anti-bonding. These two bonding and anti-bonding orbitals are the only possibilities, as determined by LCAO, since 2 atomic orbitals can only yield 2 molecular orbitals.

However, more s atomic orbitals can be added at the start. Figure 5B shows the combination process involving three of them. Similarly, one bonding and one antibonding combination are created and they are even more stabilized or destabilized, respectively, since both constructive and destructive interferences increase. However, the principle of LCAO indicates that three molecular combinations must be obtained [19]. The last one is generated when two of the orbitals interact in phase while the third one is out of phase, introducing only one node, compared to two in the most anti-bonding combination. Note that the energy level of this orbital lies in between those of purely bonding and anti-bonding combinations since it carries both characteristics. Due to the presence of the intermediate energy MO, the energy gap between sequential MOs decreases (only partial anti-bonding character is acquired when jumping to the next MO higher in energy).

If using four s atomic orbitals, as shown in Figure 5C, 4 MOs would be generated: one, the lowest in energy, completely stabilized by all in-phase interactions, two of them with intermediate energies with one and two nodes, and finally, the last is the most destabilized, with three nodes in total. However, note that the energy difference between sequential MOs is further decreased since overall change in the anti-bonding character of the orbitals as one goes up in energy decreases. In other words, introducing one node, when a total of three are possible (Figure 5C), is a less dramatic change in energy compared to one node being introduced when it is the only possible destructive interference in the MO (Figure
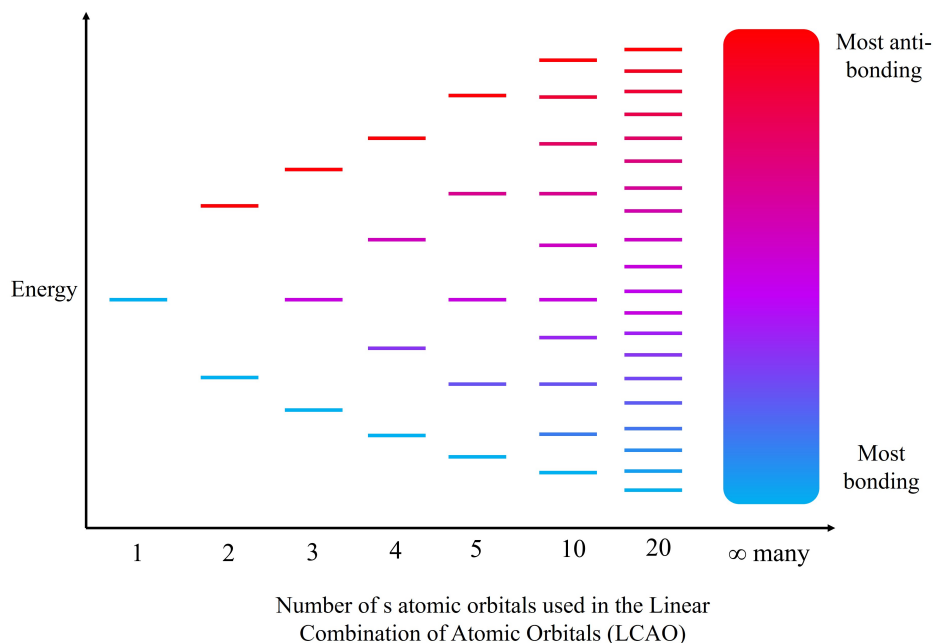
Figure 6: Generation of band structure in conductors using the tight-binding approach [16, 17]. When only two, three or four s atomic orbitals are used in the combination process, the resulting MOs have the same energy levels as described in Figure 5A, B and C, respectively. However, as more atomic orbitals are added at the beginning, more intermediate energy MOs are created to obey the LCAO. This causes the relative stabilization of the fully bonding combination to progressively increase, (greater constructive interference), while the fully anti-bonding combination destabilization increases in energy (placement of more nodes - more destructive interference). And most importantly, it shrinks down the energy gap between sequential MOs. If infinitely many orbitals are combined, the energy levels become so similar, that they are virtually indistinguishable, creating one continuous band. Color scheme: blue - most bonding, stabilized and lower in energy; red - most antibonding, destabilized and higher in energy; purple - partial bonding and antibonding characteristics and intermediate in energy. Only the relative energy levels are shown (and not the pictograms of the MOs) for clarity.

5A).

The linear combination process still applies when five, ten or twenty atomic orbitals are used, as summarized in Figure 6, and hence they yield the respective number of molecular orbitals. Naturally, the overall stabilization and destabilization of the MOs fully in phase or out phase grows but most importantly, many more intermediate in energy MOs are added. Consequently, the difference in energy between them shrinks even more. If one supposes that infinitely many atomic orbitals are combined, which is in fact a situation very similar to that of large solid structures when millions of atoms are involved, then it is reasonable to say that the difference in energy between the molecular orbitals will become so small that MOs are essentially indistinguishable! At that point, it is much easier

and accurate to think as the energy levels not as discrete units, but as one continuous electronic band.

Therefore, from a Chemistry perspective, the electronic band in conductors is generated by the interaction of many atomic orbitals from the conductor atoms, creating many and virtually indistinguishable in energy molecular orbitals. That is, there is a smooth and continuous increase in energy of the MOs generated in a conductor lattice. A quick note: the process of band structure generation should take into account the overlaps of all s, p and d orbitals available in the conductor atoms in three dimensions, but a simplification was used here to convey more directly the idea that discrete energy levels will eventually generate a uniform electronic band when analyzing a solid conductor lattice.

However, this process should sound quite amazing, since, in conductors, the electrons are no longer localized in one single bond or molecular orbital. Consequently, they essentially span the whole solid (if no defects in the lattice) and, while the electrons occupy the lowest energy states available in the band (purely stabilization criteria), they can be quite effortlessly excited, as there is no longer a HOMO-LUMO gap to be crossed. In addition, the ground state electron configuration of most metals generates by default, partially filled bands, fulfilling the requirement for conduction. Both of these effects combined give metals the capability of seamlessly conducting current.

This approach toward band structures generates a useful foundation for the development of semiconductor bands in the following section.

1.2.2 Semiconductors

In semiconductors, the process of juxtaposing atomic orbitals and generating MOs with intermediate energies is again employed, but this time the idea of bond strength and electronegativity difference should be factored in when considering the fist few overlaps, especially because two different atoms are involved. This will help generate a key feature in semiconductor band structure: the band gap.
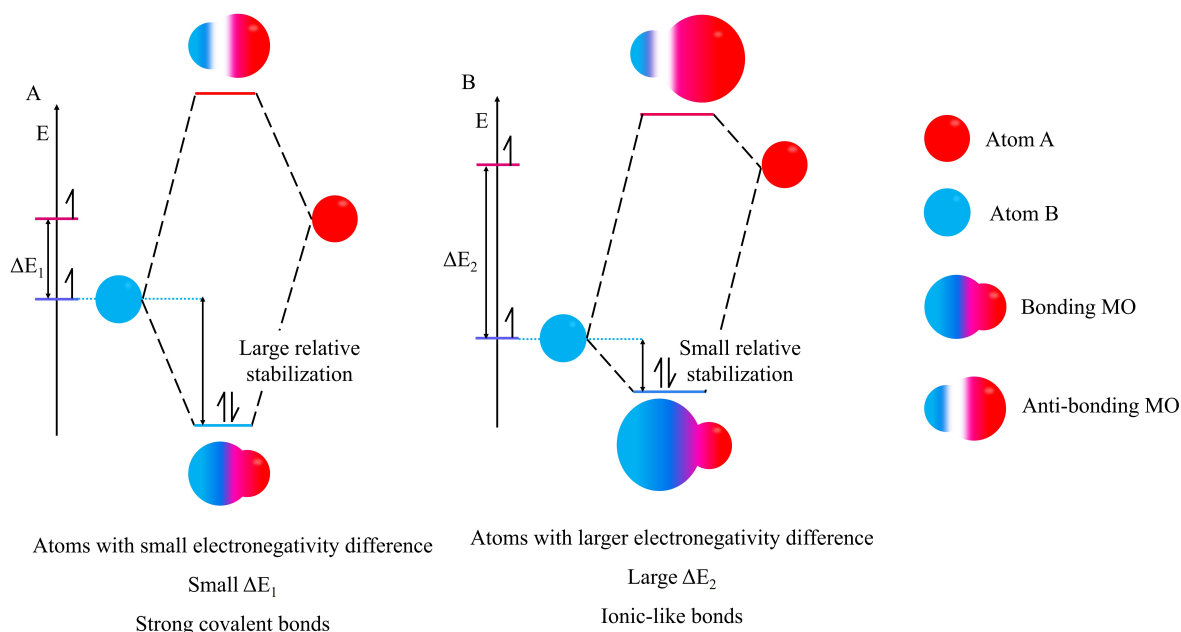
Figure 7: Molecular orbital diagrams contrasting covalent and ionic bonds. Panel A shows the MO diagram for a strong covalent bond in which atoms with similar electronegativities generate bonding combinations that are well stabilized. The overall electron densities of the resulting MOs are quite evenly shared. Panel B shows the formation of an ionic bond, in which the atoms possess a larger electronegativity difference - or their valence orbitals are energetically far apart. Their interaction leads to MOs that are poorly stabilized, almost to the point that the they seem to occupy the same energy level of the valence orbitals. The MOs also have significantly different electron density contributions: the valence orbital closest in energy to either the HOMO or LUMO donates the greater amount of the resulting electron density. This effect is given by the size of the electron cloud.

Let's consider a bond between atoms A and B. If the energy difference between their valence orbitals is small or the atoms have a small electronegativity difference, as represented in Figure 7A, then the overlap between the orbitals is very effective, generating a strong covalent bond [19]. This is implied in a molecular orbital diagram by a large stabilization of the bonding HOMO, whose overall electron density is almost an even mix

of the electron density of the starting atomic orbitals. Conversely, the LUMO is also significantly destabilized and its electron cloud is composed of the combination of the remaining electron density available from each atom (almost evenly shared as well).

However, if the energy difference between the valence orbitals is large (or large electronegativity difference), then the overlap of the orbitals is not as effective and the bond is most likely ionic [19], as in Figure 7B. Therefore, the HOMO is only poorly stabilized and most of its the electron density belongs to the atom who has the stronger electronegativity (atom B in this scenario). As no meaningful stabilization took place, the LUMO is also only slightly destabilized and its electron density is mostly composed of the atomic orbital of the least electronegative atom (atom A in this scenario). However, a key idea in ionic bonding is that the energies of the HOMO and LUMO are very close to the respective atomic orbitals who donated most of their electron densities. In practice, this means that when the ionic bonding is formed and the electrons from the valence orbitals of A fall into the HOMO, they essentially occupy the same energy level as the valence atomic orbitals of atom B.

If four atoms, two highly electronegative (atom B) and two less electronegative (atom A), are used to construct sequential ionic bonds of the form B-A-B-A, then they generate four molecular orbitals, following the principle of LCAO, as shown in Figure 8. The two more stabilized MOs have energies very similar to the starting valence orbital of the more electronegative atom B (blue - lower energy), while the two more destabilized have energies close to the starting valence orbital of the least electronegative atom A (red - higher energy). Note that the difference in electron density contributions observed in Figure 7 is maintained.

In many solids materials, perovskites included, the lattices are ionic and hence, individual bonds follow the bonding description highlighted in Figures 7B and 8. But, as seen before with conductors in section 1.2.1, one must account for the repetition of the orbitals in space, since the materials expand in three dimensions. This process is highlighted in Figure 9. And interestingly, the final band structure for semiconductors is
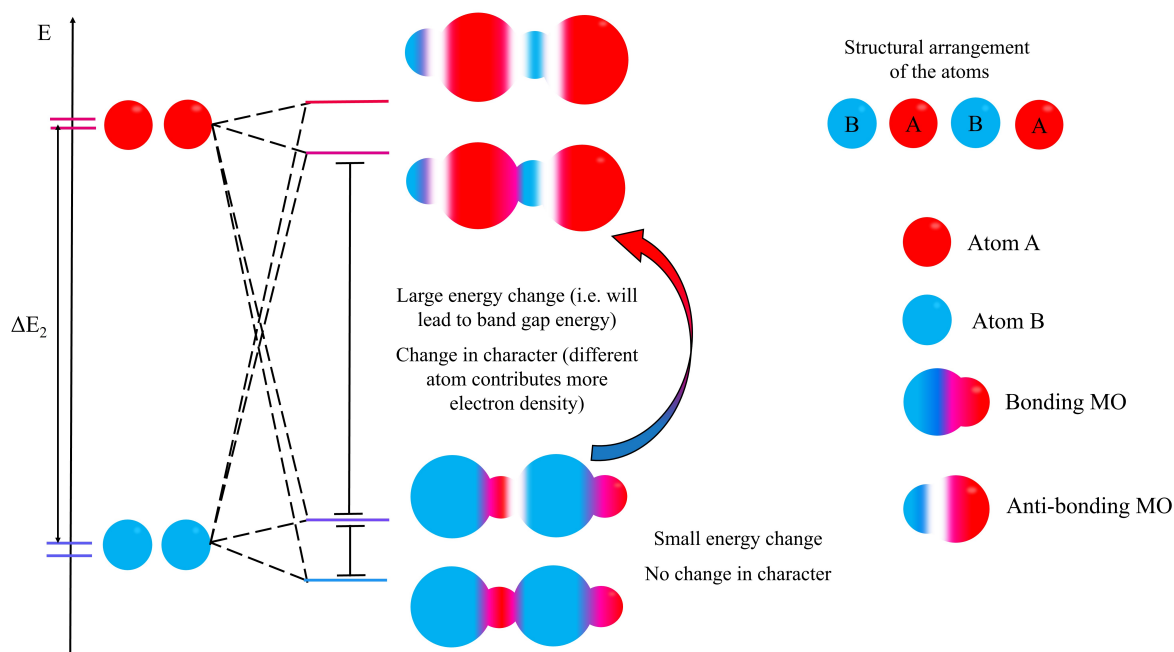
Figure 8: Display of four atom engaging in ionic bonding. When four atoms engage in bonding (B-A-B-A atom sequence), their valence orbitals generate four MOs, following the ideas displayed in Figure 7B. However, these MOs do not become energetically evenly distributed, since their overall electron clouds receive different contributions of electron density from both valence orbitals. The closest in energy valence orbitals contribute the most. Therefore, a small gap is formed within the MOs closest in energy to the more electronegative atom (introduction of node) and the same applies for the two MOs higher in energy, which experience greater electron density donation from the valence orbitals of the least electronegative atom. However, there is a large energy gap (will lead to band gap energy) between these two sets. This happens because the overall electronic character of the MOs change from electronic dispersion within MOs that are made primarily of electron density donated from the most electronegative atom (blue) to MOs that have electron density primarily donated from the least electronegative atom (red).

very different compared to the previous result for conductors due to the creation of *two* bands instead of one.

The key difference in this derivation (Figure 9 is that even as more atomic orbitals are added to the starting pool, the resulting intermediate MOs cannot fully bridge the energy gap created by the large initial separation of the valence atomic orbitals (ΔE_2). Moreover, the very nature of the ionic bond being the result of ineffective (but still existent) overlaps of the valence orbitals leads to molecular orbitals that are relatively similar in energy to each other since they share the same kind of electron density dominance (i.e. all the bonding MOs have their primary electron density coming from the most electronegative atom). In contrast, there is a more significant energy transition (the band gap!) when

But the bigger picture is that these overlaps create two bands, separated by the band gap energy. This gap is crucial in determining the material's conductivity and essentially governs the electronic behavior of semiconductors. Therefore, is it important to highlight how the electrons distribute themselves in these bands.

If one pictures the bands coming from an ionic bond perspective, then the electrons are transferred from the least to the most electronegative atom, completely fulfilling the VB (in the same way that the electrons in the valence orbitals fulfilled the HOMO in Figure 7B). However, in the case of semiconductors, only at absolute 0 K the VB is completely full because room temperature provides enough thermal energy for some electrons in the VB to be excited up to the CB (energy is sufficient to cross the band gap). That is, in semiconductors, the band gap energy is small enough so that both the VB and CB are, to a small extent, partially filled at room temperature. This again fulfills the criteria for electrical conduction, allowing the semiconductor to transmit small amounts of current.

This process might seem relative straight forward but the promotion of electrons up to the CB, a process also known as carrier generation, is at the heart of materials science. Therefore, the next section is devoted to the explanation of what exactly happens to the bands when this excitation occurs and how this phenomenon generates usable current.

1.2.3 Electronic excitation in semiconductors

As mentioned in the previous section, semiconductors have a band gap small enough that room temperature yields enough energy to excite electrons from the valence band (VB) to the conduction band (CB). However, other forms of energy, such as light photons, can also produce the same effect, as long as they match, at least, the value of the band gap energy. This process is represented in Figure 10.
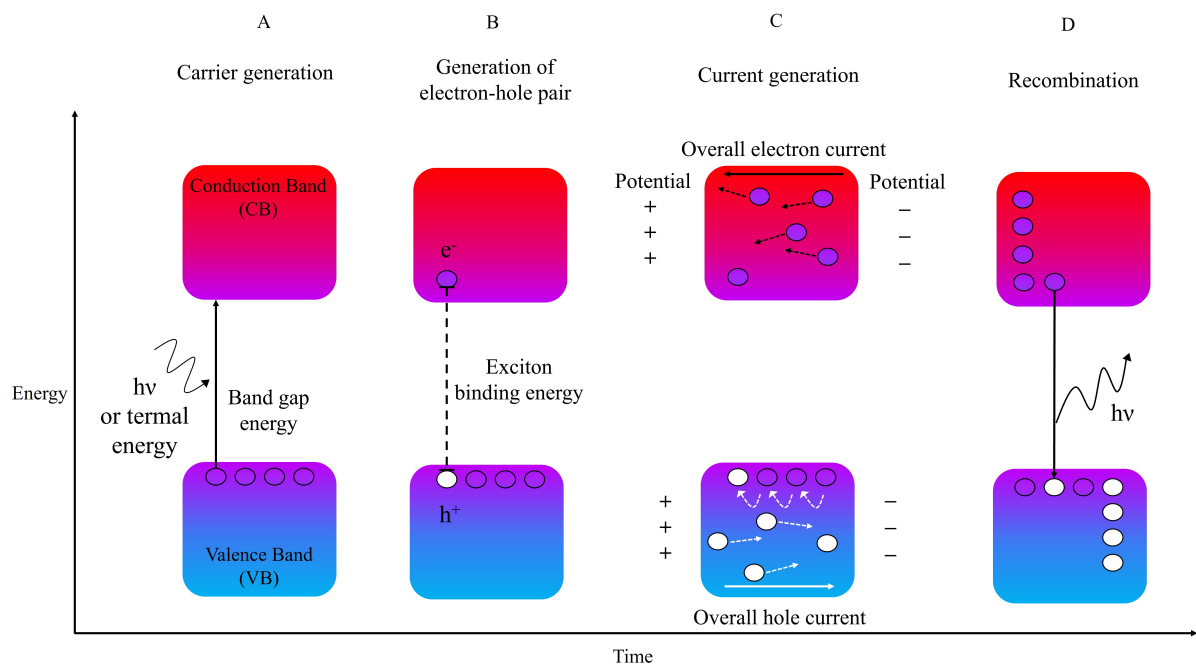
Figure 10: Semiconductors and electronic excitation. This Figure describes the process of carrier generation in semiconductors and introduces terms that relate to their stability and overall maintenance. Section A) Electrons can be excited from the valence band (VB) to the conduction band (CB) by either light photons that match the band gap energy or by heat. Section B) Upon excitation, an electron-hole pair is created. The hole lives in the VB, while the electron occupies the CB. They are held together by the exciton binding energy. Section C) With the production of several carriers, two types of current (electron and hole) can be developed, if a potential difference is established across the material. Section D) Carriers eventually recombine: the electron falls back into a hole in VB, stopping the flow of current.

In an environment of increased temperature or in which light is abundant, thermal energy or light photons are able to interact with the electrons in the (VB) and excite them, as in Figure 10A. Naturally, the electronic excitation process places the extra electron in the CB, rendering it partially filled (if assumed empty at the beginning), as well as creates a hole in the VB [18, 20]. The hole is usually imagined to be a positive charge for

simplification purposes, but in reality it is a lack of negative charge created by the leaving electron. Therefore, what was created by the energy input is actually two charges with opposite signs, commonly described as an electron-hole pair. But from basic physics, two charges with opposite signs, of course, attract each other. In semiconductors, the energy of their attraction is a stabilizing effect and is known as the exciton binding energy [18, 20]. This process is depicted in Figure 10B.

The major consequence of the binding energy is that the stronger it is, the tighter the electron-hole pair is bound and the more difficult it becomes for the carriers to disperse throughout the material. Hence, the electrons and holes are less mobile and their generation cannot effectively be translated into current propagation since the flow of carriers is halted. Conversely, a low exciton binding energy means that the electron-hole pair is easily dissociated, rendering the carriers free to promote conductivity [21]. This features is highly desirable for semiconductors whose main purpose is to promote current flow in electronic devices.

However, multiple electrons are excited in the material at any given time, as shown in Figure 10C. Technically, the movement of the carriers throughout the lattice is random, but if a potential difference is applied across the material, then the electrons and holes are attracted to the positive and negative areas, respectively. This effectively governs their motion into one overall direction, generating two different types of currents. Note though that the carrier movement (and current flow) can only take place because each band is partially filled. That is, the electrons would not be able to wander around if all the possible energy states of the CB were filled, and neither would the holes, since the VB would have been fully occupied by the non-excited electrons. This availability of states is what defines the requirement for partially filled bands for current generation in solids.

Therefore it becomes clear that electronic excitation is a fundamental process for semiconductors such as pure silicon and pure germanium (part of Group IV in the periodic table), which have their valence bands completely filled and empty conduction bands at low temperatures. Meaning that without the promotion of the electrons up to the

CB via heat or light, they would not be able to conduct electricity. However, for other semiconductors whose bands are intrinsically partially filled, which can be achieved by doping the silicon for example, then electronic excitation can help intensity the number of carriers in each band, generating a larger current overall.

The last step in the life of a carrier is recombination, as depicted in Figure 10D. That is, electron and holes are analogous to excited states in molecules and must eventually return to their ground state. In solids, the electron falls back into the valence band, filling a hole and releasing a photon of light (the carriers virtually quench one another). The rate of recombination is also an important parameter when assessing a material's ability to produce current. A high rate means that, on average, the electrons and holes are short-lived, and cannot be engaged in current production for long, whereas slow recombination (the equivalent of carriers with increased lifetime), provides the opportunity to produce current for longer periods of time.

These concepts of carrier generation, exciton binding energy, carrier-based currents and recombination help clarify the properties of a given material. Moreover, they help scientists decide its possible applications in a variety of electronic devices. For example, light-emitting diodes (LEDs) are materials whose recombination process is optimized so that photons with different wavelengths (colors!) can be generated.

In this study, perovskite materials are utilized in solar panels. Therefore, it is essential that they can effectively absorb incoming photons of light and that the carriers generated have high mobility and extended lifetimes (slow recombination). And it is indeed the case, as has been determined by extensive research by the photovoltaics community throughout the last decade [22–30] (A better explanation of how these processes arise is given in section 1.3.3).

The next task is to then dive into the chemical structure of perovskites and understand how it gives rise to semiconducting properties. In addition, it will be shown how they can be manipulated to yield efficient and stable solar panels.

1.3 Perovskites

1.3.1 Chemical structure

Solids arrange themselves in a continuous three-dimensional repetition of atoms, known as the lattice [16, 18]. But fundamentally, these atoms can be grouped into what is called the unit cell, which is the smallest unique configuration of atoms that takes into account possible rotations and packing geometries, that gets repeated over and over throughout the material. That is, the unit cell is the smallest building block of the solid.

A

B site – A divalent cation, usually a metal (Sn^{2+}, Pb^{2+}, Ge^{2+}) ●

X site – Halides (I^-, Br^-, Cl^-) or oxide anions ●

B

A site – A monovalent cation, could be either organic or inorganic (MA^+, FA^+, Cs^+) ●

MA = methyl ammonium $H_3C-\overset{+}{N}H_3$

FA = formamidinium cation $H_2N-\overset{H}{\underset{+}{C}}=NH_2$

ABX$_3$
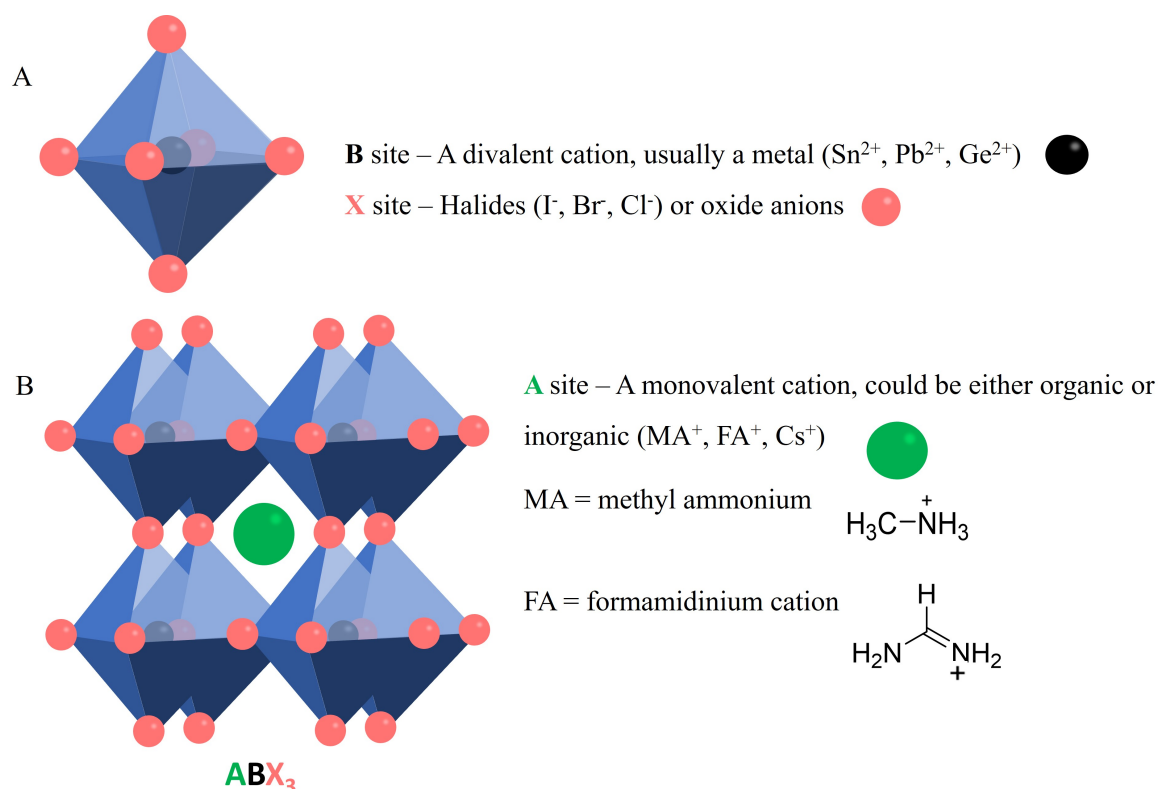
Figure 11: General structure of a perovskite unit cell. Panel A shows one individual octahedron whose structure is composed of one B site, most frequently occupied by a divalent cation, and six X sites, frequently occupied by halides or oxides. Panel B displays the formation of the A site when several octahedra are aligned in three-dimensional space. That is, the A site occupies the leftover space between them and, in metal-halide perovskites, this site is most frequently occupied by the cations methyl ammonium (MA) or the formamidinium ion (FA) [31].

Perovskite is the name given to any lattice whose structure is generalized to an ABX_3 unit cell [32–35]. This unit cell in particular is composed of several aligned metal-based octahedra and cations that fit in between them. One individual octahedron can be found

in Figure 11A. Note that the metal ion lies in the center of the octahedron (namely, position B) and achieves coordination with the six anions (position X, either halides or oxides) that occupy the corners of the structure. The exact coordination arrangement is shown in Figure 12A. As mentioned, when these octahedra are juxtaposed in three dimensions, they leave between them a space that is occupied by cations that can be either organic or inorganic based. This space is traditionally known as the A site. Note that the presence of these cations ensures charge balance of the overall structure and prevents unfavorable, direct interactions between the anions of neighboring octahedra. The position of the A-site cation is depicted in green in Figure 11B. Beyond acting as charge balancing species, these cations are unique in their bonding scheme since they can achieve impressive 12-coordinate bonding, which is displayed in Figure 12B. This specific atom orientation and bonding scheme is what is implied by the ABX_3 unit cell, which is the base of the common perovskite.
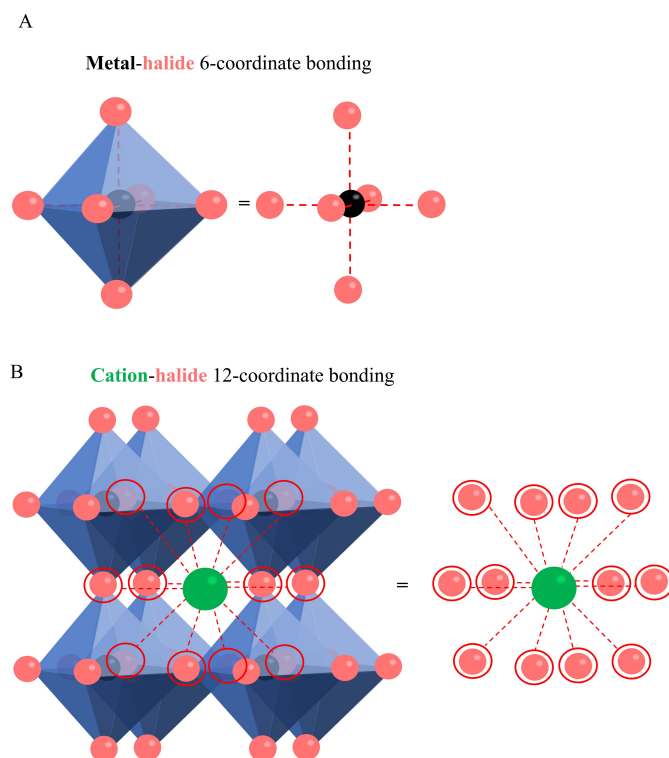
Figure 12: General coordination scheme of the perovskite components. Panel A shows the 6-coordinate bonding of the metal (site B) with the respective halides (site X) in the inorganic octahedron. Panel B shows the 12-coordinate bonding of the spacer cation (site A) with the halides (site X) of the nearby octahedra.

This structural arrangement has been known for long as in 1839 the mineralogist Gustav Rose discovered the first perovskite, namely the compound $CaTiO_3$. Since then, many other substances have been found to adopt the ABX_3 structure, such as $BaCrO_3$, $BaMnO_3$, $BaRuO_3$ and $Ba_3Re_2O_9$. But in this study, a specific set of perovskites are highlighted: metal-halide perovskites, most notably, $MAPbI_3$ and $FAPbI_3$.

In metal-halide perovskites the B site is occupied by the metal cation Pb^{+2}, while the X sites are iodides anions (I^-) [24, 29, 33–35]. The A-site cation is usually occupied by one of the two small organic molecules methyl ammonium (MA) or formamidinium (FA) (these abbreviations are used in the remaining of the text, but they are listed in the Glossary, along with the chemical structure of these cations in Figures 1 and 3 for easier reference).

These materials have attracted much attention from the photovoltaics community since metal-halide perovskites are known semiconductors with valuable properties, such as such as strong light absorption [22–26], low exciton binding energy, high carrier mobility and lifetime [27]. The next section explores how the chemical structure described above supports the creation of semiconductor band structure and how it gives rise to those desired electrical properties.

1.3.2 Semiconductor bands

The following text relies heavily on the general derivation of semiconductor bands described in section 1.2.2, only that now, it is applied to metal-halide perovskite materials.
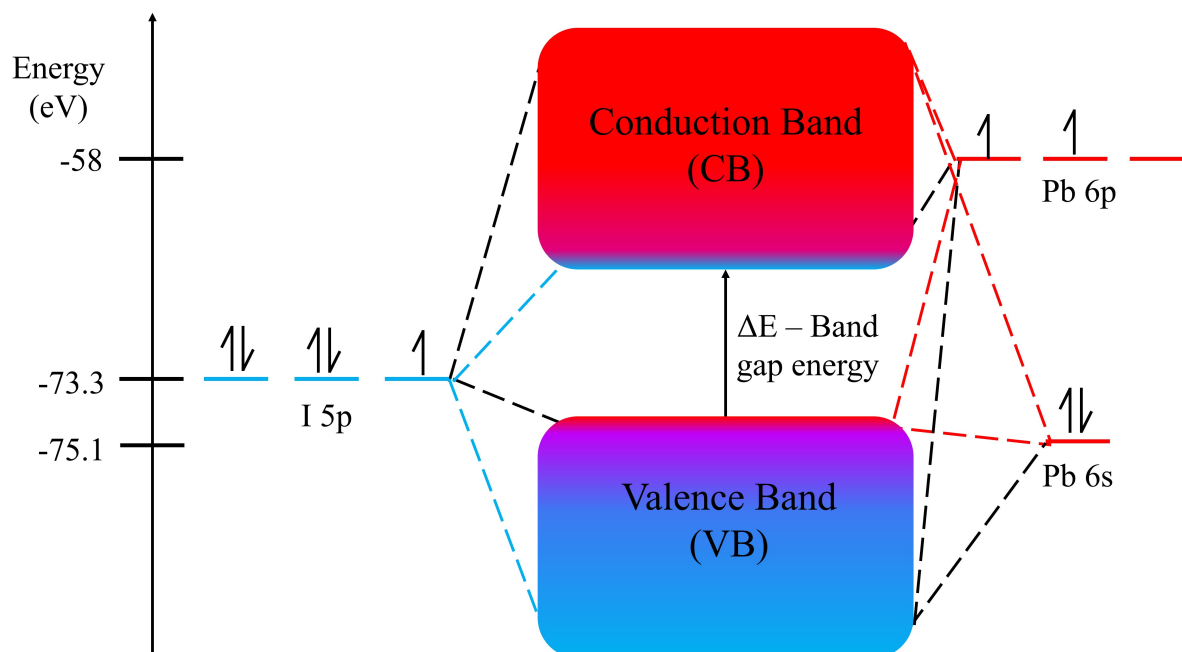
Figure 13: Metal-halide perovskite semiconductor bands. The main inorganic phase of the perovskite is composed of a lead-iodide octahedra. The valence orbitals energies (Pb 6p, Pb 6s and I 5p) are given in the diagram. I 5s is omitted since the energy is too low to provide any contribution. The I 5p orbitals interact closely with the Pb 5s orbitals leading to bonding combinations that contribute significantly to the formation of the valence band. On the other hand, I 5p orbitals interact very poorly with the Pb 6p due to a large energy separation. Consequently the conduction band's overall electron density closely resembles that of the valence Pb 6p orbitals. This bonding scheme also creates a band gap, characteristic of semiconductors, mostly due to the energy separation of the Pb and I valence orbitals. Even though the MO diagram of the inorganic octahedra was by-passed, the metal-halide perovskite band structure features highlighted in this Figure agree with experimental data and theoretical calculations [36, 37].

As observed in section 1.3.1, metal-halide perovskite have essentially two different components: the inorganic octahedra and the small organic cations that occupy the A-site (see Figure 11B) and it is the lead-halide octahedra that creates the semiconductor band structure [21, 37], through the following derivation.

The lead has a ground-state configuration of $[Xe]6s^24f^{14}5d^{10}6p^2$, but only the $6s^26p^2$ electrons occupy the valence shell; whereas iodine has a ground state electronic configuration of $[Kr]5s^24d^{10}5p^5$, but only the $5s^25p^5$ electrons occupy the valence shell. Previous studies have investigated the energies of these orbitals and found that for lead, the energies

of the 6s and 6p orbitals are about -75.10 eV and -58 eV, respectively [38, 39]. For iodine, the energy of the valence orbitals 5s and 5p were found to be -98.7 eV and -73.3 eV, respectively. These orbitals are shown in Figure 13.

With these energies in hand, the next step is to build a molecular orbital diagram considering the octahedral geometry of the Pb-I bonds in the perovskite using the LCAO principles [19]. However, this derivation would require the introduction of how orbitals with s and p symmetry interact with each other (formation of σ-bonds), as well as how p orbitals can interact head-to-head and side-by-side, generating both σ- and π-bonds. Even though exciting, this discussion is not fully necessary since due to the repetition of these octahedra in space, the molecular orbitals generated by LCAO eventually become so close in energy that they form the two semiconductor bands displayed in Figure 13. Nonetheless, I would like to refer a curious reader to the work of Kim and colleagues [21], in which the molecular orbital for the inorganic $PbI_6{}^{2-}$ is given (page 7870), as well as a more in depth discussion about the density of states of these bands.

However, there are still some remarks that are within reach considering the foundations laid in the previous sections. First, the orbital energies of I 5p and Pb 6s are very close, as presented in Figure 13. Therefore, one should expect a strong stabilization of the bonding molecular orbitals associated with these interactions (same process described in Figure 7A), forming most of the energy levels that make up the valence band. The electron densities should be also evenly distributed and the band should be almost fully occupied, since the I 5p and Pb 6s valence orbitals have almost all electrons paired.

Conversely, there is a much larger energy gap between the Pb 6p and the I 5p orbitals, analogous to the ΔE_2 shown in Figure 7B. Therefore, these interactions lead to much poorer overlaps, causing the antibonding combinations of the Pb 6p and I 5p orbitals to be close in energy to the valence 6p orbitals of the lead. Consequently, the conduction band is mostly made of the electron density donated from the Pb orbitals. But this is key: the very difference in the orbital energies of the Pb 6p and I 5p is what creates enough energy separation between the bands, creating the desired semiconductor band gap!

The relative electron density character the bands, meaning the conduction band being heavily influenced by the electron donation of the Pb 6p orbitals (or Pb 6s - I 5p antibonding MOs) and the valence band being composed of the electron donation of Pb 6s and I 5p orbitals, has been experimentally verified by experiment and density functional theory calculations [36, 37].

But note the following: due to the number of electrons present in the Pb and I, some of the electron density is pushed up to the CB [21] and as in any semiconductor, room temperature is enough to create some holes in the VB. These two features combined render the perovskite bands partially filled, meeting the criteria for conductivity.

Therefore, it's been shown that the inorganic octahedra can form a band structure characteristic of that of semiconductors, through the overlap of the valence orbitals of Pb and I. And, that the resulting bands are partially filled. However, this analysis is very basic, since the perovskite lattice is also composed of the A-site cations, which should be also factored in for more rigorous derivation (though it remains true that the VB and CB electron densities follow the description shown above [36]). But for the purposes of this study, the claim that VB is composed of the electron densities of the I 5p and Pb 6s and that the CB is composed of the electron density of the Pb 6p suffices.

Finally, it should be stated how the perovskite bands give rise to the electronic properties that render these materials suitable candidates for solar panel applications.

1.3.3 Semiconductor properties and material advantages

Metal-halide perovskites, especially of the form MAPbI$_3$ or FAPbI$_3$, have strong light absorption features, such that upon illumination, these materials facilitate electronic excitation, quickly generating carriers (Figure 14A). Additionally, they have a low exciton binding energy, which allows the carriers to smoothly move through the perovskite lattice (Figure 14B). This promotes current development. Moreover, extended carrier lifetimes provide the possibility for current maintenance since holes and electrons are kept separate (Figure 14D).
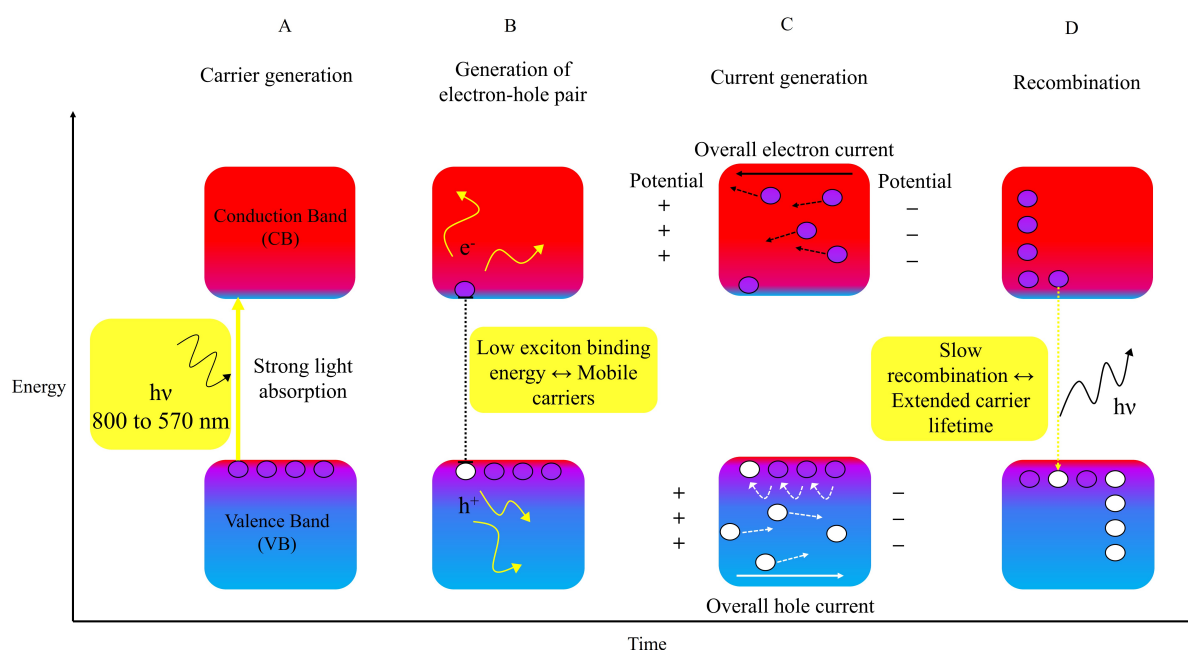
Figure 14: Perovskite semiconductor properties. The electronic properties of metal-halide perovskites that makes them promising candidates for solar panel applications. Section A) Metal-halide perovskites have a strong light absorption in the range of 570 to 800 nm [40], which can promote quick carrier generation. This wavelength range is in between the colors of yellow, orange and red. Section B) A low exciton binding energy allows carriers to be mobile through the lattice, indicating that they are suitable to drive current through the material. Section D) A slow recombination means that carriers have an extended lifetime; hence are kept apart and likely engaged in current production. All of these features combined, render metal-halide great candidates for solar cell applications, since they help extend the time in which the bands are partially filled.

In other words, all these properties combined render the perovskite bands more frequently partially filled, which is the requirement to generate electricity. Therefore, metal-halide perovskites became excellent candidates for solar panel applications since

their electronic behavior supported the continuation of current flow upon shining of sunlight.

The initial solar cell devices produced with perovskites in 2009 had a very low power conversion efficiencies (PCEs), at about only 3 % out of a theoretical limit of 30 % [14, 40]. But, in the last few years, extensive research has been able to improve their PCEs to a current (as of July 30st, 2023) champion 26.1%, as reported by the University of Science and Technology of China [41]. Such an achievement was possible by promoting extensive modifications on the perovskite composition, overall device architecture and fabrication procedures throughout the decades [42].

Another interesting feature of metal-halide perovskites is their tunable band gap energies [28]. For instance, depending on the nature of the halide anion (Cl^-, I^- or Br^-), the energy difference between the VB and CB varies, leading to a different wavelength of light being predominantly absorbed. This is consistent with the idea that the semiconductor bands are generated by the successive overlap of the valence orbitals, developed in section 1.3.2, such that if the valence orbital energies are different due to the identity of the halide, then so should the band gap energies. This provides an interesting window to manipulate the energy levels of the bands, which can be useful when considering how the perovskite layer interacts with the remaining electronic components of the solar panel and when determining which wavelength of light the material should be predominantly absorbing.

Lastly, metal-halide perovskites can be more easily manufactured in larger scale and are relatively low-cost [43], especially when careful engineering of the cell architecture is taken into consideration. Therefore, several advantages render them to be strong candidates as the leading materials in the next generation solar panels. However, these perovskites do have significant disadvantages which still limits their placement in the market [24, 26, 29, 30]. These drawbacks are described in the next section, along with the possible modification in the perovskite structure that have been performed in order to help mitigate them.

1.3.4 Perovskite materials disadvantages and possible solutions

Metal-halide perovskites do have major disadvantages that currently limits their use in modern solar panels. And one of the issues happens to be present in its very structure: lead. This brings up issues considering the environmental safety, responsible use and adequate manufacturing of these materials, especially because lead iodide, the primary source of the heavy metal used to synthesize these perovskites, is water soluble. In addition, lead poisoning can provoke long-term consequences, in particular for the human nervous system.

However, investigations of the life cycle of perovskite solar cells (PSCs) have shown little contribution of their toxicity in large-scale hazard and pollution. For example, one study performed by Espinosa and colleagues has found no explicit danger in the use of lead-bases salts in the manufacturing of PSCs [44], indicating that if safe and correct processing guidelines are applied, these solar cells can be manufactured with no side-effects. However, they are not completely free of environmental impact. Another study has concluded that the major reason for metal-halide perovskites to cause some damage is not due to lead toxicity, but yet due to rapid replacement of panels that have become degraded, likely due to low water resistance [45]. This means that the components of the panels do not, by themselves, pose poisoning threats, but that the constant refabrication of rapidly degrading solar panels is what causes them to be not environmentally friendly. Therefore, it is of supreme importance to improve the stability of these panels toward moisture so that the streams and the environment can be kept free of lead and more electricity can be adequately harvested. This leads to the second disadvantage of metal-halide perovskites: moisture and heat sensitivity.

The instability of these semiconducting materials towards water and high temperatures is the main reason for their limited application to real-world solar panels to date [24, 46, 47]. For example, when prototype solar cells are subjected to a flow of nitrogen gas and high relative humidity, the efficiency of the solar panels drops about 10 % [48] over the

span of a day for MA-based perovskites. Jiang and colleagues found that this effect can be even worse when employing FA-based materials, in which up to half of efficiency is decreased under these conditions [49]. Tests performed by water submersion also show that the solar cells power output is drastically lowered, even in short periods of time [24]. Therefore, the application of perovskites in real-world conditions is still limited since standard climate conditions would destroy the material and prevent solar powering. The curious reader is encouraged to read a thorough review by Boyd and colleagues that describes this issue and includes a discussion of possible mechanisms of degradation [50].

However, there are common and efficient methods to tackle this heat and moisture sensitivity problem. One of them is to create perovskites containing different ratios of A-site cations by mixing MA and FA ions while synthesizing the material (examples of such materials would be $FA_{0.5}MA_{0.5}PbI_3$ or $(FAPbI_3)_{0.95}(MAPbBr_3)_{0.05}$) or even to exchange or mix the X-site anions (one example would be $MAPb(SCN)_2I$) [49, 51]. The other is to completely re-design the structure of the perovskite by decreasing its dimensionality, creating what are called hybrid or 2D-perovskites. This method has provided outstanding results, by greatly improving the stability of solar cells that had undergone moisture and temperature stress [24, 26, 29].

This study focuses exclusively on the latter modification: changing the dimensionality of the perovskite in order to attempt to improve the environmental stability of solar cells. A detailed description of the chemical and electronic structure of these 2D materials is given in the next section.

1.4   Hybrid or 2D-perovskites

1.4.1   Chemical structure and solar cell benefits

The main goal of this section is to introduce the chemical structure of hybrid or 2D-perovskites. Note that there is no difference between "3D-perovskites" and the general perovskites highlighted in the sections above but the distinction is made now just to emphasize how 2D-perovskites are different.
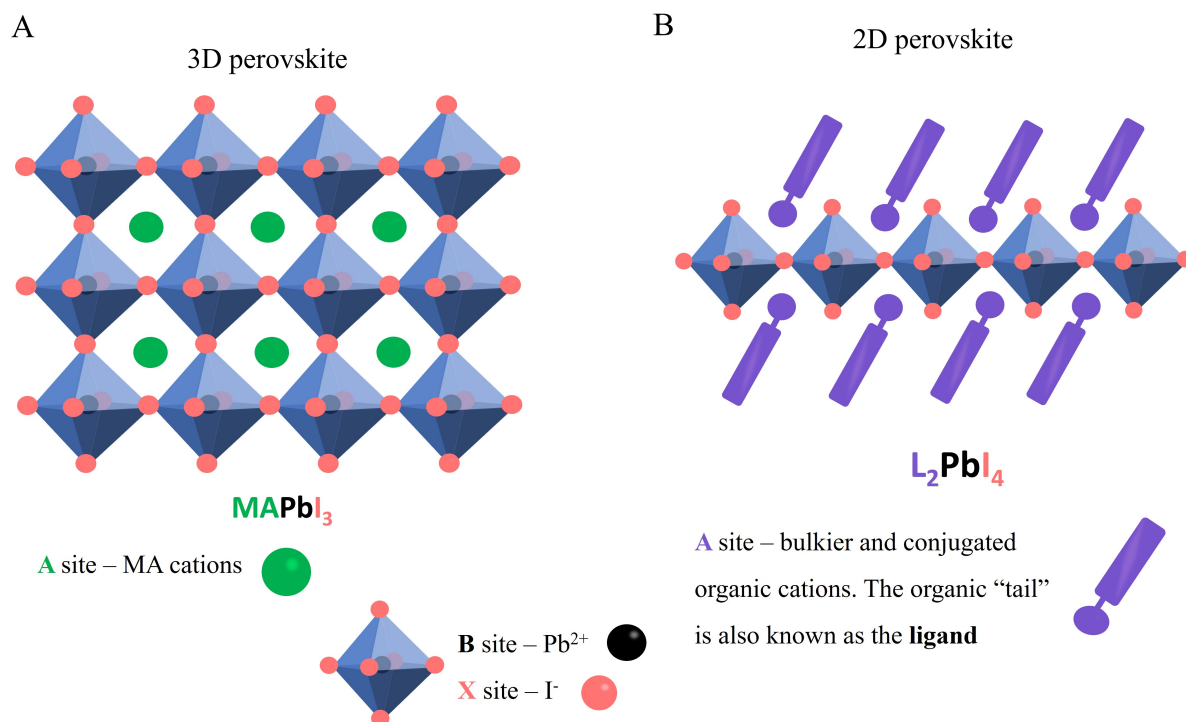
Figure 15: Direct comparison between a 3D and 2D perovskites. Panel A shows a sample pictogram of a widely used 3D metal-halide perovskite, $MAPbI_3$. The A-site is occupied by the methyl ammonium (MA) cation, which is small enough to support a 3D arrangement. The inorganic sheets expanding behind the first layer were omitted for clarity. Panel B shows a pictogram of a 2D perovskite. The A-site is occupied by bulkier and conjugated organic ligands, which force an interruption of the 3D lattice. Therefore, the inorganic octahedra do not expand upward, due the presence of organic ligands. The inorganic sheets expanding behind the first layer have been omitted for clarity. The inorganic octahedra has the same composition in both materials. The formula for the perovskite, L_2PbI_4, follows the general expression $L_2A_{n-1}B_nX_{3n+1}$ with n= 1, which is addressed in more detail in the subsequent text.

As stated previously in section 1.3.1, 3D metal-halide perovskites (i.e. $MAPbI_3$) have a uniform lattice composed by the repetition of the ABX_3 unit cell in space [24, 29, 33]. This has been reprinted in Figure 15A for comparison purposes. However, this is only

possible because the A-site organic cation, methyl ammonium (green spheres) for example, is small enough to fit in between nearby the inorganic octahedra, consequently supporting a smooth growth of the lattice in all dimensions.

This is not the case when much larger, bulkier organic cations are used to occupy the A-site valence. Note that the organic "tail" of these cations is, unfortunately, called "ligand" in materials science, escaping the definition of the term used in other areas of Chemistry. That is, the term ligand, in this study, is used to uniquely refer to the organic part of the bulkier A-site cations that are used to assemble 2D perovskites. It does not refer to the halides coordinating with the lead ion (which are traditionally called ligands in Inorganic Chemistry). This unusual definition of ligands will be used throughout this study (and was also highlighted in the Glossary for quick reference).

So, when bulkier conjugated ligands (purple rectangles) are used to replace the smaller A-site cations, they inherently lead to the self-assembly of only 2-dimensional perovskites, as depicted in Figure 15B. In other words, since these ligands are much larger, they do not fit into the space provided by neighboring lead-iodide octahedra, preventing the direct inorganic stacking in one of the dimensions (let's say upward). Therefore, this creates slabs of inorganic material (which expands sideways and front and back), instead of cubes, giving the desired 2D structural arrangement. Note that the layers behind the octahedra shown in Figure 15 have been omitted to emphasize the ligand modification and the disappearance of the inorganic layers top and bottom, even though they exist. An alternative way to visualize the effect of introducing the larger organic ligands is to think of them as capping the intermediate inorganic sheets.

2D perovskite
N=1 assembly process

Figure 16: 2D perovskite (n=1) self-assembly process. The image describes the process by which lead cations (black spheres), iodine anions (pink spheres) and bulky organic ligands (purple rectangles) combine with each other, via spin coating or recrystallization in order to produce a 2D perovskite. In spin-coating – PbI_2 and the ligands can be added to the same solution in DMF (one-step), or they can be spun-coated individually on top of each other (two-step). Follow-up annealing provides heat so that the 2D perovskite can self-assemble. In recrystallization, the formation of single crystals is usually desired. Common methods to grow these crystals are solvent diffusion or slow cooling. The formula for the perovskite, L_2PbI_4, follows the general expression $L_2A_{n-1}B_nX_{3n+1}$ with n= 1, which is addressed in more detail in the subsequent text.

The 2D material in Figure 15B is also known as n= 1 2D perovskite. This extra "n-number" piece of information relates to the number of intermediate inorganic sheets that are present in the structure. This helps distinguish the different kinds of perovskites that can be assembled in this 2D-fashion. For example, the creation of a true 2D perovskite, hence n=1, is shown in Figure 16.
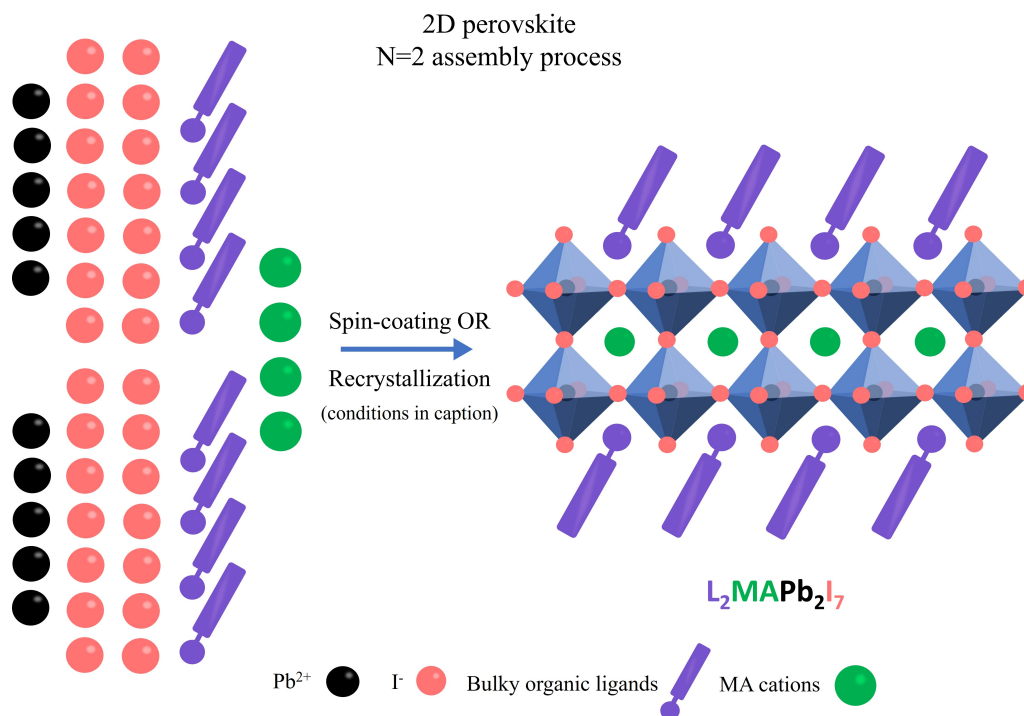
Figure 17: Quasi-2D perovskite (n=2) self-assembly process. The image describes the process by which lead cations (black spheres), iodine anions (pink spheres), bulky organic ligands (purple rectangles) and smaller organic cations combine with each other, via spin coating or recrystallization in order to produce an n=2 quasi-2D perovskite. In spin-coating – PbI_2, the ligands and the small cations can be added to the same solution in DMF (one-step), or the PbI_2 and small cations can be spun-coated followed by a ligand only solution (two-step). Follow-up annealing provides heat so that the 2D perovskite can self-assemble. In recrystallization, the formation of single crystals is usually desired. Common methods to grow these crystals are solvent diffusion or slow cooling. The formula for the perovskite, L_2PbI_4, follows the general expression $L_2A_{n-1}B_nX_{3n+1}$ with n= 2, which is addressed in more detail in the subsequent text.

Naturally, n= 2 or n= 3 structures are also possible and are very common but they receive the name of quasi-2D perovskites (see Figures 17 and 18 for respective n= 2 and n=3 assembly process), due to the presence of more than one intermediate inorganic layer. Note that for higher n-number quasi-2D perovskites to be assembled, smaller organic ligands, such as methyl ammonium, are required to be present in the starting solutions, in order to facilitate a charge-balanced stacking of the middle lead-iodide octahedra.

It should also be mentioned that the ratios of metal ions, halide anions and appropriate cations follows the stoichiometry given by the formula $L_2A_{n-1}B_nX_{3n+1}$, in which L represents the bulkier organic ligands (always two since the capping layers happen at top and bottom), B, the central metal ion (Pb^{2+}), X, the halide anions and n is the number of
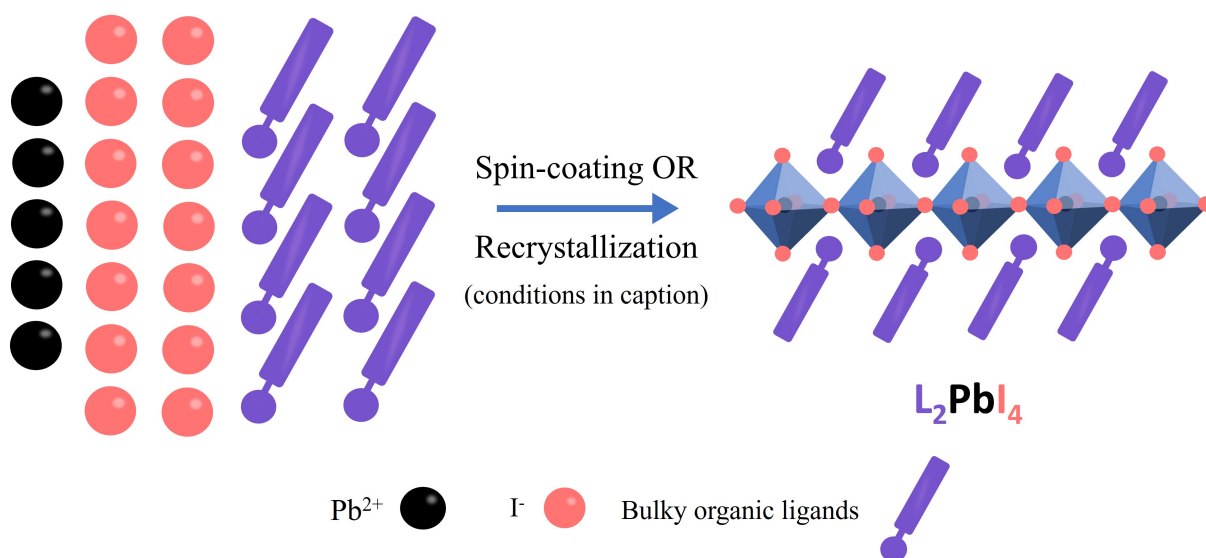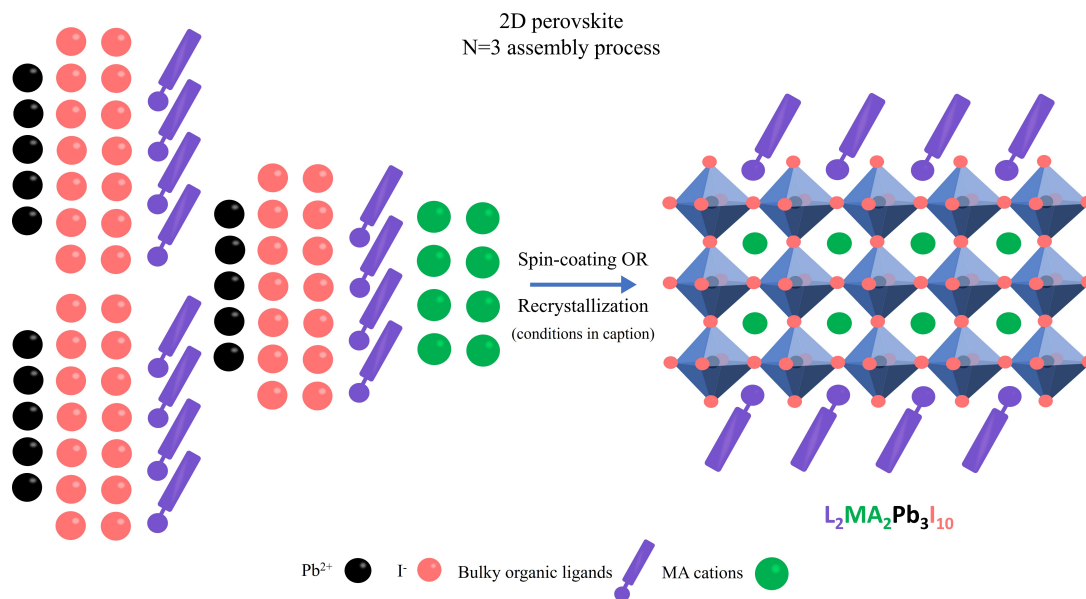
Figure 18: Quasi-2D perovskite (n=3) self-assembly process. The image describes the process by which lead cations (black spheres), iodine anions (pink spheres), bulky organic ligands (purple rectangles) and smaller organic cations combine with each other, via spin coating or recrystallization in order to produce an n=3 quasi-2D perovskite. In spin-coating – PbI_2, the ligands and the small cations can be added to the same solution in DMF (one-step), or the PbI_2 and small cations can be spun-coated followed by a ligand only solution (two-step). Follow-up annealing provides heat so that the 2D perovskite can self-assemble. In recrystallization, the formation of single crystals is usually desired. Common methods to grow these crystals are solvent diffusion or slow cooling. The formula for the perovskite, L_2PbI_4, follows the general expression $L_2A_{n-1}B_nX_{3n+1}$ with n= 3, which is addressed in more detail in the subsequent text.

intermediate inorganic sheets [24, 26, 29]. Therefore, when synthesizing (or experimentally finding) different 2D-perovskites, the number of intermediate metal sheets is central in determining the ratio of the atoms and calculating the correct material formula.

It also important to highlight the practical benefits of using these materials in the solar cells. As mentioned in the previous section, when 2D-perovskites are used in the production of solar panels, they help increase the environmental stability of the cells when exposed to temperature and moisture stressors [24, 26, 29]. One of the hypothesized mechanism of action is that the non-polarity of the ligands might help keep water molecules from interacting with the perovskite sheets. In other words, the capping layers acts as hydrophobic barriers against any incoming moisture. Therefore, solar panels designed with 2D-perovskites suffer less degradation over time.

Moreover, the insertion of these bulkier organic cations has been shown to improve

the crystallization (proper lattice formation) of the perovskite materials and lower crystal defects, which led to better conduction and smaller carrier recombination rates [52]. Therefore, they provide the opportunity to obtain control of the charge separation and recombination processes in the perovskite, which is highly desirable [26].

Lastly, introducing different functional groups in those ligands can help tune the intermolecular forces present in between different 2D-perovskite sheets, leading to the control of their stacking geometries [29].

Now that the chemical configuration of these 2D-perovskites has been introduced, along with some practical benefits of their usage, it is time to tackle their electronic arrangement. Recall that in section 1.3.2 the influence of the small organic cations in the bands of the 3D-perovskite was put aside. In 2D-perovskite, this simplification cannot take place, because the structure of the bulkier organic ligands have completely redefined the arrangement of the unit cell, creating a much more diverse pool of solids. Therefore, the ligands must have an equally strong impact on the configuration of the electronic bands.

1.4.2 Quantum well - electronic structure

This section attempts to describe the changes in the band structure of 2D-perovskites in comparison to the purely 3D materials derivation that was developed in section 1.3.2. Therefore, not only will it hinge heavily on the concepts of bands structure and the band gap energy already developed, but will also make use of some quantized analysis.
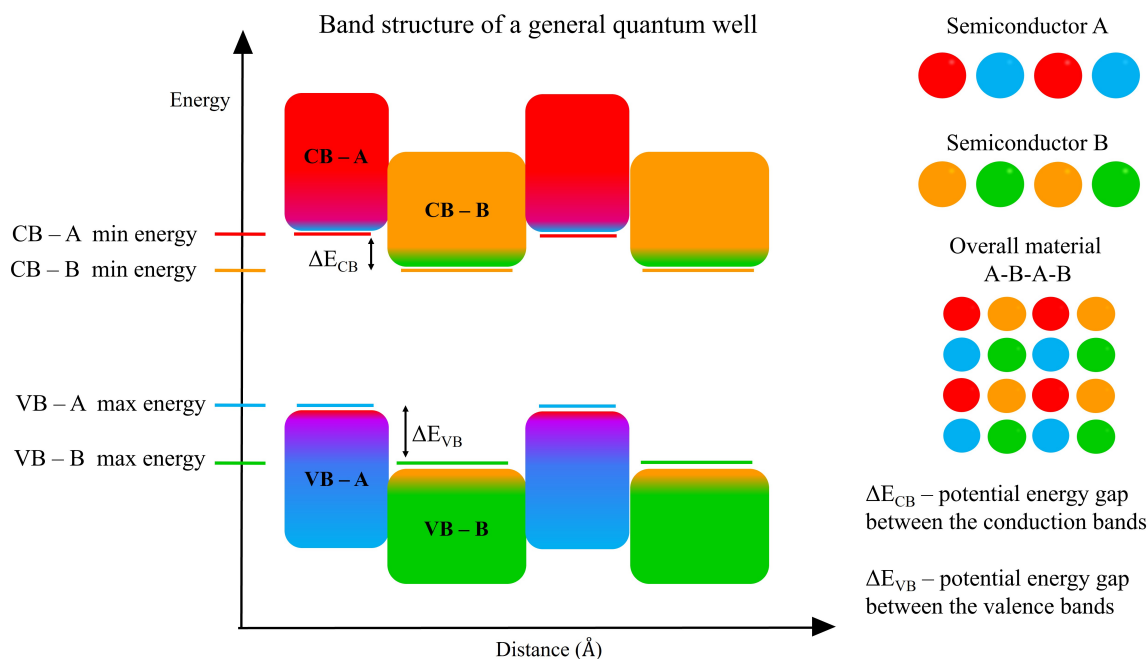
Figure 19: Band structure of a general quantum well. A quantum well is formed when two different semiconductors are juxtaposed. In that process, their valence and conduction bands become energetically misaligned, since the valence and conduction bands of the materials are not the same. Therefore, this creates potential wells within the conduction and valence regions.

The major electronic consequence of adding the bulkier organic cations and disrupting the three-dimensional growth of the perovskite lattice is the creation of quantum wells [53]. This sounds scary, but a great way to approach this dynamic is by understanding that term refers to the electronic structure of a material that is composed of two different semiconductors that have been repeatedly placed side-by-side. A schematic of a general quantum well example is shown in Figure 19. Each of these materials (semiconductor A and B) have their own band structure and hence their VB and CB have defined energy levels; but the key feature of quantum wells is that they are not the same. In other

words, the VB-A–VB-B pair and CB-A–CB-B pair are energetically misaligned [54, 55]. Therefore, this will lead to potential energy gaps in the overall band of the material.
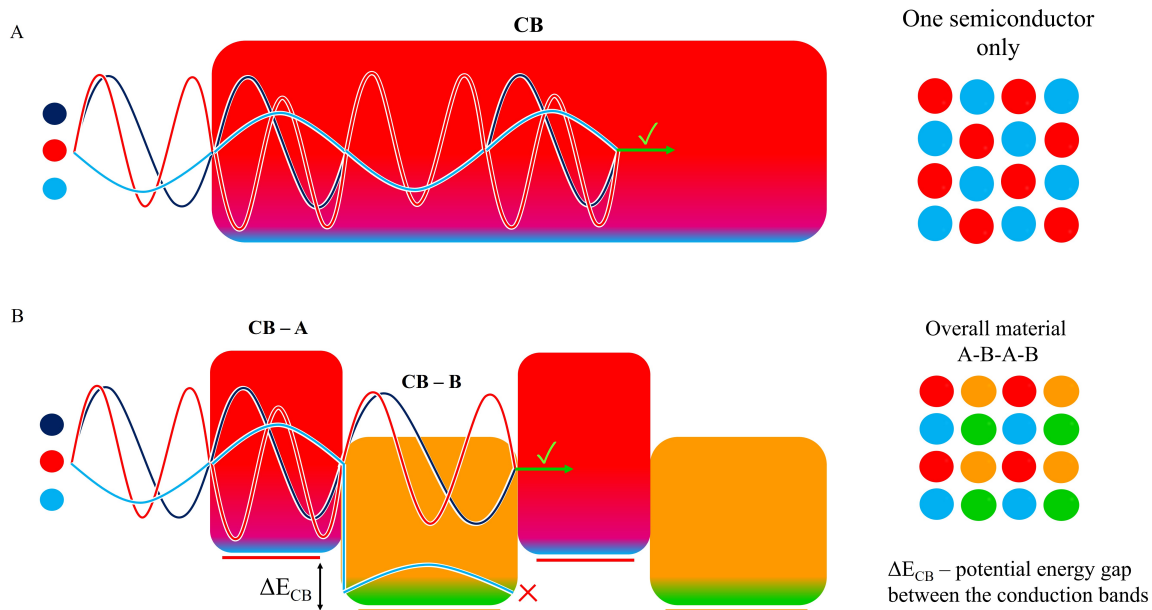
Figure 20: Quantum wells potential barrier in conduction band. Panel A shows that many different wavefunctions (symbolizes carriers) are allowed to travel to the CB of a semiconductor because there is no potential drop within the band. Panel B shows that some of these carrier waves become trapped in the in quantum well generated by the juxtaposition of the two different semiconductors. The same process takes place in the VB with holes, even though not shown.

In quantum mechanics, this translates into a selection of the wavefunctions (electrons and holes) that are allowed to travel through the resulting semiconductor *within the CBs or VBs*, as shown in Figure 20. For instance, in a material composed of only one semiconductor, any wavefunction can disperse through the CB, since there is no potential well (Figure 20A). This is not the case when two semiconductors are juxtaposed, creating the quantum well, as depicted in Figure 20B. That is, given the opportunity, some of those electrons will become stabilized in the lower CB band (let's say of the semiconductor B) causing them to be trapped in that potential well (this does not happen to all electrons, since there is still a significant overlap between the CB-A and CB-B). However, since the carrier is stuck within the potential well, it does not significantly contribute to any useful current generation. Therefore, in order to "get it out of the well", different wavefunctions will need to be selected or become more specialized. The same is true for the holes, but

in the valence bands.

While this might sound like an abstract concept, one can think of these quantum wells as a pipeline, so that only the carriers that are supported in both semiconductors upper and lower bands are allowed to flow through, promoting electrical conduction. Even though, this selection analogy is really simplistic (in reality one would need free electron models, picturing the electrons as waves, and to solve Schrödinger's equation inside and outside the well with the appropriate boundary conditions), it suffices to transmit the idea of what a quantum well is and how it is created.

In 2D-perovskites, the bulkier ligands and the inorganic sheets are the two types of semiconducting materials! That is, upon capping the inorganic sheets with the ligands, one has created a novel material (hybrid perovskites!) in which there is a repeating arrangement of two semiconductors that have different electronic bands energies [29]. However, the ligands do not touch each other or are exceptionally close when they occupy the A-site vacancy in the 2D-perovskite, and hence do not create a continuous orbital overlap (recall that the inorganic octahedra still share one of the iodide in coordination with the lead, hence leading to more facile delocalization). Therefore, it is especially useful to approximate the CB and VB coming from the ligands as the LUMO and HOMO, respectively!

Finally, one last detail should be addressed: the energy alignment of the ligands with the perovskite bands in the quantum well. They usually come in two different arrangements: type I or type II, and they impact the number of peaks observed in absorption and emission spectra (carrier generation and recombination described in section 1.2.3). Note that this alignment is ligand-dependent.
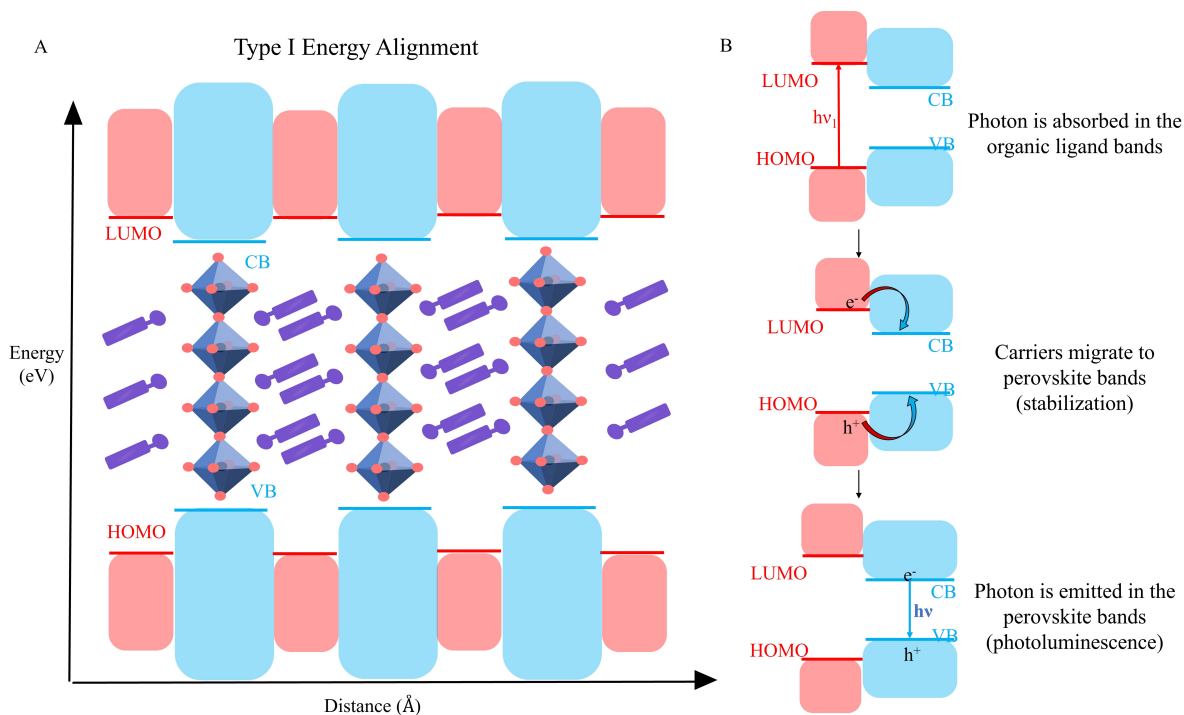
Figure 21: Type I energy alignment in 2D perovskites. Panel A shows that the HOMO and LUMO of the ligand lie in between the CB and VB of the perovskites. Panel B shows that upon light absorption in the ligand orbitals, the carriers will migrate to the perovskite bands due to stabilization. And since these electrons become localized in the perovskite, they can recombine, generating a photon that can be tracked in emission spectroscopy.

In type I (Figure 21), the HOMO energy level lies below the perovskite VB, while the LUMO is higher in energy compared to the CB, as observed in Panel A. Therefore, upon the light-absorption in the ligand orbitals, the electrons will be excited from the HOMO to the LUMO. However, by an intrinsic stabilization effect, the electrons tend to move to a lower potential energy and therefore, they jump to the CB of the perovskite (Figure 21B). Conversely, the holes move up in energy from the HOMO to the VB (equivalent to electrons being stabilized), which renders both carriers in the perovskite band. Therefore, they can recombine, generating a photon that can be detected in in emission spectroscopy.
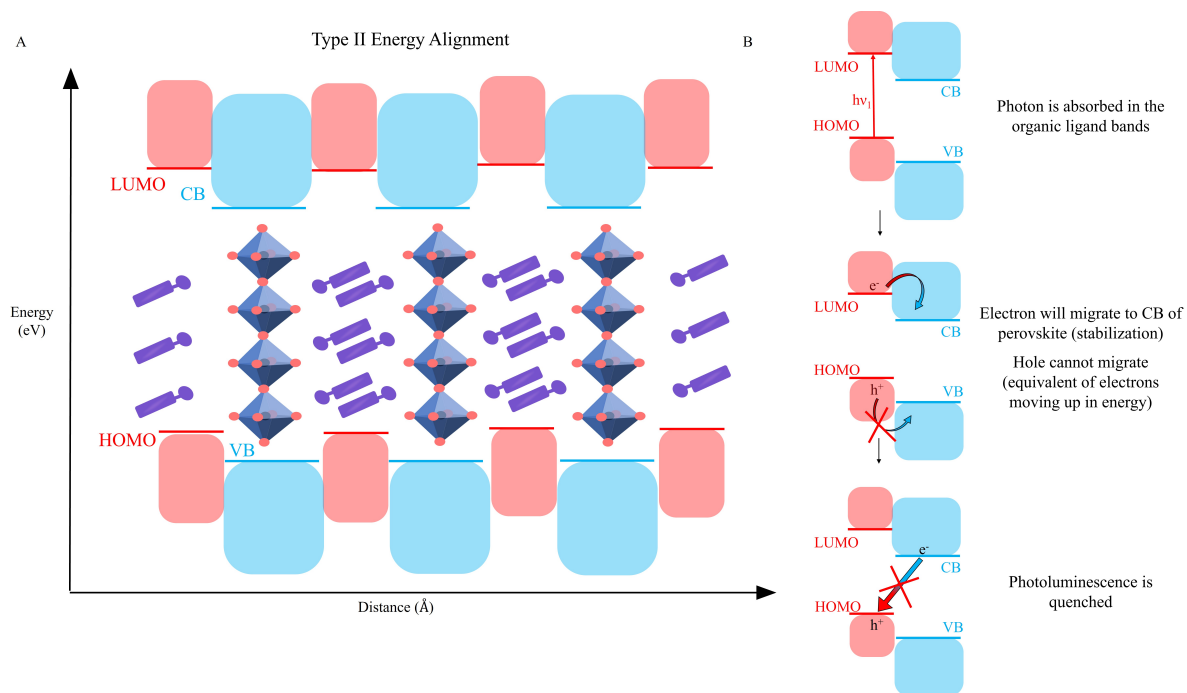
Figure 22: Type II energy alignment in 2D perovskites. Panel A shows that the HOMO of the ligand is higher in energy compared to the VB of the perovskite, in contrast with the LUMO, which lies above in energy compared to the CB. Panel B shows that upon light absorption, the electron will migrate from the LUMO to the CB of the perovskite, since it becomes more stabilized. However, the hole is stuck in the quantum well and cannot migrate to the VB (this would imply that the electrons are moving up in energy). Therefore, the traditional recombination does not take place, since the carriers are located in different bands, and no photon is emitted.

In contrast, in type II aligned materials, the HOMO lies at a higher energy state than the VB, while the LUMO is still above the CB, as shown in Figure 22A. Upon light-absorption in the ligand orbitals, the electron is again excited from the HOMO to the LUMO, and it falls into the perovskite VB, becoming more stable (Figure 22B). However, the hole created in the HOMO is stuck in the quantum well! It cannot move down in energy, because that is the equivalent of the electrons moving to higher energy state without any energy input. Therefore the carriers occupy bands from different materials and cannot recombine via the traditional process. Therefore, no photon is observed in emission spectroscopy.

Even though theoretically exciting, the quantum well feature of hybrid perovskites render them, on practice, less efficient compared to 3D materials. That is, because the carriers are trapped, they cannot engage in conduction, ultimately leading to lower power

conversion efficiencies of the solar cells [24, 26, 29, 30]. Therefore, the appropriate choice of ligand is of great importance, because it can help tune the quantum wells, providing better (or worse) electrical conductivity. Therefore, when exploring new perovskite ligands, the scientist should informed of these issues (of quantum wells and overall 2D-perovskite lower efficiency) and try to tackle them through rational ligand design.

This brings an end to the discussion on the perovskite chemical and electronic structures (oof!) and leads to their practical function: to be used as the primary light-absorber materials in solar cell devices. Therefore, a brief explanation of how these cells are produced is given on the next section.

1.5   Solar panels: Design and Physics

In this section, the basic physics of solar cell devices will be discussed, in light of the properties of semiconductor materials and in comparison to silicon solar cells.
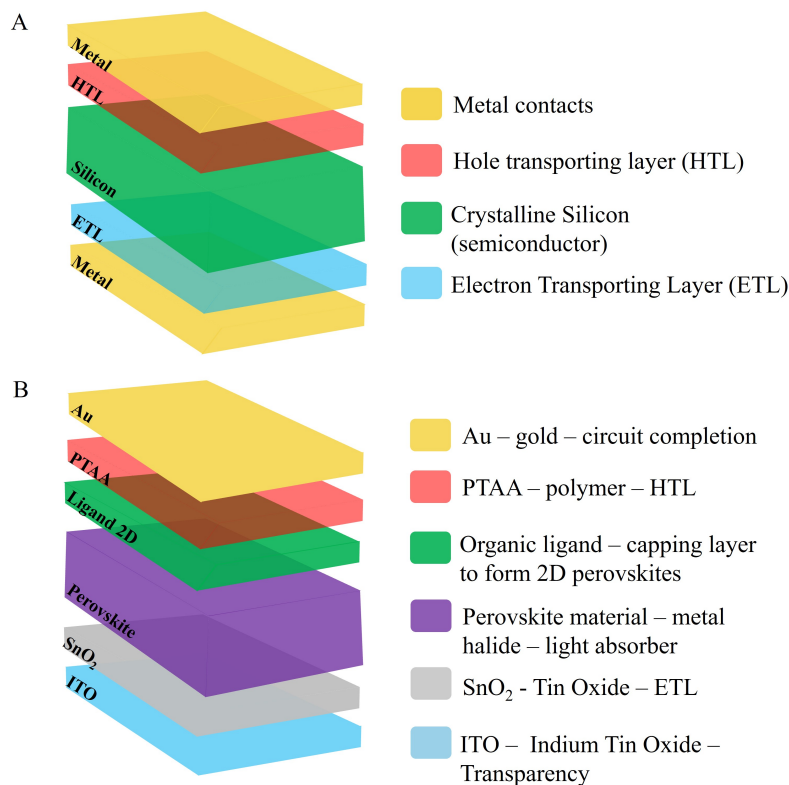
Figure 23: Solar cell architecture. Panel A shows the solar cell architecture for modern silicon devices. They are composed of a intrinsic silicon semiconductor and two layers: ETL and HTL. They are responsible for generating the potential difference across the solar cells [21, 56]. The gold layers caps the circuit. Panel B shows the solar cell device of current perovskite solar cells. The ITO layer provides transparency so that sunlight can reach the main light absorber, the perovskite with the organic ligands. The PTAA and SnO_2 layers function as the HTL and ETL, respectively while the gold caps the circuit. Adapted from Ma et al. [23].

The first solar cell created by Bell Laboratories [13] used silicon as the primary light absorber. However, Fuller and colleagues did not use pure crystalline silicon; they developed a doping procedure that enhanced the semiconductivity of the material, by creating different concentrations of holes and electrons at different sides of a silicon block. And in this process, they created the famous p-n junction, which is capable of outputting a voltage on its own, especially under illumination.

The devices currently used for testing in research laboratories built up on that archi-

tecture, and created more elaborate p-n junctions. That is, instead of doping the silicon and creating an internal carrier difference within the semiconductor, it was found that it is more efficient to use a pure semiconductor and develop the potential difference across the whole device by using two other materials or layers [21, 32, 56]: the hole-transporting layer (HTL) and the electron-transporting layer (ETL), which function as the p-type and n-type materials, respectively. Recall that when it was described that the semiconductors produced carriers, the movement of those carriers to generate usable current was conditioned to a potential difference being applied across the material (Figure 10C). The ETL and the HTL serve this very purpose: to serve as the electrical potential differences in order to allow current movement (it all comes together finally!)

In pure silicon solar cells, this is the modern device architecture, as shown in Figure 23A. The gold cap at the top serves as the final electrode so that current can flow properly upon circuit analysis.

In modern perovskite solar cells (PSCs) (Figure 23B), the same type of design is employed and it becomes quite intuitive to read the functions of these layers. Starting from the bottom: a thin coat of indium tin oxide is present in order to give transparency to the device so that light can shine through [57]; next is the ETL, composed of tin oxide (SnO_2), which is electronically rich and functions as the n-type part of the p-n junction. There are other oxides, such as ZnO, TiO_2 that can be used as ETLs, each with their advantages and disadvantages (I recommend the following review by Dkhili et al. if more information is desired [58]). Next is the perovskite, which is the primary light absorber. Note that PSCs can be constructed with either 3D or 3D+2D materials. If the latter is desired (which is the case in this study), then the ligands are deposited on top, forming a sandwich of 3D and 2D-perovskites (in that way, one keeps the great light absorbing properties of the pure perovskite and reduces environmental degradation by using the 2D materials). The HTL follows, working as the p-type material. The PTAA polymer is a common choice, but another compound called Spiro-MeOTAD is also extremely popular [56]. Lastly, the gold layer is provided to close the circuitry.

The main method though which these devices are built is called spin-coating [23, 59]. In the process, solutions of the different components (SnO_2, PbI_2, ligands and PTAA) are sequentially deposited into an ITO substrate which is spun around and heated up. The increase in temperature is known as the annealing stage during which the remaining solvents evaporate and a thin film of the material is produced, creating the desired device layer. (This procedure is further detailed on the Methods section, number 2.3).

When ready, the perovskite solar cells are analyzed by a J-V curve, in which the current response of the device is analyzed under different voltages [60]. (More details are given in the Methods section - number 2.5) This allows one to extract several parameters, such as the the V_{OC} (Open Circuit Voltage), the J_{SC} (Short Circuit current density - J), the PCE (Power Conversion Efficiency) and the FF (Fill Factor). These measurements are the most indicative of the overall efficiency of the devices and essentially determine their applicability. And as mentioned previously, the PSCs PCEs have been increasing in the last decade, allowing perovskite materials to become promising candidates for the next generation solar panels.

1.6 Ligand design

Now that all the foundation for the perovskites and the devices has been established in the previous sections, the goal of this research becomes clear: to synthesize novel ligands of 2D-perovskites in order to tackle the perovskites' environmental instability issues while attempting to maintain high efficiency of the resulting solar cells. For that, a rational ligand design was employed, considering the results of other ligands that have been created before.

Aromatic

Hong et al. *J. Am. Phys. Soc.*
1992, *45*(12), 6961-6964.

Dual amine salts

Mao et al. *J. Am. Chem. Soc.*
2017, *139*(14), 5210-5215.

Electron-withdrawing groups

Gao et al. *Nat. Chem.*
2019, *11*(12), 1151-1157.

Amide

Chen et al. *iScience*.
2018, *9*, 337-346.

Naphtalene derivative

Mishra et al. *Chem. Mater.*
2021, *33*(16), 6412-6420.

Tetrazine

Lédée et al. *Mater. Horiz.*
2021, *8*(5), 1547-1560.
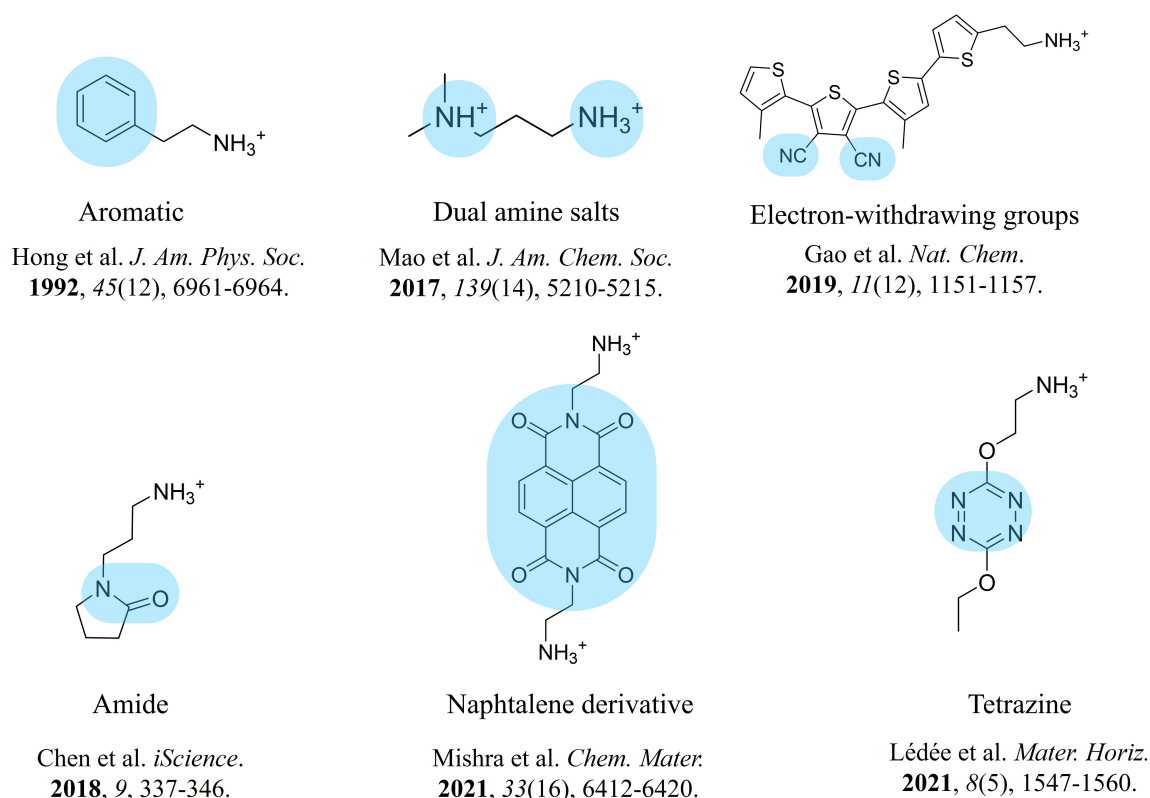
Figure 24: Examples of other ligands for 2D perovskites. The functional groups are listed below the molecule. Reference number matches are: [61] top-left, [62] top-center, [53] top-right, [63] bottom-left, [64] bottom-center and [65] bottom-right. The effect these ligands produced on the perovskites is described in the main text.

In the past, many different kinds of ligands have been synthesized. Representative structures can be find in Figure 24. They range from relatively small aromatic [61] molecules to much larger naphthalene derivatives [64]. And they can affect the perovskite properties in many ways: for example, the small aromatic molecule (top-left in Figure 24)

can help decrease the exciton binding energy of the perovskite semiconductor, leading to improved current propagation [61]; adding two ammonium heads (structure at top-center in Figure 24) can also trigger a stacking rearrangement of subsequent 2D-perovskite sheets (see Figure 27) while having an amide functional group embedded in the ligand (bottom-left structure in Figure 24) helps increase the efficiencies of the PSCs.

Conjugated ligands (top-right, bottom-center and bottom-right structures Figure 24) also provide excellent models to study the quantum wells (section 1.4.2), generating different energy alignments and perovskite band-gaps hence contributing to better charge transport across the semiconductor and better power output of the solar cell device [53, 64, 65]. Additionally, these conjugated structures lead to the formation of PSCs that have increased environmental resistance, reaching impressive power maintenance even after extended soaking periods [53].
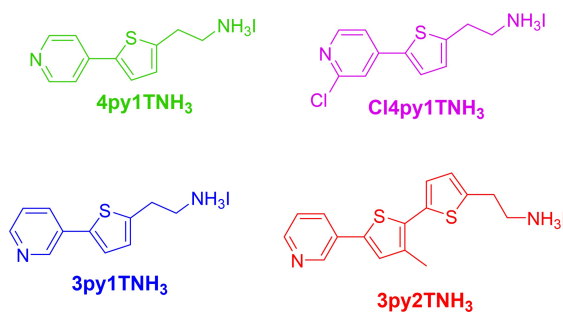
Figure 25: Structure of the four ligands synthesized in this study
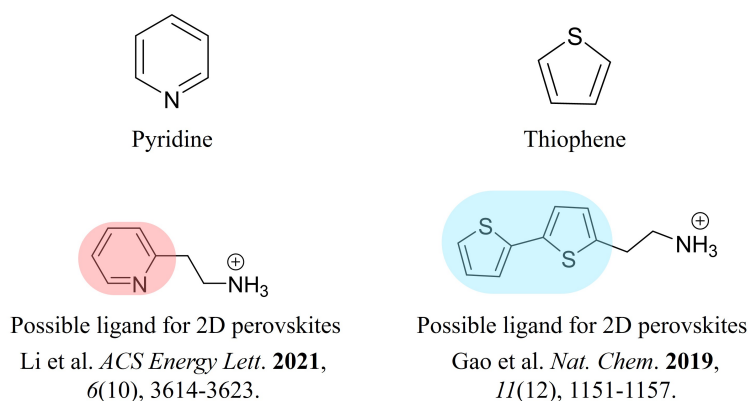
Figure 26: Example of pyridine and thiophene functional groups. In previous studies, these moieties have been introduced in other organic ligands, but they do not closely resemble those synthesized in this study (Figure 25).

This feature of conjugation is central to the four ligands designed in this study, since the functional groups chosen for exploration were pyridines and thiophenes. The structure of the ligands can be found in Figure 25 and the functional groups of pyridine and thiophene are highlighted in Figure 26.
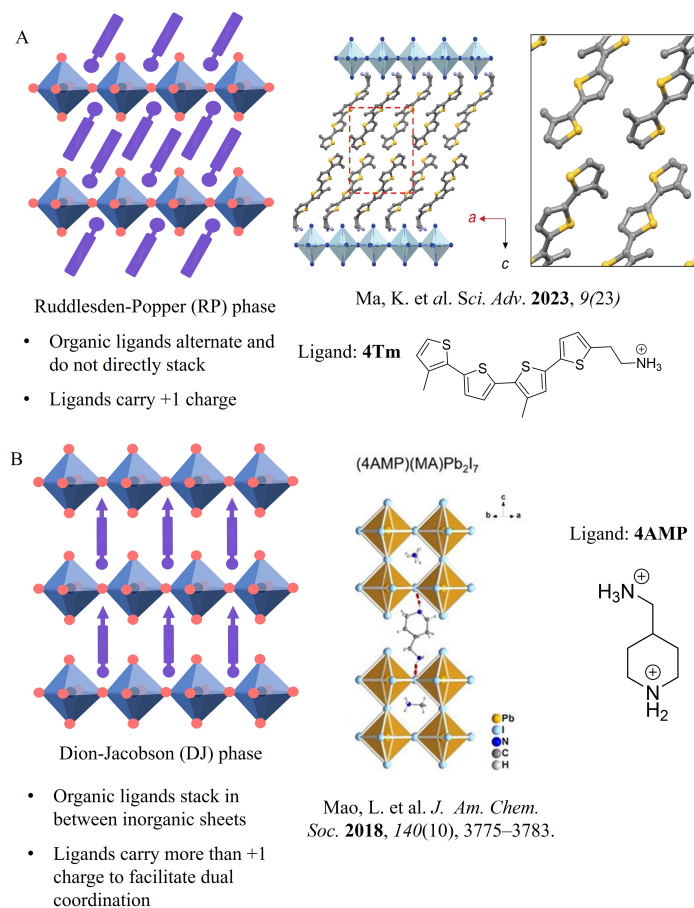
Figure 27: Different phases of 2D-perovskites. Panel A shows Ruddlesden-Popper (RP) perovskites in which the consecutive layers of inorganic octahedra are staggered. The organic ligands usually carry a +1 charge. Figure inset adapted from Ma et al. [23]. Panel B shows Dion-Jacobson (DJ) phase perovskites in which the subsequent octahedra are stabilized by a dual ammonium cation and become aligned. Figure inset is reproduced with permission form reference [66].

The main logic for the choice of the pyridine in the ligand backbone is that it was shown in previous studies to promote formation of desired 2D perovskites. At the same time, these ligands lowered defect densities of the perovskite upon crystallization and extended carrier lifetimes [52]. In this study, it was also hypothesized that addition of hydrogen bonding forces due to the presence of the pyridine nitrogen might support better 2D-3D (interlayer in PSCs) and 2D-2D (intralayer) perovskite stacking. That is, the

adhesion between sequential layers would be optimized, especially if the perovskites were assembled in Ruddlesden-Popper (RP) phase. These interactions can be visualized in Figure 27.

The thiophene moiety was chosen to continue the research performed by the Dou group at Purdue University. That is, in their laboratory, several other thiophene-based ligands have already yielded solar cells with exceptional power conversion efficiency (23% out of maximum 30%) [23, 53, 59, 67], indicating that these thiophene-based ligands seem to be promising candidates. Therefore, the combination of both pyridine and thiophene features seemed an attractive research route.

Two other ligand features must be highlighted: the ammonium head and the conjugation. The former was designed to be at end of the ligand, attached to a small alkyl chain in order to minimize steric interactions with the perovskite lattice when the ligand assembles into the A-site valence.

Frost circle diagrams
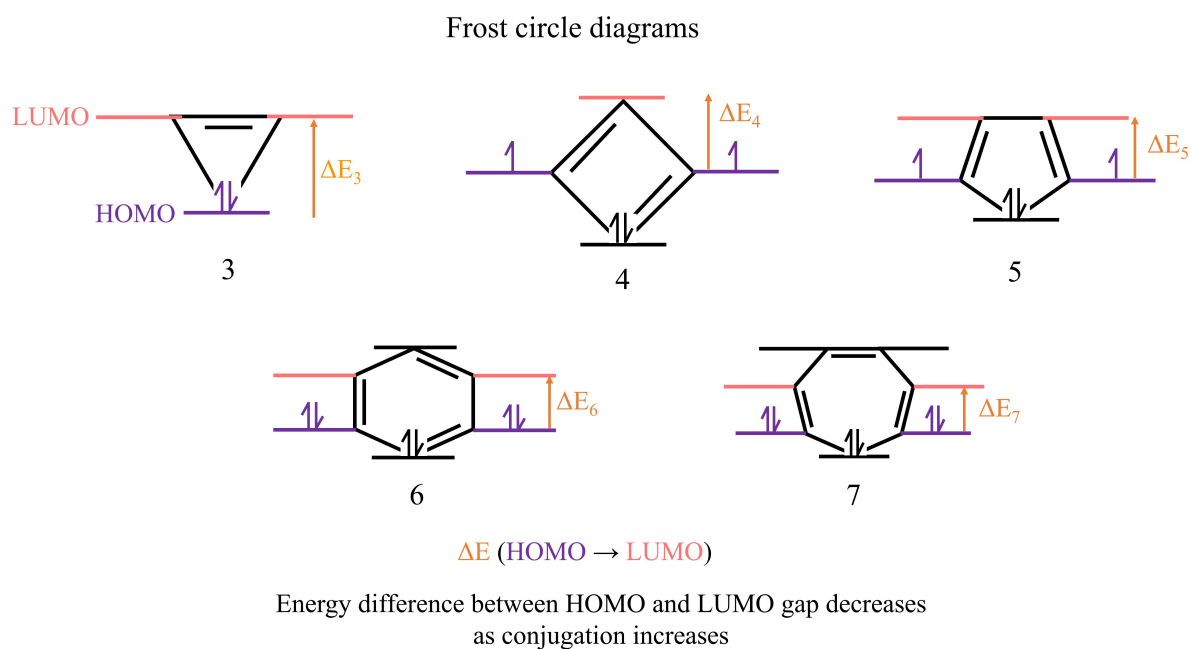
Figure 28: Frost circle diagrams. These diagrams show that with increased conjugation, the gap between the HOMO and LUMO decreases for aromatic molecules, which is the case for the ligands synthesized in this study [68].

The conjugation was designed to tackle different possible energy alignments and the electronic conduction problems. Recall that the ligand structures presented in Figure 25, three out of the four ligands have two aromatic rings fused, while 3py2TNH$_3$ contains three; hence the latter contains a larger π-conjugated system. This impacts the energy of the HOMO-LUMO gap, as given by the Frost circles, shown in Figure 28. That is, if the energy of the HOMO-LUMO gap decreases enough, then the HOMO energy level might increase enough so that the hole becomes trapped in the ligand orbitals (this would be a type II alignment, shown in Figure 22).

Moreover, this network of delocalized p-orbitals can promote out-of-plane current propagation [59], in which the electrons jump in across aromatic rings. Any incoming electricity would also face less resistance, since the conjugation provided a path for facilitated electronic flow. Both of these processes were designed to favor the production and maintenance of current within the 2D-perovskite and ligand.

Also, the conjugation creates rings that are flat in space. This helps create less steric hinderance, decreasing the likelihood that the ligands crash into the perovskite lattice or into each other, as they assemble into the A-site valence.

The next step is to discuss the purpose of the different modifications employed in the four ligand series in this study.

1.6.1 Ligand modifications within this study

As noted in Figure 25, none of the ligands are the same, even though they all display the pyridine and thiophene functional groups, the ammonium head and some level of conjugation. The modifications discussed in this section relate to the position of the nitrogen atom in the pyridine ring and the halogenation of the ligand Cl4py1TNH$_3$.

The position of the pyridine nitrogen is strategic. In ligand 4py1TNH$_3$, the nitrogen atom occupies the fourth position in the ring (in relationship to the bond that connects the pyridine to the thiophene). This is relevant when considering the formation of perovskite interlayer interactions, as depicted in Figure 27. That is, when the 2D-perovskite sheets and the capping ligands stack on each other upon crystallization, it was hypothesized that the symmetrical presence of the nitrogen might create stabilizing intermolecular forces (IMFs) between the pyridine nitrogen's lone pair and a polarized hydrogen atom in the sheet above. This would create a better lattice formation enthalpy, hopefully driving better recrystallization. Note that for this interaction to be possible, the perovskite lattice would most likely have an RP geometry (see Figure 27A)

Additionally, if the pyridine nitrogen were to be ever protonated by hydroiodic acid upon crystallization (see Methods section 2.6), the ligand would become a divalent cation. Therefore, the formation of DJ phase perovskite (Figure 27B), in which the 2D layers are directly stacked with each other, could be attempted. Therefore, ligand 4py1TNH$_3$ provides the possibility for the formation of two different perovskite phases, which is very interesting.

In ligand 3py1TNH$_3$, the pyridine nitrogen atom occupies position number 3. This could prove more difficult to form stabilizing intermolecular forces among different perovskite layers since the ligand might be required to bend. Nonetheless, some rotational freedom is granted by the small alkyl chain, which might be enough to allow those IMFs to take place and support 2D perovskite crystallization.

The halogenation modification in the ligand Cl4py1TNH$_3$ also probed on the interlayer

hypotheses. For instance, the addition of the chlorine leads to an inductive pull on the electron density in the pyridine ring, changing the electron density distribution. This might favor the formation of dipole-dipole interactions between subsequent perovskite sheets, again contributing to a favorable enthalpy of crystallization. Additionally, in past investigations in the Dou group, the insertion of halogens at those positions seemed to significantly increase the solar cell device performances, rendering these materials more successful [23, 53, 59].

The effect of increasing the conjugation in the ligand 3py2TNH$_3$ was described more thoroughly in the previous section (1.6). But as reminder, this ligand should have a smaller energy gap between the HOMO and the LUMO, following the analogy of Frost circles. Therefore, a different perovskite-ligand energy alignment (section 1.4.2) could be achieved.

With all the desired modifications decided (halogenation, increased conjugation and position of the pyridine nitrogen), it was necessary to develop a synthesis plan and finally do some Chemistry!

1.7 Synthesis plan

Developing a synthetic route is key in Organic Chemistry since it lays down the necessary transformations so that target molecules can be synthesized without major complications and is especially imporant when multiple intermediates are required. This is the first step in the project strategy, since good reaction designs can help save time and resources.

Project strategy
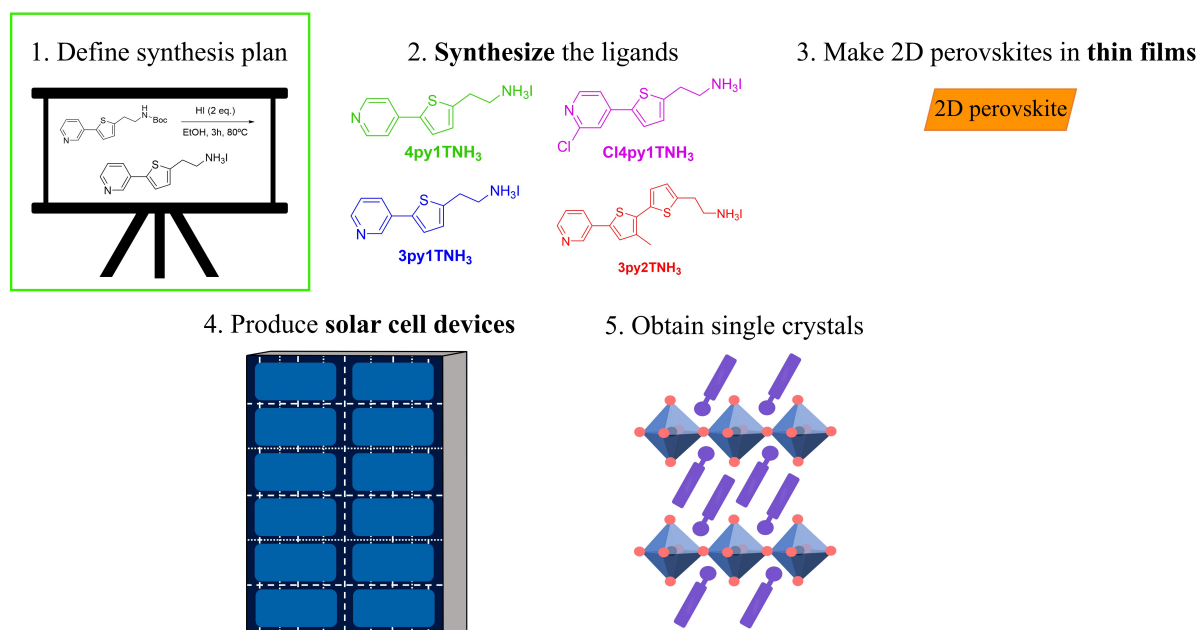
Figure 29: Project strategy - Step 1: Define synthesis plan

The 2-ring ligands reactions are addressed first.

1.7.1 2- and 3-ring ligands

As shown in Figure 25, three of the four ligands in this study contain two aromatic rings, one pyridine and one thiophene, which can be synthesized through the same route, with only small modifications in stoichiometry and purification procedures. The synthesis of the 3-ring ligand is described afterward.
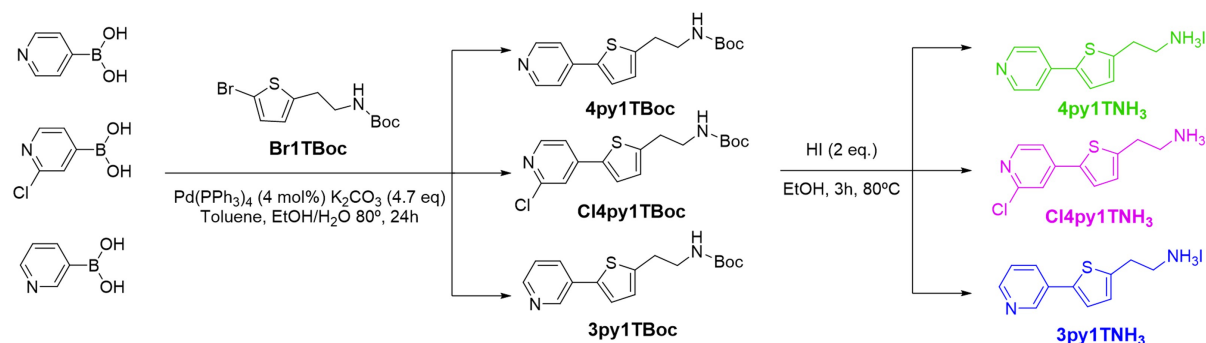
Figure 30: Synthesis plan for 2-ring ligands. All three ligands follow the same synthetic route. In the first step, a well-known Suzuki coupling reaction is used. In the second, deprotection and protonation of the resulting amine yields the desired 2-ring ligands.
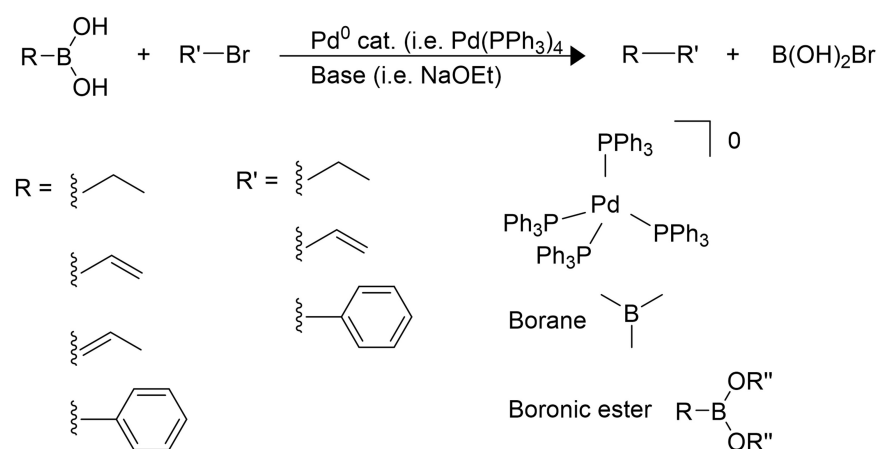
Figure 31: General Suzuki coupling scheme. Samples of possible boronic acid R group and halide R' groups are shown. But the reaction could also take place with boranes or boronic ester. Two sample structures of these different boron-containing reagents are also displayed. The structure of solid Pd(PPh$_3$)$_4$, (palladium-tetrakis(triphenylphosphine)) is shown. This organometallic complex is essential to effectively carry out the coupling.

The first step of the synthesis plan, as shown in Figure 30, takes advantage of a widely used and Nobel Prize-winning coupling reaction, known as the Suzuki coupling [69]. In its most basic form (as shown in Figure 31), a Suzuki coupling reacts a molecule

containing either a boronic acid (R-B(OH)$_2$, or boronic ester (R$_1$-B(OR$_2$)$_2$) group with a halide-containing substrate (that could be a alkyl, vinyl or aryl halide - R') in the presence of a base and an organometallic complex. In the past, all of these reagents and possible solvents have been scrutinized ([70], and references therein), since this reaction creates a much-desired carbon-carbon bond [71] in which either side of the bond could be sp$_2$ or sp$_3$ hybridized, in a environmental of relatively low toxicity in comparison to other organometallic couplings.

In the project, the creation of C$_{sp^2}$-C$_{sp^2}$ bond was desired, so that the pyridine and thiophene rings could be readily connected. The group chosen to bear the boronic acid was the pyridine since the reagents with different nitrogen positions and halogen substitutions were commercially available through Sigma Aldrich. The thiophene ring, then, carried the halogen (Br1TBoc in Figure 30), and a BOC protecting group (*tert*-butyloxycarbonyl - the reasoning for such protection is addressed in intermediate rings synthesis plan).

The choice of catalyst and base were based on standard practice and quick availability. Hence, the widely used palladium zero catalyst Pd(PPh$_3$)$_4$, (palladium-tetrakis (triphenylphosphine)), and potassium carbonate were employed. The solvents, however, were tailored to unique starting materials used in this study: a mixture of water, toluene and ethanol. The base and boronic acid dissolve in the water and the other reagents and products dissolve in the toluene, while ethanol is used as bridge solvent so that the reagents dissolved in those different phases can appropriately react. A high stirring rate, high temperatures (i.e. 80 $^{\circ}$C) and extended reaction times (i.e. 24 hours) also help push the reaction toward completion.

$$K_2CO_3(aq) + 2\ H_2O(l) \longrightarrow 2\ K^+\ (aq) + 2\ OH^-\ (aq) + H_2CO_3\ (aq) \longrightarrow H_2O(l) + CO_2(g)$$
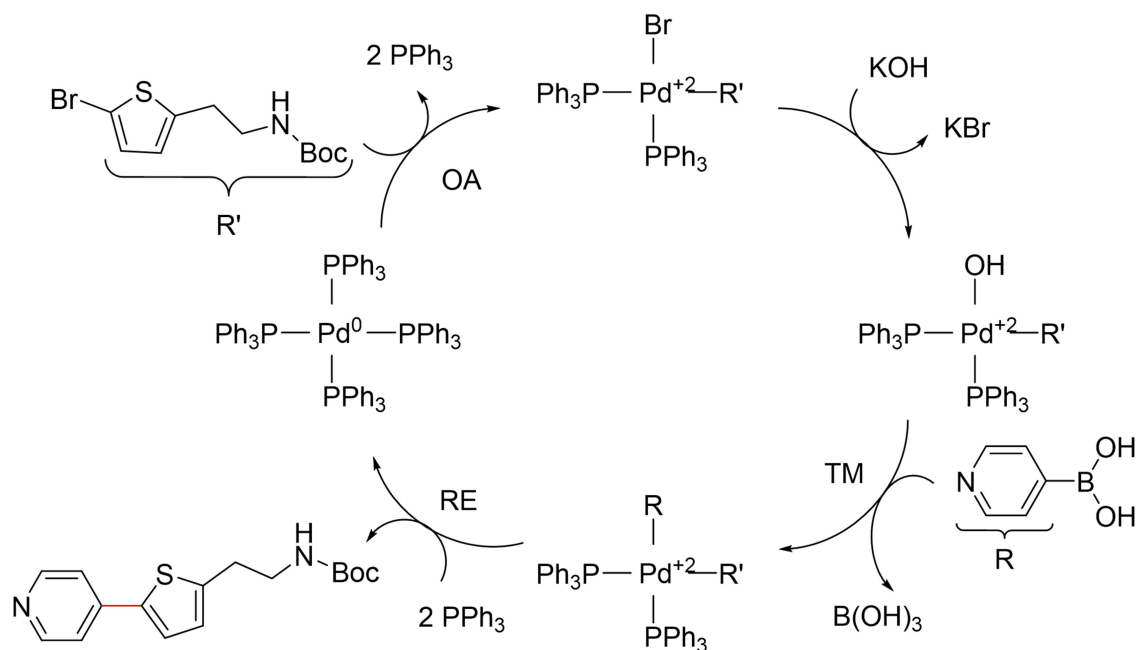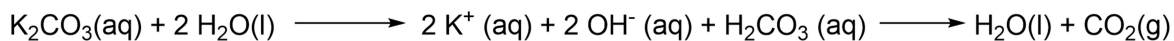
OA – Oxidative addition   TM - Transmetalation

RE – Reductive elimination

Figure 32: Proposed Suzuki coupling mechanism. The catalytic cycle drawn portraits the formation of a coupling intermediate, 4py1TBoc. In the first step (upper left), the organohalide coordinates to the metal, increasing the palladium oxidation state from 0 to 2+. Next, the base substitutes the halide in the metal center, which is followed by a transmetalation step. In the process the boronic acid reagent gives up its organic group so that the carbon coordinates to palladium. In the last step, reductive elimination takes place and the desired carbon-carbon bond is formed, releasing the organic product into into the solvent mixture. This restores the palladium oxidation state to 0 and the ligands recoordinate to the metal center, completing the catalytic cycle.

A proposed mechanism for the formation of the desired Suzuki products, in which the thiophene and pyridine rings are directly connected, is described in Figure 32. Note that the addition of potassium carbonate in water likely generates hydroxide (the carbonate ion reacts with the water to generate hydroxide and carbonic acid, which decomposes into carbon dioxide and water) and it coordinates with the metal in the mechanism. For the purpose of consuming all of Br1TBoc, the stoichiometry of the reaction was increased to 1.33 equivalences with respect to the boronic acid. However, in the synthesis of Cl4py1TBoc, the presence of the chlorine in the boronic acid could lead to the formation of side products, as the pyridine could couple with itself. Therefore, in that reaction, the

equivalence was lowered to 0.90.
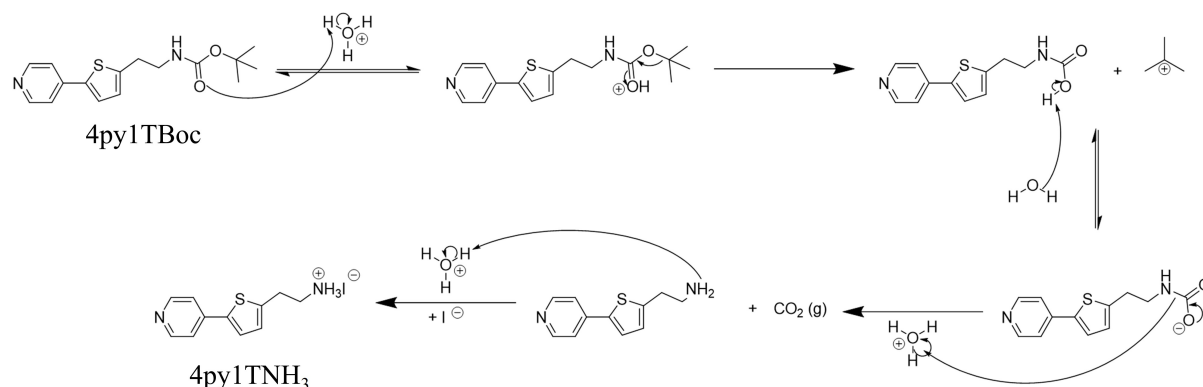
Figure 33: Boc deprotection and salt formation mechanism. In the first step, one of the equivalences of the acid is used to protonate the carbonyl, which is followed by the leaving of a stabilized tertiary carbocation. After a proton transfer, decarboxylation occurs and carbon dioxide is produced, at the same time that the amine nitrogen becomes protonated. In the last step, the amine is once more protonated by the second equivalent of acid, forming the desired iodide salt. Note that three protonations are allowed to occur, even if only two equivalences of acid are used, since in step 3 the acid is regenerated.

The final step in the synthesis of the 2-ring ligands is the creation of the ammonium head (cation) which is key so that the ligands can occupy the A-site valence in the perovskite structure. For that, the products of the Suzuki coupling are treated with two equivalents of hydroiodic acid at 80 °C. The two equivalents are meaningful since one of them is used to deprotect the starting materials and remove the BOC group, following the mechanism in Figure 33, and the other, is used to protonate the amine, creating the desired salt. The use of HI and not other strong acids is also a necessary condition, since these ligands are used to produce 2D-perovskites. That is, if other acids were to be used used, such as HCl or HBr, they could lead to the formation of counter anions Cl^- or Br^-, which might trigger the crystallization of mixed-halide perovskites.

Ethanol is used as the solvent because it can solubilize both the Suzuki products and enough acid so that the reaction can take place, even though it might still dissolve the desired salts. Therefore, to collect the desired 2-ring ligands, direct precipitation from diethyl ether was used (for explanation of extra purification procedure, see the Methods section).

These two consecutive reactions should easily yield the desired 2-ring ligands. In

contrast, to achieve a 3-ring conjugation, a more involved synthesis is required, since the introduction of the middle thiophene ring is only possible through two consecutive couplings. The synthesis plan for the ligand 3py2TNH$_3$ is displayed in Figure 34.
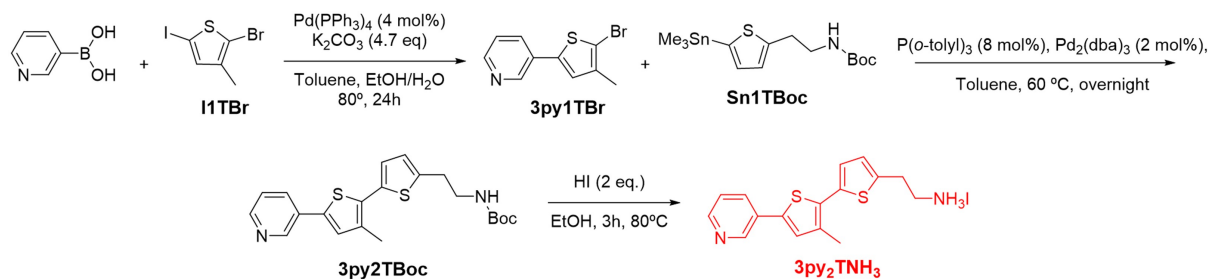
Figure 34: Synthesis plan for the 3-ring ligand 3py2TNH$_3$.

Note that the same basic skeleton as in the 2-rings is repeated: an initial Suzuki coupling and a final deprotonation. The key difference is that in between these steps, a Stille coupling is performed to add the third ring.

The initial Suzuki coupling, in this case, uses the intermediate thiophene derivative I1TBr, which contains both iodine and bromine handles. Note that Suzuki reactions favor the coupling with iodine side [70], hence leading to the formation of the product 3py1TBr, which still contains one of the handles. This allows the molecule to be used in the subsequent Stille reaction. The mechanism is assumed to be the same as in Figure 32.

A

$$R-SnBu_3 \; + \; R'-Br \; \xrightarrow{Pd^0 \; cat. \; (i.e. \; Pd_2(dba)_3)} \; R-R' \; + \; SnBu_3Br$$

B

OA – Oxidative addition   TM - Transmetalation

RE – Reductive elimination
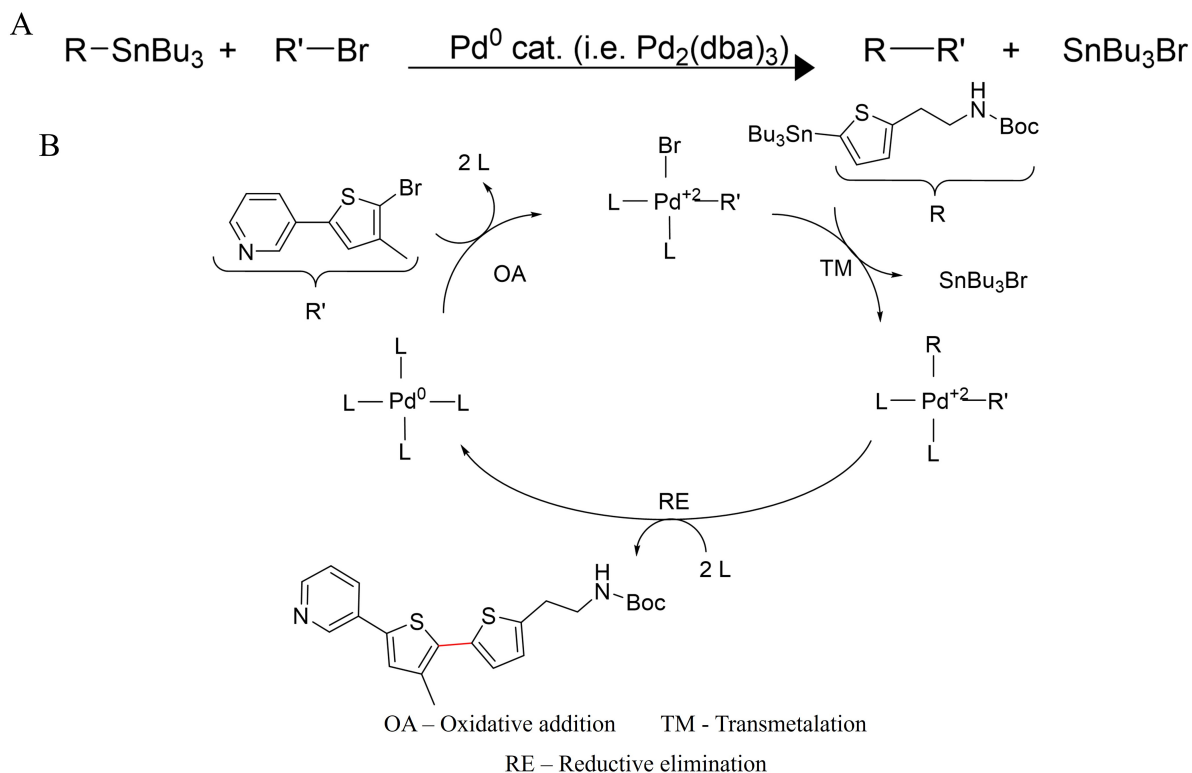
Figure 35: Stille coupling reactions. Panel A shows a general scheme of a Stille coupling. Panel B shows the mechanism that yields the desired reaction product.

Stille couplings are also extremely versatile and are widely used in Organic Chemistry, because similarly to Suzuki reactions, they deliver facile formation of carbon-carbon bonds [72, 73], as depicted in Figure 35A. But in these reactions, a tin-based reagent is used in place of the more mild boron-based reagents from the Suzuki. Therefore, this reaction is not as environmentally friendly and can generate toxic byproducts (namely $SnBu_3Br$). However, it does not require a base, since the delivery of the substrates to the metal center in the mechanism is supported by a true transmetalation step (Figure 35B).

So, for the second coupling a Stille reaction was chosen, in order to form a carbon-carbon bond between the middle and the last thiophene ring. In the reaction a palladium zero catalyst, $Pd_2(dba)_3$, was used to introduce the metal catalyst, but different phosphine ligands (in this case following the true ligand definition - this is not related to the perovskite) were added to improve the reactivity of the palladium. The solvent of choice was toluene, so that all reagents could be easily dissolved. The mechanism for product

formation is given in Figure 35B.

This specific set up in which Stille coupling is performed in the Suzuki product with the bromine handle while the tin reagent is prepared from a BOC protected thiophene is strategic (the thiophene itself is not protected - it's the amine in the substituent. This is only used as a shorthand notation). In a different scenario, for example the tin and bromine handles are swapped in these molecules, the synthesis of the tin reagent would be more expensive and time consuming since the Suzuki coupling would have to be scaled up to account for loss of yield. Or if the Stille coupling were performed first and then the Suzuki, then the synthesis pipeline would be increased, potentially calling for scale ups of previous reactions. Therefore, the reaction sequence used in this study provides the desired 3-ring intermediate in the less expensive and time consuming synthetic route.

The final reaction to obtain the desired ligand 3py2TNH$_3$ is to deprotect the BOC group and create the ammonium salt. This follows the same conditions described in the 2-ring system.

The next section is devoted to the show the syntheses of the intermediates that allowed the ligands to be created within very few reactions.

1.7.2 Intermediates

As mentioned before, the facile synthesis of the 2-ring ligands is only achieved due to the use of the advanced organohalide intermediate Br1TBoc, which is not commercially available. Therefore, it must be synthesized from simpler molecules, as shown in Figure 36.
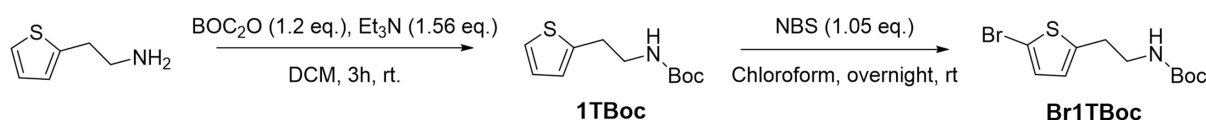
Figure 36: Synthesis scheme for Br1TBoc.

The closest starting material to Br1TBoc commercially available is thiophene-2-ethylamine, which bears the desired thiophene ring and an amine group, but no bromine handle, which then must be installed. But the available reactions for that precise transformation cannot be carried in the presence of an amine due to the formation of side products [74], leading to first step in the synthesis of Br1TBoc: protection of the amine. Note that a non-reactive amine also help ensures that no other Suzuki products are formed, since a Pd-amine coordination is also possible.
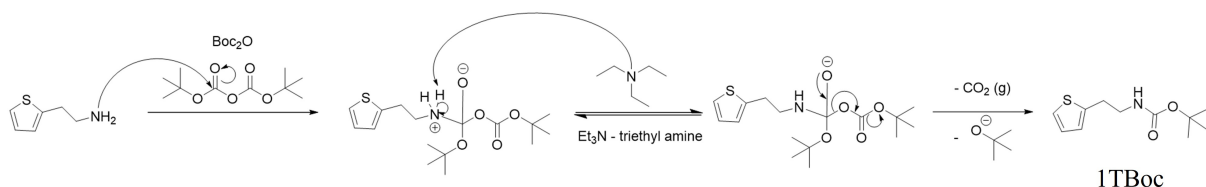
Figure 37: Boc protection mechanism. In the first step of the Br1TBoc synthesis, the starting reagent thiophene-2-ethylamine reacts with BOC anhydride. The resulting intermediate undergoes a proton transfer supported by triethylamine. In the last step, the tetrahedral intermediate collapses, leading to decarboxylation of part of the anhydride, the release of an alkoxide species, *tert*-butoxide, and the desired protected molecule. The elimination of the alkoxide is also plausible with the basic reaction conditions.

The common protecting group BOC is used since it is stable toward bases and is tolerated in the presence of radicals. Therefore, it will be tolerated in the subsequent reactions (halogenation and Suzuki coupling). Also, this reaction is fairly simple since the reactive BOC anhydride in the presence of triethylamine at room temperature can deliver

the protected molecule in high yield and in a timely manner! The mechanism of the Boc
protection can be found in Figure 37.

A

B
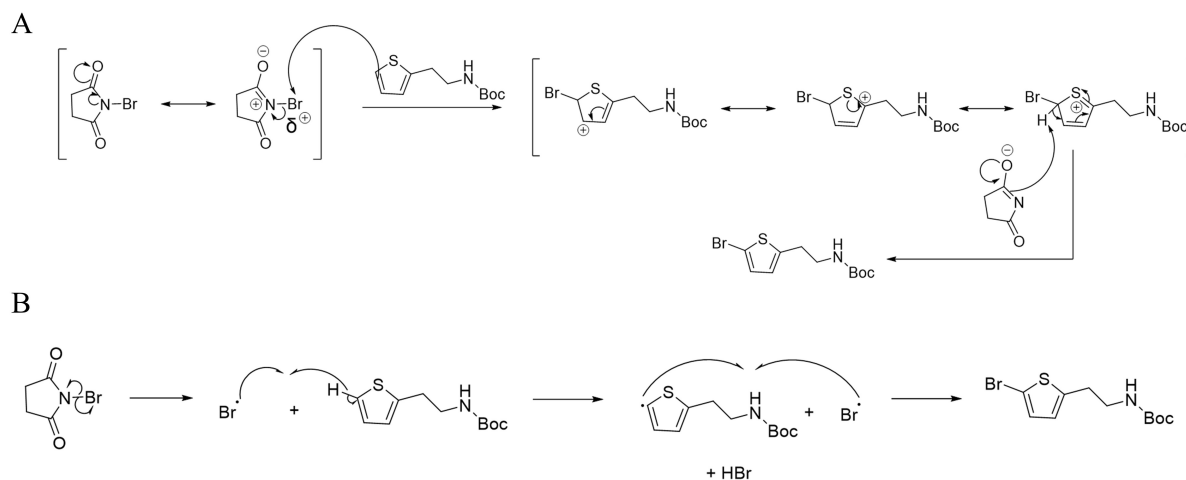
Figure 38: Halogenation of intermediate BOC thiophene. Panel A displays possible mechanism through
EAS. In the first step, the umpolung effect is shown, rendering the bromine with a partial positive charge
character. Next the electron-rich thiophene ring promotes a nucleophilic attack on the bromine, leading
to the formation of a sigma complex with three resonance stabilized structures. The introduction of the
bromine *ortho* to the sulfur is crucial, since sigma complex formed if it were introduced *meta* would be
only stabilized by the sulfur, losing aromatic stabilization. The final proton transfer restores aromaticity
(driving force of reaction). Panel B shows the mechanism if undergoing the radical pathway. Note that
the intermediate thiophene radical is also generated *ortho*, so that is is stabilized by the sulfur. The
production of HBr in the second step might help catalyze the EAS pathway as well, since the amide
could become protonated. Therefore, these pathways are not mutually exclusive and they both lead to
the same desired product.

The second step is to conduct a halogenation (Figure 36). This transformation is
commonly achieved though reagents such as N-bromosuccinimide, which are quite cool since
the presence of the succinimide in them reverses the polarity of the halogens (umpolung
effect) [75] (The curious reader is directed to the Appendix 6.2, for a richer discussion).
Therefore, they are capable of delivering, in this case, bromine radicals, although is many
cases they can also be viewed as Br_2 sources. The halogenation mechanism can then
proceed through a radical pathway or electrophilic aromatic substitution (EAS), shown in
Figure 38, both leading to the same desired product.

However, as noted above, if this reaction is carried in the presence of an unprotected
amine, a side product, an aldehyde, is formed [74]. The mechanism for this side-reaction
is shown in the Appendix section 6.2. However, since the amine was indeed protected

Br1TBoc can be effectively synthesized.

Moreover, another set of intermediate rings had to be created because the synthesis of the 3-ring ligand (Figure 34) is more involved and requires two thiophene derivatives that are not commercially available. Their synthesis is described next.

The first derivative is I1TBr, which is composed of two halogen handles and can be synthesized through another halogenation reaction, as shown in Figure 39. Note that the need for this dual handle is that two sequential carbon-carbon couplings can be performed when building the 3-ring conjugated system in 3py2TNH$_3$. The reaction conditions for this halogenation include the addition of acetic acid, hence pushing the mechanism, shown in Figure 90 in the Appendix section 6.2, toward EAS.
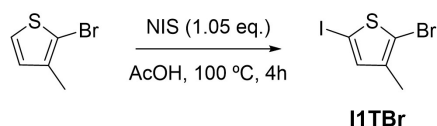
Figure 39: Synthesis scheme for I1TBr.

Another important feature of I1TBr is actually its methyl substitution. It does not have any impact on the chemistry, but it helps create some steric bulk, reducing the probability that the 3-ring ligand molecules stack on top of each other when isolated as solids (this process could be favored due to more extensive conjugation). Therefore, the presence of the methyl helps increase solubility of the 3py2TNH$_3$ ligand in the solutions prepared to spin coat thin films (allow the study of 2D-perovskites directly) and perovskite solar cells.
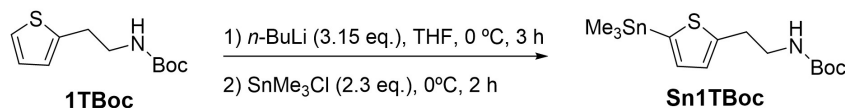
Figure 40: Synthesis scheme for Sn1TBoc.

The second derivative is Sn1TBoc, which is synthesized directly from the BOC protected thiophene. In the first step of this reaction, the thiophene ring is metalated at the *ortho* position, creating a high energy intermediate [76]. Next, upon the addition of a SnBu$_3$Cl,

the tin reagent is added at the desired position in the ring. However, this reaction is somewhat low yielding and unreacted reagent is likely to be present at the end. This creates a problem because the polarity of the starting material and product is dominated by the BOC group, rendering their separation extremely difficult. So, a higher equivalence of n-butyl lithium is used to push the reaction to greater conversion. Gladly though, in the case that the reaction is still low-yielding, the follow-up Stille coupling can tolerate the presence of some leftover starting material as it is inert under those reaction conditions.

This bring an end to the ligand synthesis plan discussion. It is time to synthesize those ligands, following the reaction conditions described above, so that they can be used to form novel 2D-perovskites and possibly improve the efficiency of current perovskite solar cells.

2 Methods

Synthesizing the ligands is the step 2 in the project strategy. Let's do some Chemistry (finally!).

Project strategy
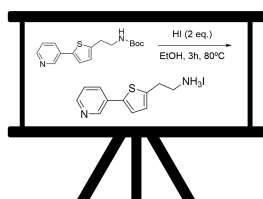
Figure 41: Project strategy - Step 2: Synthesize the ligands

2.1 Synthesis

2.1.1 2-ring ligands

Figure 42: Synthesis scheme for 4py1TNH$_3$ ligand

Synthesis of *tert-butyl (2-(5-(pyridin-4-yl)thiophen-2-yl)ethyl)carbamate*
(**4py1TBoc**)

Tert-butyl (2-(5-bromothiophen-2-yl)ethyl)carbamate (Br1TBoc) (292 mg, 0.953 mmol, 1 eq.), 4-pyridinylboronic acid (155.8 mg, 1.27 mmol, 1.33 eq.), potassium carbonate (625 mg, 4.52 mmol, 4.7 eq.) and palladium-tetrakis(triphenylphosphine) (Pd(PPh$_3$)$_4$) (44 mg, 0.0381 mmol, 4 mol%) were degassed in a Schlenk line and placed under inert argon atmosphere. Toluene (9 mL), water (2.5 mL) and ethanol (2.5 mL) were added and the resulting solution was refluxed at 80 °C for 24 hours. The reaction was extracted twice with chloroform and deionized (DI) water, and the combined organic layers were dried with brine, magnesium sulfate and concentrated down through rotary evaporation. The desired product (**4py1TBoc**) was isolated as an oil by column chromatography (start solvent mixture - ethyl acetate: hexanes 1:1 and later switched to 2:1) (234 mg, 80.66%, ^{1}H NMR - 400 MHz, CDCl$_3$: δ 8.56 (2H, dd, J$_1$ = 4.64 Hz, J$_2$ = 1.60 Hz), 7.41 (2H, dd, J$_1$ = 4.52 Hz, J$_2$ = 1.68 Hz), 7.35 (1H, d, J = 3.68 Hz), 6.86 (1H, d, J = 3.68 Hz), 4.68 (1H, s), 3.43 (2H, m), 3.04 (2H, t, J = 6.8 Hz), 1.45 (9H, s)).

Synthesis of *4-(5-(2-(iodo-l5-azaneyl)ethyl)thiophen-2-yl)pyridine* (**4py1TNH$_3$**)
Tert-butyl (2-(5-(pyridin-4-yl)thiophen-2-yl)ethyl)carbamate (214 mg, 0.705 mmol, 1 eq.) was degassed in the Schlenk line, placed under inert argon atmosphere and ethanol (14 mL) was added. To the solution, hydroiodic acid (196 μL, 57 %wt, 1.41 mmol, 2 eq.) was added and the temperature was raised to 80 °C. After overnight stirring, the suspension

was evaporated down to almost dryness and diethyl ether was added in large volume (>25 mL) to precipitate the desired HI salt. The resulting suspension was sonicated, placed in the freezer to ensure complete precipitation and thoroughly washed with diethyl ether. This procedure yielded the desired salt (**4py1TNH$_3$**) as a pale orange solid (252.2 mg, 107.8 %, ^{1}H NMR - 400 MHz, DMSO-d$_6$: δ 8.77 (2H, d, J = 6.8 Hz), 8.11 (2H, d, J = 6.76 Hz), 8.07 (1H, d, J = 3.08 Hz), 7.81 (3H, s), 7.22 (1H, d, J = 3.8 Hz), 3.16 (4H, m)). If further purification was necessary, the product was dissolved in the least amount of hot methanol, precipitated with diethyl ether, sonicated, placed in the freezer and thoroughly washed with diethyl ether three times. The color of the material became progressively lighter until a light yellow powder was achieved.

Figure 43: Synthesis scheme for Cl4py1TNH$_3$ ligand

Synthesis of *tert-butyl (2-(5-(2-chloropyridin-4-yl)thiophen-2-yl)ethyl)carbamate* (**Cl4py1TBoc**)

Tert-butyl (2-(5-bromothiophen-2-yl)ethyl)carbamate (Br1TBoc) (2.01 g, 6.58 mmol, 1 eq.), (2-chloropyridin-4-yl)boronic acid (1.04 g, 6.58 mmol, 1.0 eq.), potassium carbonate (4.27 g, 30.9 mmol, 4.7 eq.) and palladium-tetraki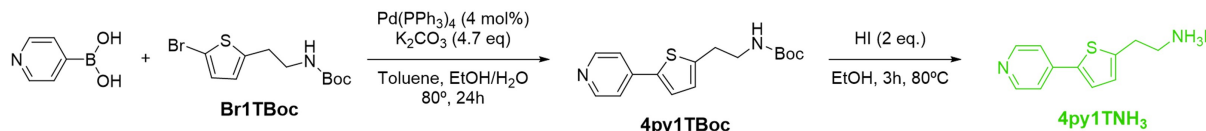s(triphenylphosphine) (Pd(PPh$_3$)$_4$) (304 mg, 0.263 mmol, 4 mol%) were degassed in a Schlenk line and placed under inert argon atmosphere. Toluene (50 mL), water (15 mL) and ethanol (15 mL) were added and the resulting solution was refluxed at 80 ^{o}C for 24 hours. The reaction was extracted twice with chloroform and DI water, and the combined organic layers were dried with brine, magnesium sulfate and concentrated down through rotary evaporation. The desired product (**Cl4py1TBoc**) was isolated as an oil by column chromatography (start solvent mixture - ethyl acetate: hexanes 1:4 and later switched to 1:2) (1.24 g, 69.2%*, ^{1}H NMR - 400 MHz, CDCl$_3$: δ 8.32 (1H, d, J = 6.2 Hz), 7.44 (1H, s), 7.36 (1H, d, J = 3.76 Hz), 7.32 (1H, dd, J$_1$ = 5.52 Hz, J$_2$ = 2.08 Hz), 6.87 (1H, d, J = 3.44 Hz), 4.68 (1H, s), 3.43 (2H, d,

J = 7.56 Hz), 3.03 (2H, t, J = 6.72 Hz), 1.45 (8.3H, s)).

*Average of 2 runs.

Synthesis of *2-chloro-4-(5-(2-(iodo-l5-azaneyl)ethyl)thiophen-2-yl)pyridine*

(**Cl4py1TNH$_3$**)

Tert-butyl (2-(5-(2-chloropyridin-4-yl)thiophen-2-yl)ethyl)carbamate (Cl4py1TBoc) (1.208 g, 3.56 mmol, 1 eq.) was degassed in the Schlenk line, placed under inert argon atmosphere and ethanol (75 mL) was added. To the solution, hydroiodic acid (992 μL, 57 %wt, 7.13 mmol, 2 eq.) was added and the temperature was raised to 80 $^\circ$C. After 3 hours, the suspension was evaporated down to almost dryness and diethyl ether was immediately added in large volume (>25 mL) to precipitate the desired HI salt. The resulting suspension was sonicated, placed in the freezer to ensure complete precipitation and thoroughly washed with ether to yield the desired salt (**Cl4py1TNH$_3$**) as a light yellow powder (1.19 g, 91.2 %, ^{1}H NMR - 400 MHz, DMSO-d$_6$: δ 8.36 (1H, dd, J$_1$ = 11.32 Hz, J$_2$ = 0.52 Hz), 7.80 (3.75H, d, J = 3.72 Hz), 7.73 (1H, dd, J$_1$ = 1.64 Hz, J$_2$ = 0.52 Hz), 7.58 (1H, dd, J$_1$ = 5.36 Hz, J$_2$ = 1.68 Hz), 7.09 (1H, d, J = 3.76 Hz), 3.11 (4H, d, J = 2.56 Hz)). If further purification was necessary, the product was dissolved in the least amount of hot methanol, precipitated with diethyl ether, sonicated, placed in the freezer and thoroughly washed with diethyl ether three times.
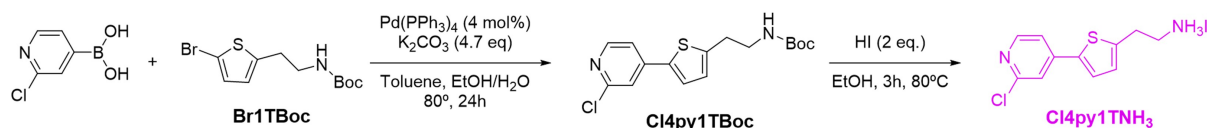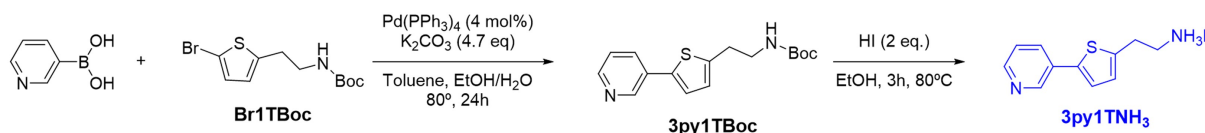

Figure 44: Synthesis scheme for 3py1TNH$_3$ ligand.

Synthesis of *tert-butyl (2-(5-(pyridin-3-yl)thiophen-2-yl)ethyl)carbamate*

(**3py1TBoc**)

Tert-butyl (2-(5-bromothiophen-2-yl)ethyl)carbamate (Br1TBoc) (292 mg, 0.953 mmol, 1 eq.), 3-pyridinylboronic acid (155.8 mg, 1.27 mmol, 1.33 eq.), potassium carbonate (625 mg, 4.52 mmol, 4.7 eq.) and palladium-tetrakis(triphenylphosphine) (Pd(PPh$_3$)$_4$) (44 mg, 0.0381 mmol, 4 mol%) were degassed in a Schlenk line and placed under inert

argon atmosphere. Toluene (9 mL), water (2.5 mL) and ethanol (2.5 mL) were added and the resulting solution was refluxed at 80 °C for 24 hours. The reaction was extracted twice with chloroform and DI water, and the combined organic layers were dried with brine, magnesium sulfate and concentrated down through rotary evaporation. Column chromatography was performed to isolate the desired product (start solvent mixture - ethyl acetate: hexanes 1:1 and later switched to 2:1) (**3py1TBoc**), which was also recrystallized from hexanes to yield high purity white shiny crystals (172.1 mg, 59.3%, ^{1}H NMR - 400 MHz, CDCl$_3$: δ 8.83 (1H, d, J = 2.24 Hz), 8.49 (1H, dd, J$_1$ = 4.88 Hz, J$_2$ = 1.48 Hz), 7.81 (1H, ddd, J$_1$ = 7.98 Hz, J$_2$ = 2.46 Hz, J$_3$ = 1.64 Hz), 7.27 (1H, ddd, J$_1$ = 8.32 Hz, J$_2$ = 4.96 Hz, J$_3$ = 0.92 Hz), 7.20 (1H, d, J = 3.72 Hz), 6.84 (1H, d, J = 4.40 Hz), 4.71 (1H, s), 3.43 (2H, m), 3.04 (2H, t, J = 6.64 Hz), 1.45 (9H, s)).

Synthesis of *3-(5-(2-(iodo-l5-azaneyl)ethyl)thiophen-2-yl)pyridine* (**3py1TNH$_3$**)

Tert-butyl (2-(5-(pyridin-3-yl)thiophen-2-yl)ethyl)carbamate (3py1TBoc) (173 mg, 0.57 mmol, 1 eq.) was dissolved in ethanol (12 mL). To the solution, hydroiodic acid (160 μL, 57 %wt, 1.14 mmol, 2 eq.) was added and the temperature was raised to 80 °C. After overnight stirring, the suspension was evaporated down to almost dryness and diethyl ether was added in large volume (> 25 mL) to precipitate the desired HI salt. The resulting suspension was sonicated, placed in the freezer to ensure complete precipitation and thoroughly washed with ether to yield the desired salt (**3py1TNH$_3$**). If further purification was necessary, the product was dissolved in hot methanol, precipitated and repeatedly washed with diethyl ether three times to yield a pale orange solid (232 mg, 122.5 %, ^{1}H NMR - 400 MHz, DMSO-d$_6$: δ 8.96 (1H, d, J = 1.84 Hz), 8.58 (1H, dd, J$_1$ = 5.04 Hz, J$_2$ = 1.44 Hz), 8.23 (1H, d, J = 8.24 Hz), 7.79 (3H, s), 7.66 - 7.59 (2H, m), 7.07 (1H, d, J = 3.68 Hz), 3.11 (4H, d, J = 2.64 Hz)).

2.1.2 Intermediates

For scheme and molecular structure, please see Figure 39.

Synthesis of *2-bromo-5-iodo-3-methylthiophene* (**I1TBr**)

2-bromo-3-methylthiophene (1.00 g, 8.54 mmol, 1 eq.) was degassed in the Schlenk line, placed under an inert argon atmosphere and dissolved in glacial acetic acid (5 mL). Under light protection, N-iodosuccinimide (1.925 g, 8.54 mmol, 1 eq.) was added against a gentle argon flow to yield an orange solution, which was heated to 100 $^{\circ}$C for 4 hours. The resulting ruby solution was extracted twice with DI water and dichloromethane. The combined organic layers were washed with a 5% sodium thiosulfate solution and dried with brine and magnesium sulfate. The organic layers were concentrated down and purified by column chromatography (hexanes used as solvent throughout the whole procedure) to yield the desired product (**I1TBr**) as a pale yellow oil (1.75 g* 75.8%*, ^{1}H NMR - 400 MHz, CDCl$_3$: δ 6.95 (1H, s), 2.16 (3H, s)).

*Average of two runs.

For scheme and molecule structure, please see Figure 36.

Synthesis of *tert-butyl (2-(thiophen-2-yl)ethyl)carbamate* (**1TBoc**)

2-(thiophen-2-yl)ethan-1-amine (4g, 31.4 mmol, 1 eq.) was dissolved in dichloromethane (80 mL) and triethylamine (7 mL, 49 mmol, 1.56 eq.) and di-tert-butyl dicarbonate (Boc2O) (8.7 mL, 38 mmol, 1.2 eq.) were added dropwise. After 3 hours, the reaction was extracted twice with DI water and dichloromethane, and the combined organic layers were dried with brine and magnesium sulfate. Upon concentrating down the resulting solution and placing the material in the freezer overnight, the procedure yielded the desried product (**1TBoc**) as a solid. (9.08 g, 122.7 %*, ^{1}H NMR - 400 MHz, CDCl$_3$: δ 7.15 (1H, dd, J$_1$ = 5.08 Hz, J$_2$ = 0.92 Hz), 6.94 (1H, dd, J$_1$ = 5.12 Hz, J$_2$ = 5.08 Hz), 6.83 (1H, d, J = 2.96 Hz), 4.66 (1H, s), 3.34 (2H, m), 3.01 (2H, t, J = 6.72 Hz), 1.44 (10H, s)). *Average of two runs.

Synthesis of *tert-butyl (2-(5-bromothiophen-2-yl)ethyl)carbamate* (**Br1TBoc**)

Tert-butyl (2-(thiophen-2-yl)ethyl)carbamate (1TBoc) (5.05 g, 22.2 mmol, 1 eq.) was dissolved in chloroform (50 mL) and placed under light protection. N-bromosuccinimide (4.15 g, 23.3, 1.05 eq.) was added portion-wise. After overnight stirring, the reaction was extracted twice with chloroform and DI water; the combined organic layers were dried with brine and magnesium sulfate and concentrated down to an oil. The desired product (**Br1TBoc**) was purified by column chromatography (dichloromethane was used as the solvent throughout the whole procedure) to yield a light orange oil (5.62 g, 82.67%, ^{1}H NMR - 400 MHz, CDCl$_3$: δ 6.87 (1H, d, J = 3.56 Hz), 6.58 (1H, d, J = 3.56 Hz), 4.66 (0.86H, s), 3.35 (2H, d, J = 5.96 Hz), 2.93 (2H, t, J = 6.44 Hz), 1.43 (9H, s)).

For scheme and molecular structure, please see Figure 40.

Synthesis of *tert-butyl (2-(5-(trimethylstannyl)thiophen-2-yl)ethyl)carbamate* (**Sn1TBoc**)

Tert-butyl (2-(thiophen-2-yl)ethyl)carbamate (1TBoc) (2.5 g, 11 mmol, 1 eq.) was degassed in the Schlenk line, placed under an inert argon atmosphere, dissolved in anhydrous THF (50 mL) and cooled to 0 ^{o}C. *N*-butyllithium (14 mL, 2.5 M in hexane, 34.6 mmol, 3.15 eq.) was added dropwise and stirred cold for 3 hours. Chlorotrimethylstannane (25 mL, 1 M in THF, 25.3 mmol, 2.3 eq.) was added and the solution was stirred for 2 hours, gradually warming up to room temperature. The reaction was extracted three times with DI water and chloroform. The combined organic layers were dried with brine and magnesium sulfate and concentrated down to an oil (4.45 g). The product (**Sn1TBoc**) purity was determined by NMR and used with no further purification in subsequent reactions (>85 % purity, 3.56 g, 83 % yield, ^{1}H NMR - 400 MHz, CDCl$_3$: δ 7.03 (1H, d, J = 3.16 Hz), 6.94 (1H, d, J = 3.12 Hz), 4.68 (0.86H, s), 3.41 (2.20H, m), 3.05 (2.5H, t, J = 6.72 Hz), 1.45 (10.2H, s), 0.35 (9.34H, s)).

2.1.3 3-ring ligand

For scheme and molecular structure, please see Figure 34.

Synthesis of Synthesis of *3-(5-bromo-4-methylthiophen-2-yl)pyridine* (**3py1TBr**)

2-bromo-5-iodo-3-methylthiophene (I1TBr) (1.52 mg, 5.02 mmol, 1 eq.), 3-pyridinyl-boronic acid (555 mg, 4.52 mmol, 0.9 eq.), potassium carbonate (3.26 g, 23.58 mmol, 4.7 eq.) and palladium-tetrakis(triphenylphosphine) ($Pd(PPh_3)_4$) (232 mg, 0.201 mmol, 4 mol%) were degassed in a Schlenk line and placed under inert argon atmosphere. Toluene (40 mL), water (11 mL) and ethanol (11 mL) were added and the resulting solution was refluxed at 80 °C for 24 hours. The reaction was extracted twice with chloroform and DI water, and the combined organic layers were dried with brine, magnesium sulfate and concentrated down through rotary evaporation. The desired product (**3py1TBr**) was isolated as an oil by column chromatography (start solvent mixture - ethyl acetate: hexanes 1:5 and later switched to 1:3) (454.1 mg, 38.4 %∗, 1H NMR - 400 MHz, CDCl$_3$: δ 8.75 (1H, d, J = 1.88 Hz), 8.49 (1H, dd, J$_1$ = 4.80 Hz, J$_2$ = 1.52 Hz), 7.72 (1H, ddd, J$_1$ = 7.92 Hz, J$_2$ = 2.32 Hz, J$_3$ = 1.68 Hz), 7.26 (1H, ddd, J$_1$ = 5.60 Hz, J$_2$ = 4.80 Hz, J$_3$ = 0.80 Hz), 7.01 (1H, s), 2.20 (3H, s)).

*Average of 2 runs.

Synthesis of *tert-butyl (2-(3'-methyl-5'-(pyridin-3-yl)-[2,2'-bithiophen]-5-yl)ethyl) - carbamate* (**3py2TBoc**)

3-(5-bromo-4-methylthiophen-2-yl)pyridine (3py1TBr) (339.5 mg, 134 mmol, 1 eq.), *tert*-butyl (2-(5-(trimethylstannyl)thiophen-2-yl)ethyl)carbamate (Sn1TBoc) (793.9 mg, 1.5 eq., 85 % purity), tris(*o*-tolyl)phosphine (45.6 mg, 0.150 mmol, 11.2 mol%) and tris(dibenzylideneacetone)dipalladium ($Pd_2(dba)_3$) (39 mg, 0.0425 mmol, 3.2 mol%) were degassed in the Schlenk line and placed under an inert argon atmosphere. Toluene (10.2 mL) was added and the solution was heated at 100 °C overnight. The reaction was extracted with dichloromethane and DI water three times. The combined organic layers were dried with brine and magnesium sulfate and concentrated down to an oil. Column

chromatography was performed to isolate the desired product (start solvent mixture - ethyl acetate: hexanes 1:3 and later increased to 1:1) (**3py2TBoc**) as a solid (390.9 mg, 62.0 %∗, ^{1}H NMR - 400 MHz, CDCl$_3$: δ 8.84 (1H, d, J = 1.88 Hz), 8.49 (1H, dd, J$_1$ = 4.80 Hz, J$_2$ = 1.56 Hz), 7.82 (1H, ddd, J$_1$ = 7.96 Hz, J$_2$ = 2.24 Hz, J$_3$ = 1.68 Hz), 7.29 (1H, ddd, J$_1$ = 8.08 Hz, J$_2$ = 4.80 Hz, J$_3$ = 0.72 Hz), 7.15 (1H, s), 7.01 (1H, d, J = 3.56 Hz), 6.81 (1H, d, J = 3.60 Hz), 4.71 (1H, s), 3.43 (2H, m), 3.02 (2H, t, J = 6.60 Hz), 2.40 (3H, s), 1.45 (9H, s)).

*Average of 2 runs.

Synthesis of *3-(5'-(2-(iodo-l5-azaneyl)ethyl)-3-methyl-[2,2'-bithiophen]-5-yl)pyridine* (**3py2TNH$_3$**)

Tert-butyl (2-(3'-methyl-5'-(pyridin-3-yl)-[2,2'-bithiophen]-5-yl)ethyl)carbamate (3py2TBoc) (337 mg, 0.841 mmol, 1 eq.) was degassed in the Schlenk line, placed under inert argon atmosphere and ethanol (17.7 mL) was added. To the solution, hydroiodic acid (234 μL, 57 %wt, 1.68 mmol, 2 eq.) was added and the temperature was raised to 80 $^{\circ}$C. The reaction was refluxed overnight and evaporated down to almost dryness. Diethyl ether was immediately added in large volume (>25 mL) to precipitate the desired HI salt. The resulting suspension was sonicated and placed in the freezer to ensure complete precipitation and thoroughly washed with diethyl ether to yield the product (**3py2TNH$_3$**) as a bright yellow powder (329.3 mg, 65.9 %∗, ^{1}H NMR - 500 MHz, DMSO-d$_6$: δ 8.96 (1H, d, J = 1.65 Hz), 8.58 (1H, d, J = 4.85 Hz), 8.22 (1H, d, J = 8.35 Hz), 7.80 (3H, s), 7.65 - 7.60 (2H, s), 7.17 (1H, d, J = 4.3 Hz), 7.02 (1H, d, J = 4.85 Hz), 3.10 (4H, m), 2.37 (3H, s)). If further purification was necessary, the product was dissolved in the least amount of hot methanol, precipitated and repeatedly washed with diethyl ether three times.

*Average of 2 runs.

2.2   Nuclear Magnetic Resonance (NMR) analysis

With regards to NMR, all coupling constants have been calculated by finding the difference in chemical shift between the split peaks, which was multiplied by the magnet field strength. If more than one option to calculate the coupling constant was possible (for example using peaks 1 and 2 *versus* 5 and 6), at least two different possibilities were calculated and the resulting coupling constant were averaged out and the mean was reported. Table 1 displays the splitting pattern nomenclature and abbreviation that was used.

Table 1: Nuclear Magnetic Resonance (NMR) splitting pattern nomenclature.

Splitting pattern name	Abbreviation
Singlet	s
Doublet	d
Triplet	t
Multiplet	m
Doublet of doublets	dd
Doublet of doublet of doublets	ddd

A molecule-specific analysis of splitting arrangements and peak assignments can be found in the Results and Discussion (section 3.1).

As a small review of NMR interpretation - this information will be assumed known in the Results and Discussion sections: the chemical shift of peaks (relative position in the ppm axis) indicates the extent that the nuclei are shielded or not by the electron clouds. This piece of information gives insight into the functional groups to which the protons are close. The more deshielded, the more downfield and the higher ppm the signal is. Another key aspect of NMR is the integration value, or the area under the peak, which indicates the number of hydrogens yielding a given signal. Lastly, the splitting pattern of the peaks relates to the number of hydrogen neighbors and in most simplistic cases, the "n+1" rule applies. For instance, a hydrogen with two neighbors who share the same magnetic environment would be split into a triplet (2+1=3). However, hydrogens can be split by neighboring protons that do not share the same magnetic environment, leading

to more complex peak shape. Long-range coupling, defined by the splitting of a signal by hydrogens in carbons more distant than direct neighbors can also take place. These situations will be addressed in the Results and Discussion sections.

2.3   Thin film fabrication

Now that the ligands were synthesized, they need to be assembled into the 2D-perovskites. This is the step 3 in the project strategy! **These techniques were performed by Jiaonan Sun (from the Department of Chemical Engineering at Purdue University)** and not by the author. However, the methods are still described here so that the thin film characterization analysis placed in the discussion is given some context. *Therefore, this section can be skipped without significant loss in continuity.*

Project strategy
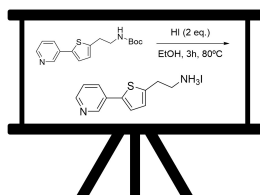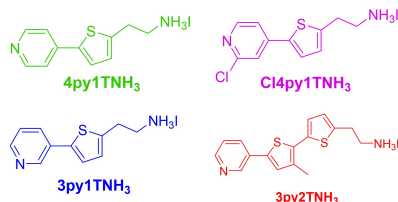
Figure 45: Project strategy - Step 3: Make 2D perovskites in thin films

A widely-used technique called spin-coating can generate 2D-perovskites in thin films [23, 52, 53, 59]. This process encompasses coating solutions of both lead iodide and the ligands on top of a glass substrate, which is later heated up. This is known as annealing. At that time, the system has enough energy so that the 2D-perovskites can be self-assemble. The thin films fabricated in this study followed the spin-coating procedure established by Ma and coworkers [23], with small modifications in ligand to PbI_2 ratios, which have been noted below. Figure 46 was provided as a visual aid for the spin-coating procedure.
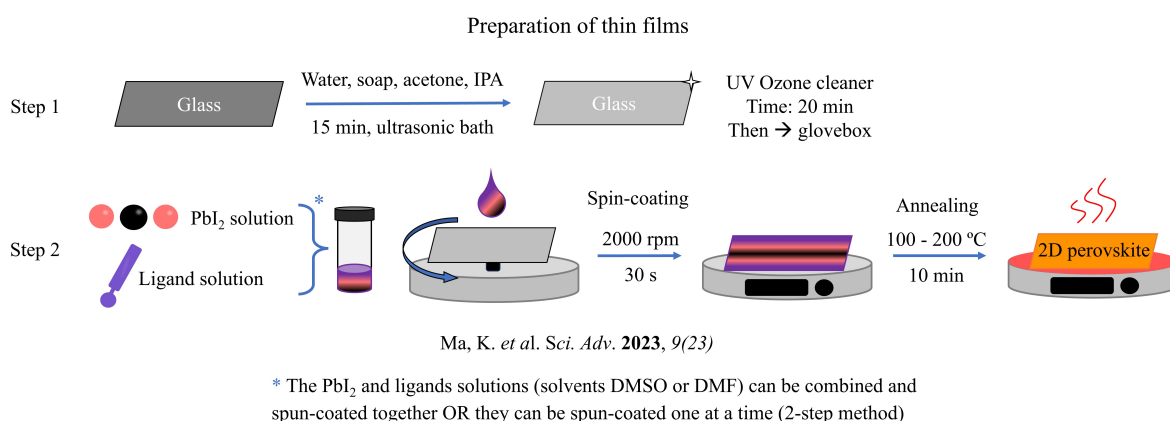
Figure 46: Thin film spin-coating procedure. The the first step, the glass substrates are thoroughly washed in an ultrasonic bath and rinsed with acetone and isopropyl alcohol (IPA). Then they are dried and placed in a UV Ozone cleaner and brought into a N_2 filled glovebox. In the second step (in glovebox), solutions of PbI_2 and the ligand (common solvents are DMSO or DMF) can be mixed and spun-coated together onto the plate, or they each under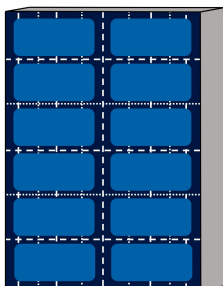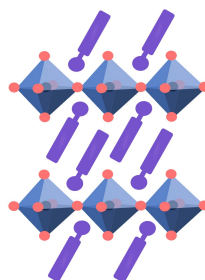 go spin coating individually. In this study, the solutions were mixed. Lastly, the film is allowed to anneal at high temperatures, which provides a favorable environment for the self-assembly of the desired 2D-perovskites.

In the first step of the thin film fabrication process, glass slides were cleaned using soap water, water, acetone, and isopropanol for 15 min in an ultrasonic bath. They were dried with a nitrogen gun, placed in an UV Ozone cleaner for 20 min and finally brought into a N_2 filled glovebox.

A precursor spin-coating solution of PbI_2 was prepared in a glovebox in anhydrous DMF at a concentration of 0.2 M and left stirring overnight at 70 °C for proper dissolution. It was then diluted to a concentration of 0.1 M by mixing a precursor ligand solution, so that the final mixture contained a 1:2 ratio of PbI_2 to ligand (namely, 3py1TNH$_3$, 4py1TNH$_3$ or Cl4py1TNH$_3$). In the case of 3py2TNH$_3$, the concentration of ligand was

increased in order to better observe the excitonic peak in UV-Vis spectroscopy.

The second step of thin film fabrication is to perform a technique called spin-coating: in a N_2 filled glovebox, 20 μL of the combined PbI_2 and ligand solution were added to the cleaned glass substrates, spun-coated at 2000 rpm for 30 seconds and then immediately transferred to a hot plate to anneal. The temperature range of the process was between 100 - 200 °C (ligand dependent) and the perovskites were given up to 10 minutes to self-assemble into hybrid perovskite thin films.

These films were analyzed by three different techniques, with no further treatment: UV-Vis spectroscopy, Emission spectroscopy (photoluminescence) and X-ray diffraction. The UV-Vis spectra were obtained using an Agilent Cary-5000 spectrometer, while the photoluminescence spectra were acquired on a SpectraPro HRS-300. The X-ray diffraction pattern was obtained on a Rigaku Smart Lab using Cu Kα source. The advantage of using this instrument compared to other diffractometers is that it can be used to directly measure the XRD pattern from thin films.

2.4 Perovskite solar cell fabrication

Next, perovskite solar cells were fabricated with the four different ligands synthesized in this study. This is step 4 in the project strategy! Again, it is highlighted that **this work was performed by Jiaonan Sun (from the Department of Chemical Engineering at Purdue University)**. However, the methods are still described in this section so that the device data shown the discussion is given some context. In addition, it gave the author a better understanding of the purpose each material and how the solar cells are fabricated in practice. *Therefore, this section can be skipped without significant loss in continuity.*
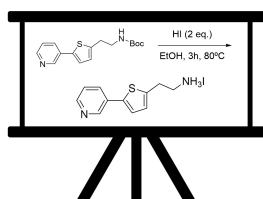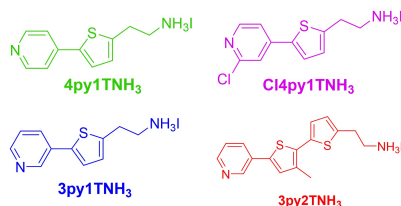
Figure 47: Project strategy - Step 4: Produce solar cell devices

The solar cell fabrication follows the same general procedure of thin films, although more steps are involved in the spin-coating due to a higher number of material layers. The procedure was performed in close agreement with the methods described by Ma and coworkers [23]. Figures 48 and 49 were added as a visual aid for PSC fabrication process. But it is also helpful to keep the structure of the perovskite solar cell in mind as these layers are built. The device architecture was presented in the introduction (section 1.5) and is shown in Figure 23.

Ma, K. *et al*. S*ci. Adv.* **2023**, *9(23)*
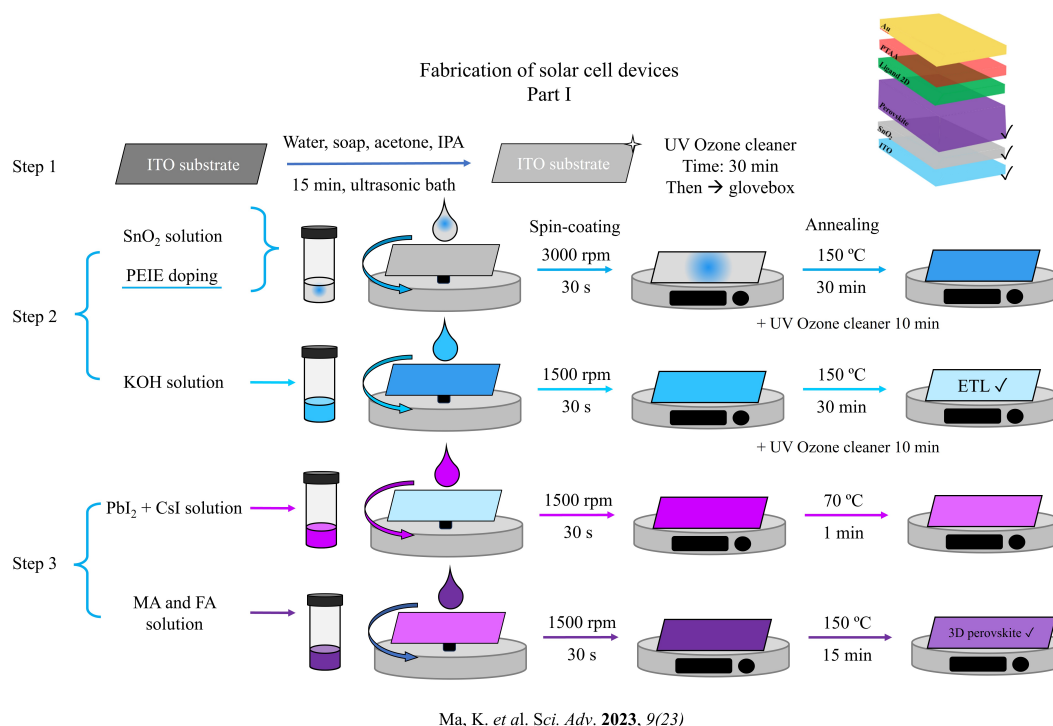
Figure 48: Perovskite solar cell fabrication procedure - steps 1 through 3. In step 1 the ITO substrates are thoroughly cleaned in an ultrasonic bath, subjected to an UV Ozone cleaning and brought into a glove box. All spin-coatings and annealing processes are conducted under N_2 environment. In step 2, the ETL layer coated in a two-step addition of PEIE-doped SnO_2 (spin-coating, annealing and UV Ozone cleaning) and KOH (spin-coating, annealing and UV Ozone cleaning) [77]. In step 3, the metal-halide perovskite layer is also coated in a two-step process. First, the PbI_2 is deposited, in the presence of small amounts of CsI (spin-coating and annealing). Second, the traditional small organic cations for metal-halide perovskites, MA and FA, are spun-coated and allowed to anneal. This process produced a mixed perovskite, with an approximate formula of $FA_{0.88}MA_{0.07}Cs_{0.05}PbI_3$, which is more resistant to environmental degradation [51] The next steps of device fabrication are shown in Figure 49.

In step one of the fabrication process, indium tin oxide (ITO) substrates were cleaned extensively using soap water, water, acetone, and IPA for 15 min in ultrasonic bath and dried with a nitrogen gun. They were then treated under UV Ozone for 30 minutes and

brought into a N_2 filled glovebox for spin coating. All the subsequent steps (spin-coating and annealing) were performed inside the glovebox, with the exception of cleaning the substrates under UV Ozone, which was performed under normal atmosphere.

In step two, the electron-transporting layer (ETL) was coated on the substrates. For that, a SnO_2 (15 wt%) stock solution was diluted with IPA:H_2O (v/v = 1:1) to concentration of 2.14 wt%, creating a solution to which polyethylenimine ethoxylated (PEIE) (15 μL, 0.61%) was added. After thorough mixing, 45 μL of the diluted SnO_2 solution was spun-coated onto the ITO substrates at 3000 rpm for 30 s, followed by annealing at 150°C for 30 min. The resulting substrates were further treated under UV Ozone for 10 minutes. In addition, directly on top of the SnO_2 layer, a 10 mM KOH solution was spun-coated on to the substrates at 3000 rpm for 30 s, followed by annealing at 150°C for 30 min. The addition of a base has been shown to optimize device performance, as it helps modulate electronic behavior of the ETL [77]. The substrates were again UVO treated for 10 min before re-transferred into the glovebox.

In step three, a 3D metal-halide perovskite layer was assembled using the two-step method. For that, a solution of PbI_2 (691.5 mg of PbI2, 19.5 mg of CsI, 900 μL of DMF, and 100 μL of DMSO) was spun-coated on top of the KOH and SnO_2 layers at 1500 rpm for 30 s, followed by annealing at 70°C for 1 min. After cooling down, a solution of the characteristic small organic cations for metal-halide perovskites, MA and FA cations (90 mg of FAI, 30.4 mg of MAI and 1 ml of IPA), was spun-coated on top of the PbI_2 film at 1500 rpm for 30 s. The substrates were allowed to anneal 150°C for 15 min. Note that heating provides enough energy so that the desired 3D-perovskites can self-assemble correctly in this layer. And in this case, a mixed 3D perovskite was likely obtained, since multiple cations were used. The approximate formula would be $FA_{0.88}MA_{0.07}Cs_{0.05}PbI_3$. The main reason for adopting this mixed system is that these perovskites have been shown to have enhance environmental stability [51], as described in section 1.3.4.

Fabrication of solar cell devices
Part II
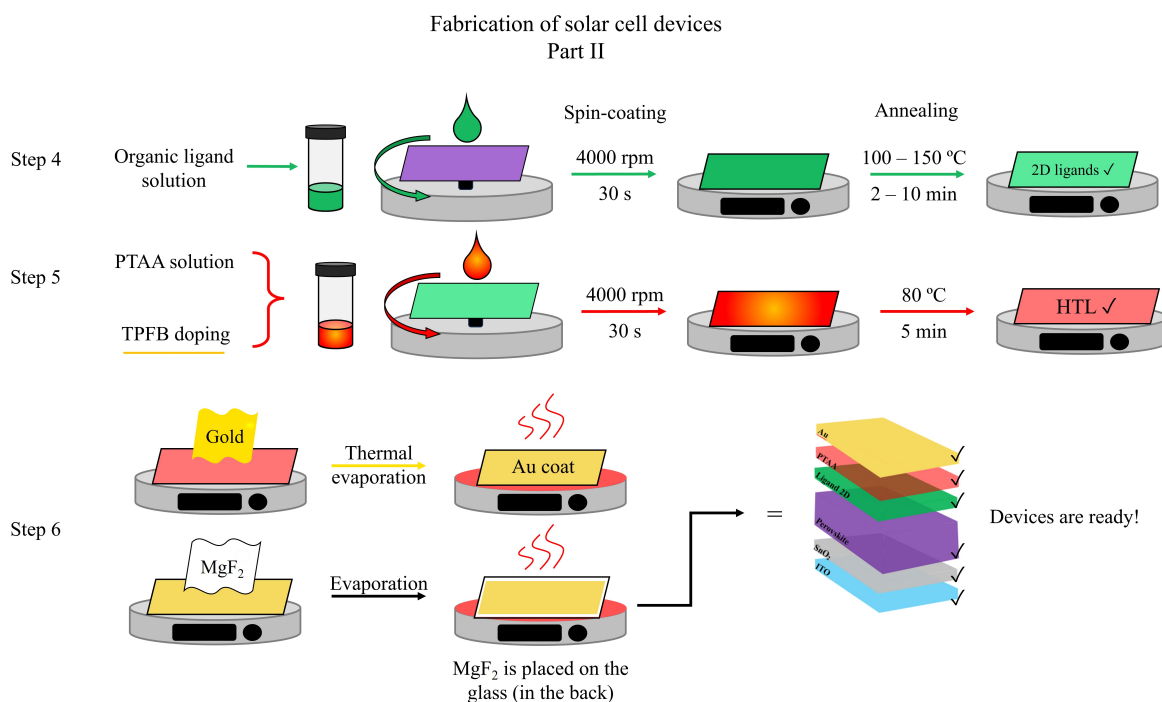
Ma, K. *et al*. S*ci. Adv.* **2023**, *9(23)*

Figure 49: Perovskite solar cell fabrication procedure - steps 4 through 6. All spin-coatings and annealing processes were conducted under N_2 environment. In step 4 the organic ligands (Cl4py1TNH$_3$, 4py1TNH$_3$, 3py1TNH$_3$ and 3py2TNH$_3$) were spun-coated and annealed on the perovskite films, producing the desired 2D-perovskites. In step 5, the HTL layer was coated with TPFB-doped PTAA (spin-coating and annealing). Lastly, gold was thermally evaporated on top of the HTL layer in order to close the electronic circuit and facilitate area measurements during characterization. In addition, MgF$_2$ was evaporated on the back of the ITO substrates in order to prevent light reflection. This finalized the device fabrication procedure! Previous steps are shown in Figure 48.

In step four, the ligands were spun coated onto the previous materials, creating a 2D-perovskite layer. For that, each of the ligands (Cl4py1TNH$_3$, 4py1TNH$_3$, 3py1TNH$_3$ and 3py2TNH$_3$) were initially dissolved in a solution of ethanol and DMSO. The exact concentration of these solution was optimized in a case by case basis, due to issues with solubility and influence on device performance. Having achieved the best concentrations, the solutions were spun-coated on the 3D-perovskite surface at 4000 rpm for 30 s, followed by annealing at 100°C - 150 °C for 2-10 min. The temperatures and waiting times during annealing process were also optimized in a case by case basis. Note that the coating procedure forms a 3D and a 2D perovskite layer, consistent with the modern design of PSCs presented in section 1.5.

In step five of the device fabrication, the hole-transporting later (HTL) was coated. For that, a solution of poly-triaryl amine (PTAA) was prepared in chlorobenzene (30 mg/ mL) and doped with 11% of tris(pentafluorophenyl)borane (TPFB). The doping was performed to increase device performance [78]. This system of PTAA/ TPFB was chosen in particular to avoid the incorporation of small mobile Li^+ into the devices while maintaining the hole mobility of PTAA. (Another choice of HTL system incorporates a highly conjugated material called Spiro-OMeTAD and lithium salt dopants [79]. Both systems have their advantages and disadvantages [56], but the PSCs in this study adopt the PTAA system). The PTAA/ TPFB solution was stirred overnight at 45 $^{\text{o}}$C to ensure full solubility of all components and then spun-coated onto the 2D-perovskite film at 4000 rpm for 30 s. The annealing process was conducted at 80°C for 5 min.

Lastly, to cap the solar cell device, 90 nm of gold were thermally evaporated onto the substrates with shadow mask to help determine the device area during characterization. In addition, 105 nm of MgF_2 was evaporated on to the back of the ITO substrates as an anti-reflection layer. Four pixels were made on each device substrate, and at least 8 substrates were fabricated for each ligand to confirm the reproducibility. For ligand 4py1TNH$_3$ n=16, 3py1TNH$_3$ n= 8, Cl4py1TNH$_3$ n= 14, Cl4py1TNH$_3$ and cations n= 12 and 3py2TNH$_3$ n= 12.

Control devices (n= 16) followed the same procedure but did not receive the ligand spin-coating layer, indicating that they had only one 3D perovskite layer.

2.5   Device characterization

As in the previous sections, the device characterization was performed by **Jiaonan Sun (from the Department of Chemical Engineering at Purdue University)**. However, the methods are still described in this section so that the parameters used to analyze a solar cell device are given enough background. In addition, it gave the author a better understanding of the electrical operating conditions of the cells. *Therefore, this section can be skipped without significant loss in continuity.*

After the perovskite solar cells were prepared, they were characterized electronically. As mentioned in section 1.5, the standard method for this characterization is to obtain a J-V curve and the desired parameters (V_{OC}, J_{SC}, FF and PCE - see Glossary section for definitions), which was obtained following the procedure described by Ma [23] and Sun [59].

The J-V curves were measured under 1 sun intensity, AM 1.5G irradiation based on Xe lamp solar simulator (Enlitech SS-F5-3A) in a N_2 glovebox. The light intensity (100 mW cm^{-2}) was calibrated each time before use by using a standard Si reference cell certified by National Renewable Energy Laboratory (NREL). The active area of each device was measured by Olympus microscope (between 0.047 cm^2 and 0.05 cm^2), following the shadow mask and the deposited gold layer of the devices. The voltage was swept from 1.2 V to -0.1 V (reverse) and from -0.1 V to 1.2 V (froward), with an average scan rate around 0.17 V/s. From -0.1 V to 0.8 V and 0.8 V to 1.2 V, the voltage steps were 40 mV and 10 mV, respectively. The external quantum efficiency (EQE) measurement was conducted at zero bias in air on a home-built instrument, equipped with a preamplifier and a lock-in amplifier with 161 Hz of chopper frequency. The light source was also calibrated with a Si diode (818-UV-L).

The curves obtained were fitted to the Mott-Gurney law [80] shown in the equation below:

$$J = \frac{9\varepsilon_0\varepsilon_r\mu V^2}{8L^3}$$

Where, ε_0 is the vacuum permittivity, ε_r is the relative dielectric constant (25 is applied for current devices), μ is the charge mobility, V is the voltage applied and L is the thickness of perovskite (around 800 nm). Figure 50 shows an example of how the parameters V_{OC} and J_{SC} are read from the curve.
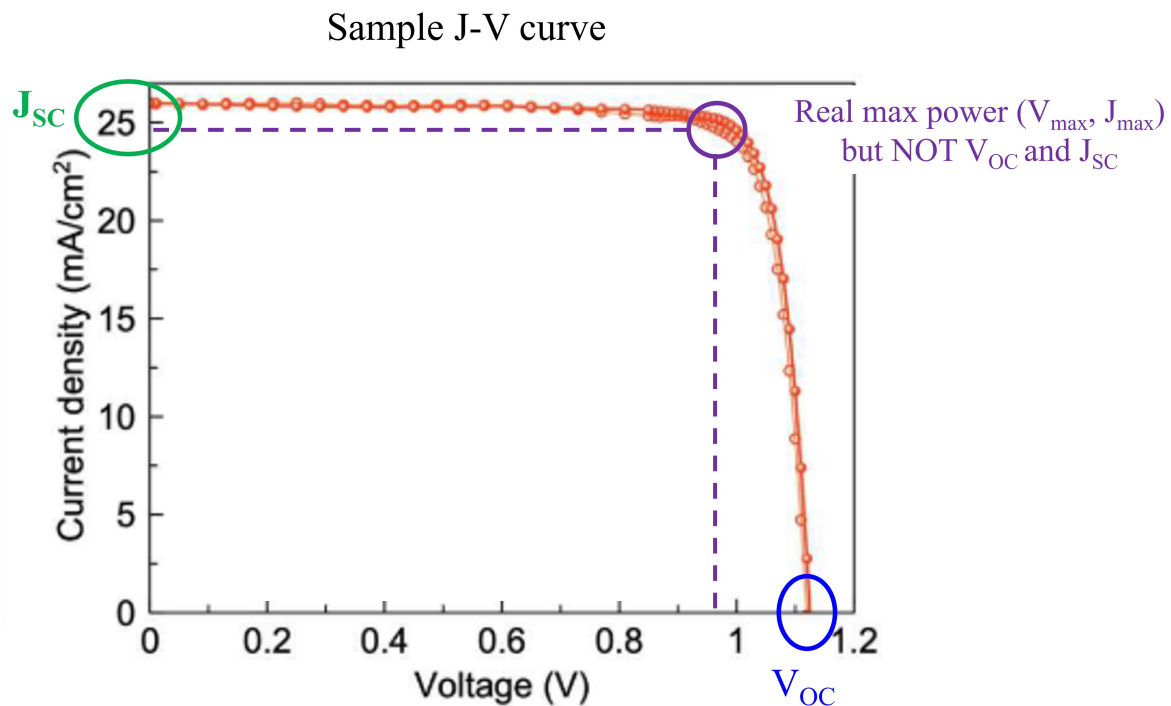
Sample J-V curve

Ma, K. *et al*. S*ci. Adv.* **2023**, *9(23)*

Figure 50: Sample J-V curve for PSC. This is a sample J-V curve that was obtained for 2D-perovskite solar cells in the study performed by Ma [23]. The J_{SC} point (green) represents the highest current produced by the solar cell under illumination and it is located on the y-axis. At that point the solar cell is shorted. The V_{OC} point (blue) represents the maximum voltage produced by the solar cell under illumination and is located on the x-axis. At that voltage, the current outputted by the power supply fully balances the one generated by the solar cell, hence no overall current is measured. The real maximum power obtained is given by the multiplication of the current and voltage at some point in the curve.

But is also necessary to understand what is happening electronically in the solar cell at those points [60]. That is, when zero voltage is applied on the device while it is still under illumination, the circuit is essentially shorted since the perovskite is outputting current but there is no resistance. This gives the maximum output current possible, the J_{SC} value (green mark in Figure 50). Note that J, current density (Amps/ m^2), is being measured (instead of current directly) since the output current is produced in an *area* of the solar cell.

However, as the voltage is raised up, the power supply is fighting against the perovskite current (this is known as reverse bias), creating one of its own. This decreases the overall current measured. At some voltage, there is enough current output from the power supply such that it fully balances the one generated by the perovskite under illumination. That voltage is known as the open-circuit voltage (V_{OC} - blue mark on Figure 50) (it is true though that one could just measure the voltage across the perovskite under illumination directly, but this set up is more convenient for measuring both the V_{OC} and J_{SC} together). The V_{OC} is, therefore, the maximum voltage that the PSC can output. Since the voltages are scanned throughout the whole process, the J-V curve is produced.

Another point of particular interest is the maximum output power (purple mark in Figure 50). Power, in physics is defined by the multiplication between voltage and current, so the maximum power will be given by the maximum value achieved on the J-V curve. In theory, the maximum power would be given by the direct multiplication of the V_{OC} and J_{SC}, but in experimentation that is not the case, since some power is lost by the generation of heat in the device or due to the material's resistance. Therefore, the real maximum power is given by the multiplication of a given current and voltage that lies in between these extrema. At that point, one can drop a lines directly to the axes and create a square. The desired parameter, the fill factor (FF) will be the ratio of that square (real maximum power - point (V_{max}, J_{max})), compared to the square created by the theoretical maximum power (which would be the point V_{OC}, J_{SC}), as shown in Figure 51. The FF can be also thought as a ratio of real to theoretical powers, as shown in the equation

Fill factor in J-V curve
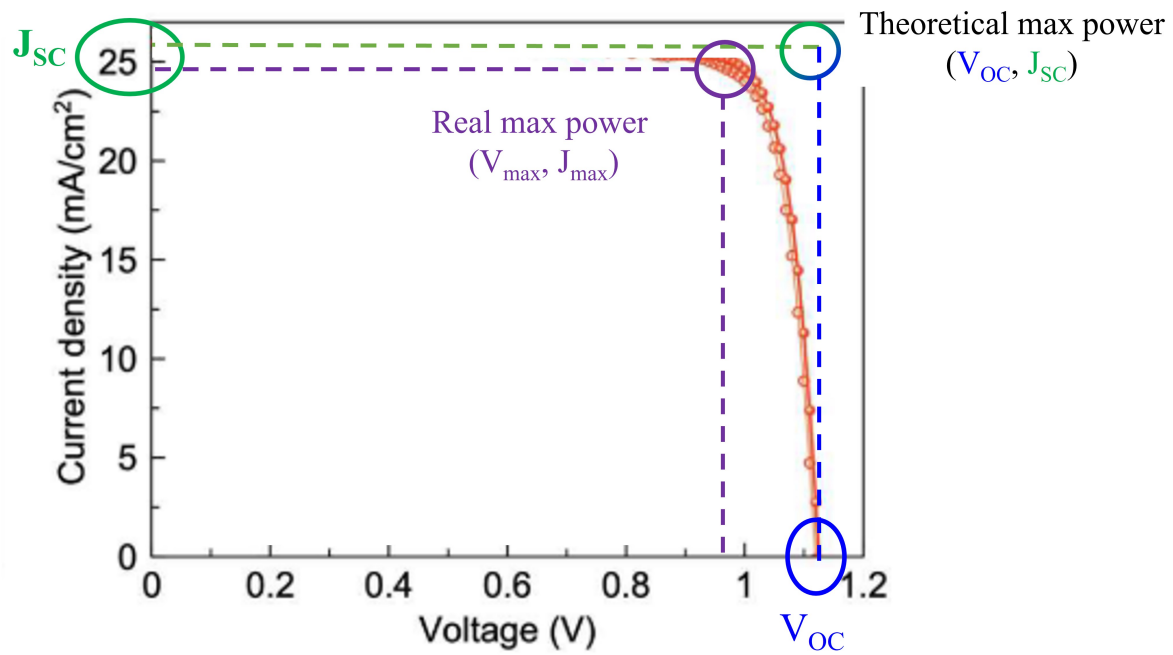
Ma, K. *et al*. S*ci. Adv.* **2023**, *9(23)*

Figure 51: Sample of Fill Factor (FF) parameter. Visual aid for the squares produced in the J-V curve when the real maximum power and the theoretical maximum power are contrasted in the solar cell. Their ratio gives the (FF) parameter [81]. This is why, sometimes, the FF is also described as the squareness of the solar cells.

below [81, 82] (and references therein) .

$$FF = \frac{J_{max}V_{max}}{J_{SC}V_{OC}}$$

With all these values in hand, one can finally calculate the Power Conversion Efficiency (PCE), which is the most significant parameter of the solar cell efficiency. The PCE incorporates all parameters mentioned above and compares them to the initial power output, given by the power supply ([82] and references therein). This is summarized in the the equation below:

$$PCE = \frac{J_{SC}V_{OC}FF}{P_{in}}$$

Note that each of the solar device replicates (for each of the four ligands) undergoes a J-V curve measurement. The resulting data is then analyzed to extract the desired parameters, V_{OC}, J_{SC} and the PCE and FF are calculated. Since many replicates were produced, the results are reported with box plots (statistical analysis). This ensures that only the overall characteristics of the solar cells, meaning the quality of the 2D perovskite materials and the efficiency that the ligands can create are highlighted.

2.6   Single crystals

The fifth and last step of the project strategy is to attempt single crystal formation of the novel 2D-perovskites. Even though these hybrid materials can be characterized in thin films, the most rigorous evidence of their formation would be through the synthesis and analysis of their single crystals, since they would provide the opportunity to directly observe the 2D-lattice [23, 53]. Therefore, the recrystallization of the 2D-perovskites assembled with the ligands Cl4py1TNH$_3$ and 3py2TNH$_3$ was attempted.
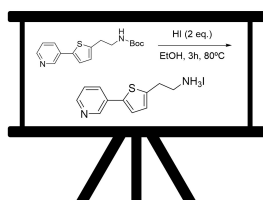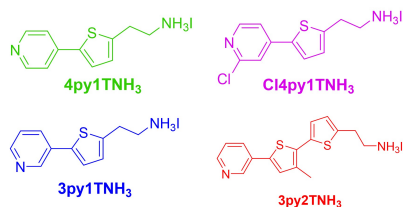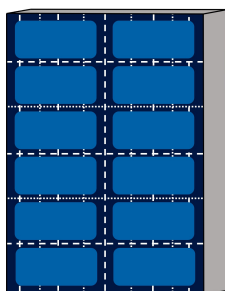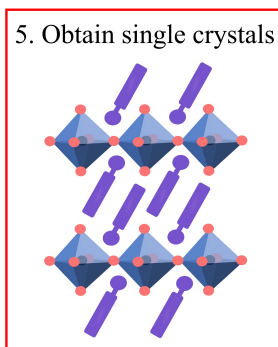
Figure 52: Project strategy - Step 5: Obtain single crystals

For the Cl4py1TNH$_3$ ligand, two different crystallization techniques were employed: slow cooling and solvent diffusion. In the slow cooling method, all the necessary components of the perovskite (Pb^{2+}, iodide, the ligands and possibly other smaller organic cations for high n-number recrystallization) were mixed together in a given solvent mixture and heated up to a boil. Then, they were allowed to cool down inside a thermal flask for the span of 1-2 days. The conditions for each trial using this method are summarized in Table 2.

Table 2: Slow cooling conditions for single crystals of 2D-perovskites with ligand Cl4py1TNH$_3$

| Compound	1	2	3	4	5	6	7	8
Cl4py1TNH$_3$ (mg)	1.1	1.1	1.0	2.7	3.0	2.0	2.1	2.1
Lead Iodide (PbI$_2$) (mg)	12.2	12.5	4.6	5.0	5.0	5.4	5.6	4.9
Formamidinium iodide (FAI) (mg)	16.5	16.1	–	–	–	–	–	–
Ethanol (mL)	2.0	2.0	1.0	1.0	1.0^b	1.0^c	–	1.0
Hydroiodic acid (HI) (μL)	–	–	200	200	200	200	200	–
Hypophosphorous acid (H$_3$PO$_2$ (μL)	–	–	100	100	100	100	100	–
Cooling time (days)	2	2	2	2	2	2	1	2
N-number attempted formation	high-n^a	high-n^a	1	1	1	1	1	1

^{a} High-n would indicate n>1. ^{b} A solution of 0.2% DMF in ethanol was used. ^{c} A solution of 1.0 % DMF in ethanol was used.

Table 3: Anti-solvents and volumes used in diffusion recrystallization of 2D-perovskites with ligand Cl4py1TNH$_3$

Solvent	Chloroform (mL)	Chlorobenzene (mL)	Hexane (mL)	Anisole (mL)	Toluene (mL)
1	1.0	–	–	2.0	–
2	1.0	1.0	–	–	–
3	1.0	2.0	–	–	–
4	1.0	–	–	–	1.0
5	–	1.0	1.0	–	–
6	–	2.0	1.0	–	–
7	–	2.0	–	1.0	–
8	1.0	1.0	–	–	–
9	–	–	1.0	1.0	1.0
10	1.0	–	–	1.0	–
11	3.0	–	–	–	–

Similarly, in the solvent diffusion technique, the 2D-perovskite components, PbI$_2$ (0.01

M) and the ligand Cl4py1TNH$_3$ (0.02 M), were dissolved in ethanol and then mixed together in a small vial. This vial was then placed into a second, larger vial that contained a given solvent mixture, known as the anti-solvent. The idea is that with time, the anti-solvent evaporates and diffuses into the smaller vial, causing the 2D-perovskite to recrystallize. Note that this process can take up to two weeks (if the diffusion is too fast, then the materials only precipitate and do not yield a crystal). Table 3 summarizes the anti-solvent mixtures that were used in eleven diffusion recrystallization trials for the ligand Cl4py1TNH$_3$.

Additionally, single crystals of 2D-perovskites containing the ligand 3py2TNH$_3$ were attempted via the slow cooling method. The conditions for each of the trials are displayed in Table 4.

Table 4: Slow cooling details for ligand 3py2TNH$_3$.

Compound	1	2	3	4
3py2TNH$_3$ (mg)	1.0	1.9	1.0	2.1
Lead Iodide (PbI$_2$) (mg)	11.9	11.9	5.1	4.9
Formamidinium iodide (FAI) (mg)	16.6	16.6	—	—
Ethanol (mL)	2.0	2.0^b	1.0	1.0^b
Hydroiodic acid (HI) (μL)	—	—	200	200
Hypophosphorous acid (H$_3$PO$_2$ (μL)	—	—	100	100
Cooling time (days)	1	1	1	1
N-number attempted formation	high-n^a	high-n^a	1	1

^{a} High-n would indicate n>1. ^{b} A solution of 0.2% DMF in ethanol was used.
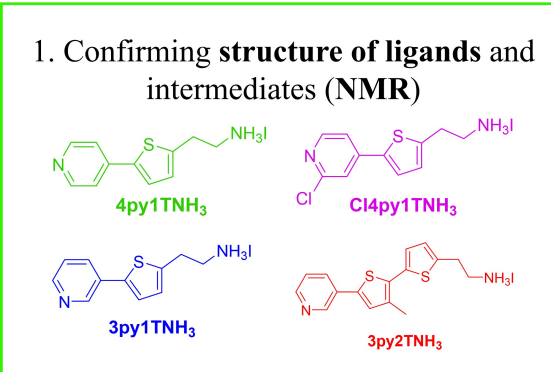
3   Results and Discussion

3.1   Nuclear Magnetic Resonance (NMR) analysis

This section is devoted to the first step in data analysis: confirming the structures of all molecules synthesized in this study using NMR.
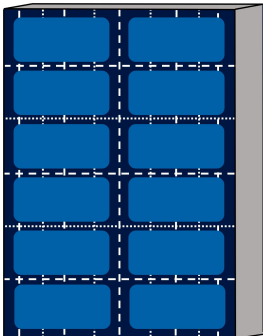
Data analysis
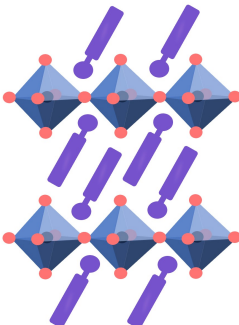
Figure 53: Data analysis - Step 1: Confirming the structure of ligands and intermediates via NMR.

3.1.1 2-ring ligands and relevant intermediates

The first molecule to be addressed is 4py1TBoc. Its full spectra can be found in Figure 54 and a detailed view of the peaks is displayed in Figure 55. In the full view, the peaks that were not integrated correspond to residual solvents. The small signals at around 2, 4 and 1.3 ppm correspond to leftover ethyl acetate, while the one at about 1.5 ppm corresponds to water [83]. Deuterated chloroform, which was the solvent used to run the spectrum appears at the usual chemical shift at 7.26 ppm.

Figure 54: Full NMR spectrum for the molecule 4py1TBoc. This is intended to show all peaks present in the scan, considering possible impurities, standards and solvent peaks (not integrated), which are addressed in the text. This spectrum was collected by Jiaonan Sun.
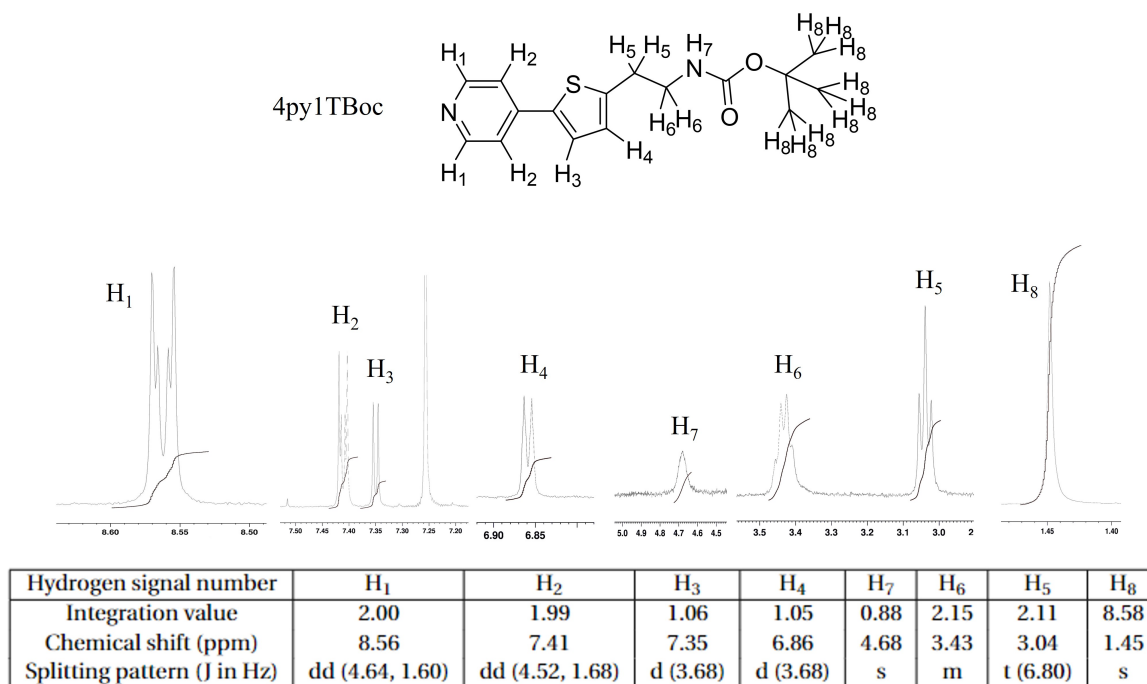
Figure 55: Partial NMR spectrum for the molecule 4py1TBoc. The peaks have been cropped out from the complete spectrum (displayed in Figure 54) and zoomed in to show the splitting patterns more clearly. The peaks retain their chemical shift order. The hydrogen labels correspond to respective protons in the molecule drawn at the top. The integration values, chemical shift and splitting patterns and coupling constants are displayed in the table. A reference of splitting pattern abbreviation can be found in Table 1. This spectrum was collected from Jiaonan Sun.

As displayed in Figure 55, all the hydrogens in the molecule 4py1TBoc have been assigned. H_1's are assigned the highest chemical shift due to the proximity of the nitrogen in the pyridine. H_2's correspond to the following peak (7.41 ppm) since the effect of the pyridine nitrogen has faded. The integration values correspond to two protons in both cases, adequately matching the structure of the molecule. H_3 and H_4 both integrate for 1 and correspond to hydrogens in the thiophene ring. Their assignment follows the same logic of the fading effect of the pyridine. However, to fully confirm the identity of these protons, a more complex experiment, such as a 2D NMR is necessary. Nonetheless, both signals integrate for the correct number of hydrogens and display the same splitting pattern suggesting the correct structure.

Methylene 5 is assigned to the peak at 3.04 ppm and is relatively shifted downfield due to the adjacent thiophene ring. In addition, it has two neighboring protons (H_6's) which would cause the signal to split into a triplet. According to the inset table, the signal

is split into a triplet hence matching methylene 5. In contrast, methylene 6 is assigned the peak at 3.43 ppm, more downfield, since it experience more of the polarizing effect of the carbamate (BOC) group, which is stronger than that of the thiophene. However, its peak shape is uneven and hence is considered a multiplet. The main reason for this distortion is hypothesized to be the presence of neighboring protons in different magnetic environments, namely H_5 and H_7. That is, most likely when the signals split based on the different J values of neighboring protons, they end up falling upon each other, leading to the overlapped shape observed and a multiplet-like splitting. Note that this is a case in which the simplified "n+1" rule does not apply due to the asymmetrical shape of the peak.

H_7 has a matching peak at 4.68 ppm, which falls within the upper range of appropriate region of amine protons, due to carbamate deshielding [84]. The integration value is less than 1, but this is to be expected since H_7 could behave as an exchange proton with the solvent, leading to a smaller integration value. The remaining hydrogens, H_8, belong to the BOC group. They integrate for 8.5 protons, which is slightly lower than expected (total of 9), but still confirms the presence of the carbamate. Therefore, the spectrum confirmed the correct synthesis of intermediate molecule 4py1TBoc.

The full spectrum of 4py1TNH$_3$ can be found in Figure 56. The non-integrated peak at 2.5 ppm corresponds to the residual signal of d$_6$-DMSO, which was used the solvent [83]. A detailed view of the peaks is shown in Figure 57.
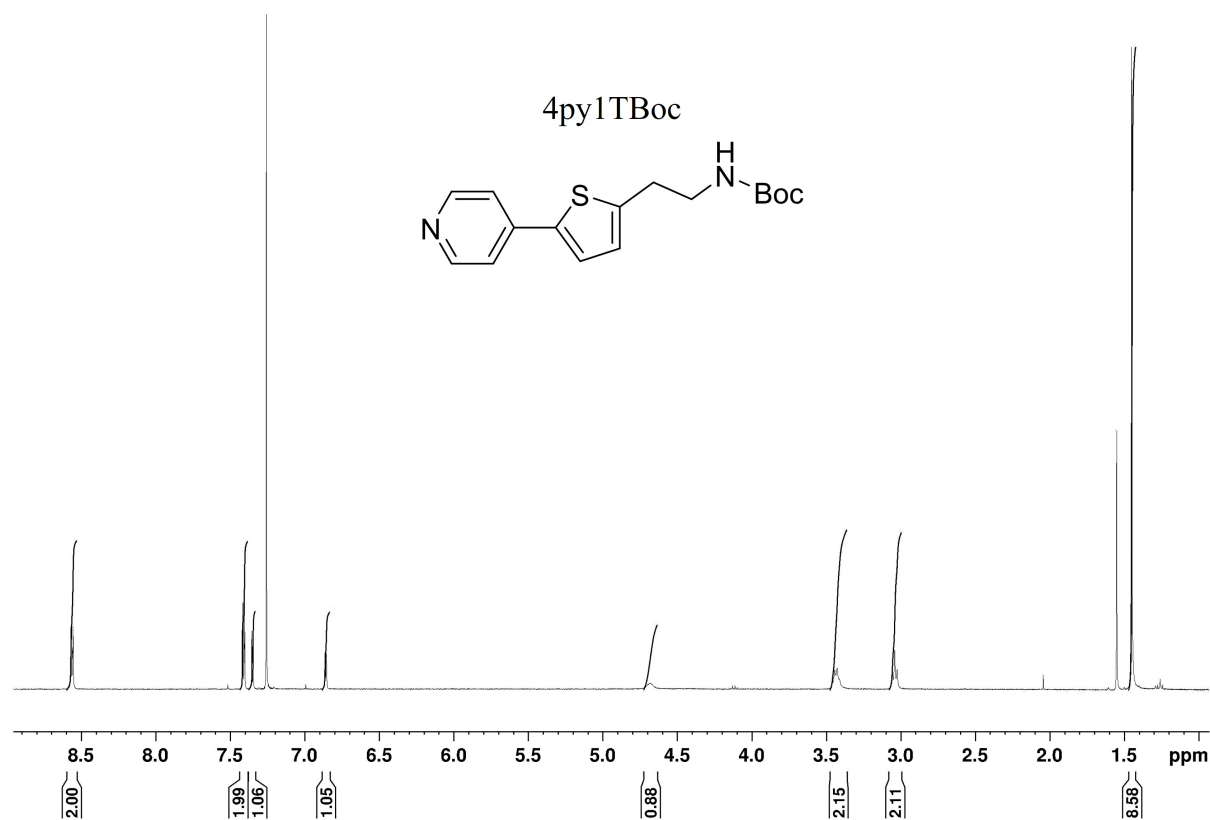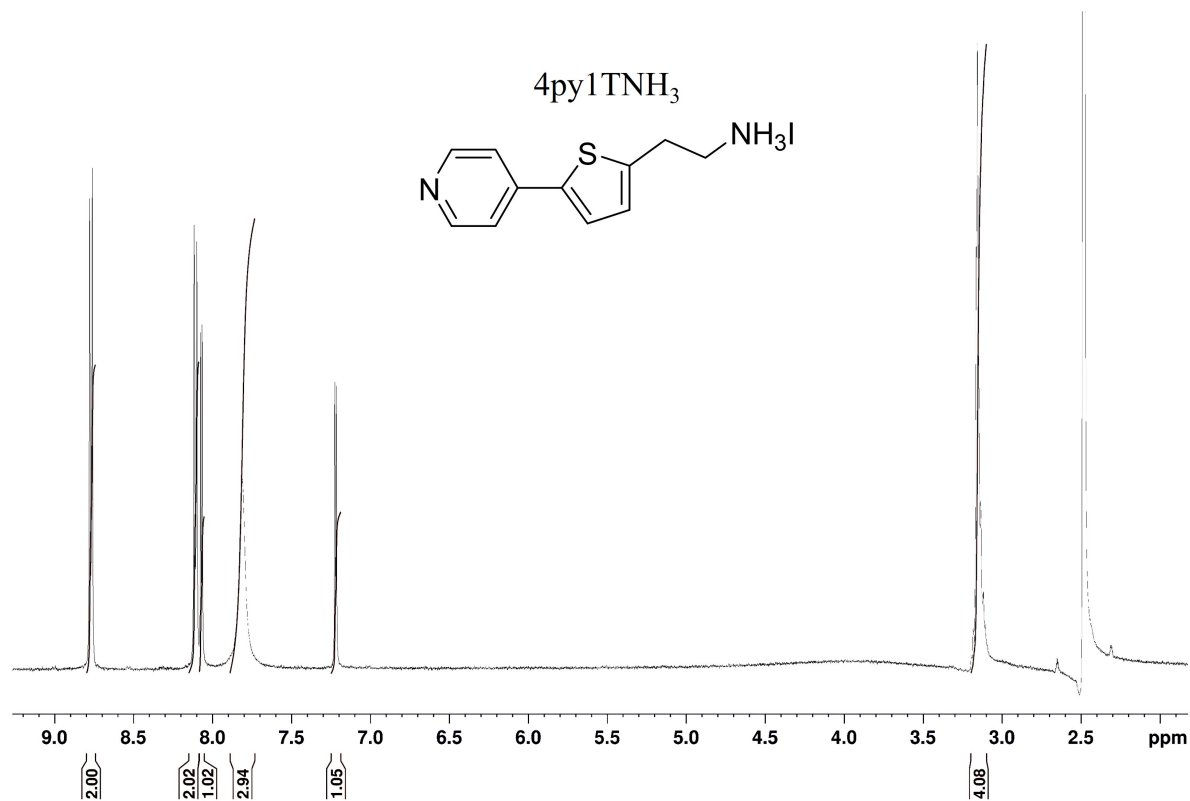

Figure 56: Full NMR spectrum for the molecule 4py1TNH$_3$. This is intended to show all peaks present in the scan, considering possible impurities, standards and solvent peaks (not integrated), which are addressed in the text.
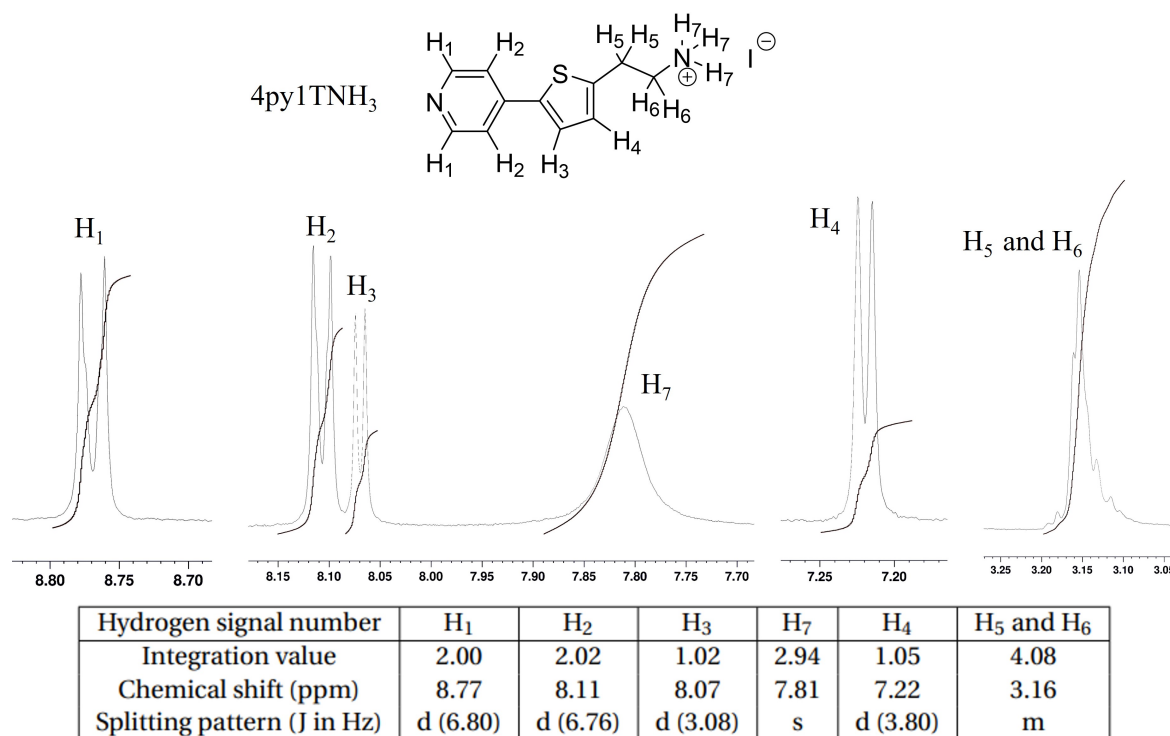
Figure 57: Partial NMR spectrum for the molecule 4py1TNH₃. The peaks have been cropped out from the complete spectrum (displayed in Figure 56) and zoomed in to show the splitting patterns more clearly. The peaks retain their chemical shift order. The hydrogen labels correspond to respective protons in the molecule drawn at the top. The integration values, chemical shift and splitting patterns and coupling constants are displayed in the table. A reference of splitting pattern abbreviation can be found in Table 1.

Hydrogen signal number	H_1	H_2	H_3	H_7	H_4	H_5 and H_6
Integration value	2.00	2.02	1.02	2.94	1.05	4.08
Chemical shift (ppm)	8.77	8.11	8.07	7.81	7.22	3.16
Splitting pattern (J in Hz)	d (6.80)	d (6.76)	d (3.08)	s	d (3.80)	m

Protons H_1 and H_2 in the molecule 4py1TNH₃ (Figure 57) are assigned the first and second peaks, due to their proximity to the pyridine nitrogen. The peaks at 8.07 and 7.22 ppm are within the aromatic region and each of them integrate for 1 proton. Therefore, they are assigned to protons H_3 and H_4, respectively, due to the fading effect of the pyridine. But but to fully confirm this proposition, a 2D NMR would have to be performed (follows the same case as with 4py1TBoc).

In comparison to the precursor molecule, 4py1TBoc, the biggest changes n this spectrum are the shift of the amine protons from previous 4.68 ppm (see Figure 55) to 7.81 ppm and the combination of the methylene hydrogens into one peak. With respect to the amine shift, this is expected: as a salt the nitrogen carries one extra bond and becomes positively charged, which significantly alters its electronegativity. Thus, to compensate for the extra bond, the electron density becomes skewed toward the nitrogen (it becomes

even more electronegative), further deshielding and pushing the protons downfield. With respect to the methylene hydrogens, the protonation seems to have averaged out their difference in chemical shift. That is, it is hypothesized that the electron withdrawal of the thiophene ring on H_5's seems to have the same strength as the effect caused by the protonated amine pulling on neighboring protons, H_6's. This then leads their signals to overlap at 3.16 ppm. The uneven peak shape (multiplet) and integration value of 4 hydrogens support this explanation, as the latter indicates the correct number of protons. Also, there are no other signals upfield.

Another imporant remark is the disappearance of the Boc group signal. That is, a successful deprotection would eliminate this signal, as evidenced by the mechanism in Figure 33. Because this signal is not observed, the deprotection is deemed successful. Moreover, all peaks have their respective hydrogens assigned and only the solvent signal remains. This, the ligand 4py1TNH$_3$ is determined to be successfully synthesized in high purity.

Note that NMR interpretation for the molecules 4py1TBoc and 4py1TNH$_3$ are representative for the remaining two 2-ring ligands, Cl4py1TNH$_3$ and 3py1TNH$_3$ and their respective intermediate molecules. Their full spectra can be found in the Appendix (section 6.1). They are also considered to be successfully synthesized.

3.1.2 Intermediates

The synthesis of the desired ligands in this project required the use of intermediate thiophene derivatives that are not commercially available. The first derivative to have its NMR interpreted is 1TBoc. The full spectrum can be found in Figure 58. Clearly, there are many unassigned peaks, but they correspond to residual solvents and reagents that had not been washed away in the extraction procedure. Dichloromethane, the reaction solvent and organic phase of the extraction, can be found at 5.30 ppm [83]; residual triethylamine peaks also show at 2.53 and 1.05 ppm as quartets and triplets. Water is also present at around 1.5 ppm. In spite of these solvents, the remaining peaks indicate that the desired compound is synthesized correctly, as indicated in the explanation below.
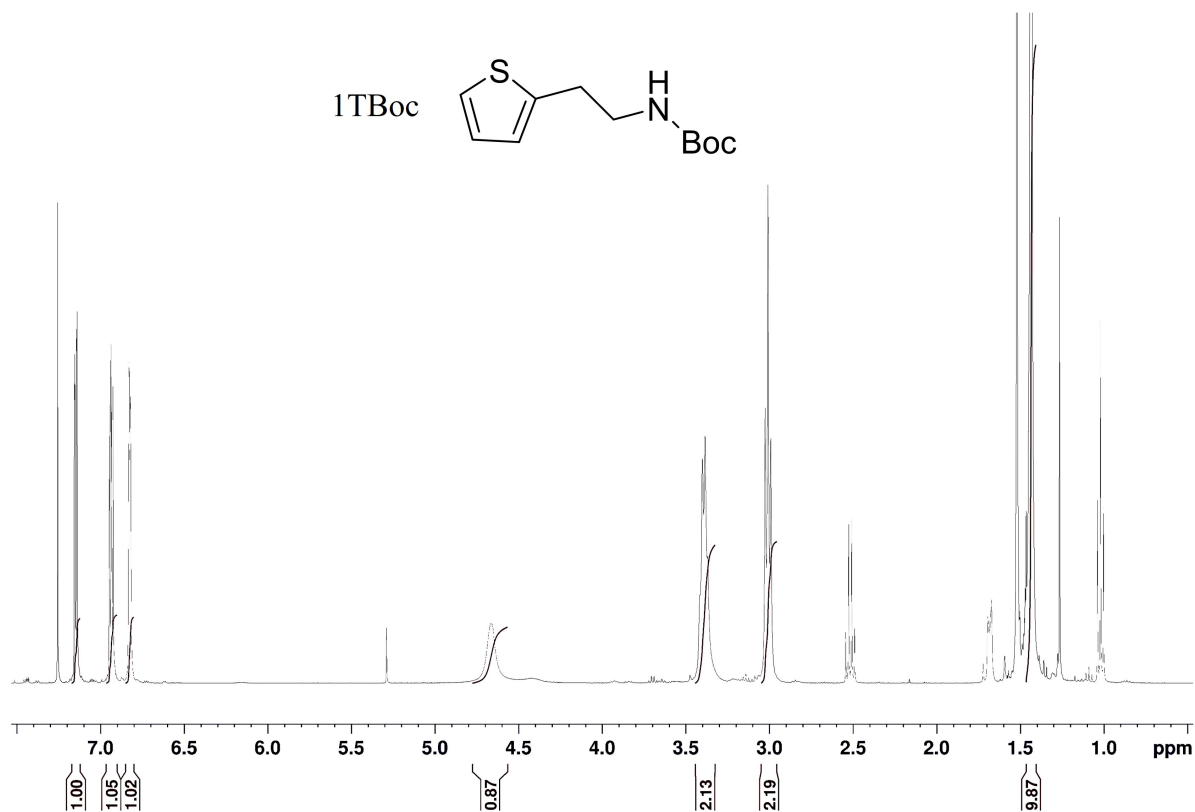

Figure 58: Full NMR spectrum for the molecule 1TBoc. This is intended to show all peaks present in the scan, considering possible impurities, standards and solvent peaks (not integrated), which are addressed in the text. This spectrum was provided by Jiaonan Sun.
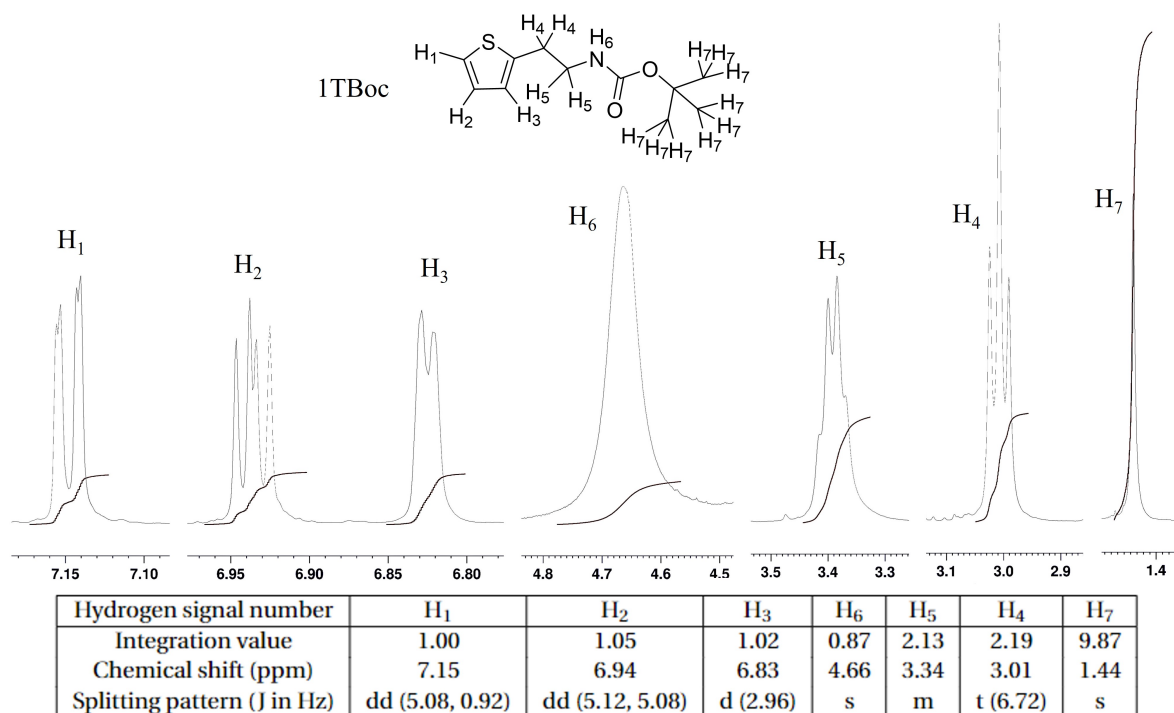
Figure 59: Partial NMR spectrum for the molecule 1TBoc. The peaks have been cropped out from the complete spectrum (displayed in Figure 58) and zoomed in to show the splitting patterns more clearly. The peaks retain their chemical shift order. The hydrogen labels correspond to respective protons in the molecule drawn at the top. The integration values, chemical shift and splitting patterns and coupling constants are displayed in the table. A reference of splitting pattern abbreviation can be found in Table 1. This spectrum was provided by Jiaonan Sun.

Hydrogen signal number	H_1	H_2	H_3	H_6	H_5	H_4	H_7
Integration value	1.00	1.05	1.02	0.87	2.13	2.19	9.87
Chemical shift (ppm)	7.15	6.94	6.83	4.66	3.34	3.01	1.44
Splitting pattern (J in Hz)	dd (5.08, 0.92)	dd (5.12, 5.08)	d (2.96)	s	m	t (6.72)	s

Figure 59 displays in detail the peaks belonging to the molecule 1TBoc. The three aromatic protons are assigned based on their distance from the sulfur atom, as well as differences in splitting pattern. H_1 is the closest to the sulfur atom and should experience the most electron withdrawal. Moreover, its peak should display *ortho* coupling (due to the presence of H_2) and weaker *meta* coupling (due to the presence of H_3) producing a asymmetrical doublet of doublets. This is the case with the first signal, at 7.15 ppm, whose splitting constants are calculated to be 5.08 Hz (*ortho* and 0.92 Hz (*meta*) and which appears as a dd. H_2, most interestingly, experiences two *ortho* couplings of relatively similar J values, since the only difference between the hydrogen neighbors is their closeness to the sulfur atom. This matches second peak at 6.94 ppm, which is assigned to H_2. Lastly, the third proton should have one *ortho* and one *meta* splitting and be more upfield compared to H_1 (further away from sulfur atom). This matches the peak 6.83 ppm,

which is assigned to H_3. Note that the signal has a slightly different shape (a true double it skinnier and sharper), which might support the hypothesis that the *ortho* and *meta* splitting led to an overlap.

1TBoc also contains an amine proton H_6, which appears at 4.66 ppm. The integration value is lower, but this is acceptable considering that this hydrogen can be exchanged with the solvent. The splitting pattern observed for H_4 and H_5 follows the description provided when interpreting the NMR from the molecule 4py1TBoc. The same is valid for the BOC protecting group hydrogens, H_7.

Another key thiophene derivative is Sn1TBoc since it is used to build the last ring in ligand 3py2TNH$_3$. However, when attempting its synthesis (see reaction scheme in Figure 40), one runs into an issue: the tin product cannot be easily separated from the starting material 1TBoc because in both molecules, the polarity is dominated by the BOC protecting group. Therefore, column chromatography is not an option and recrystallization can be quite challenging due the significant amount of both molecules still present after extraction. Therefore, the amount of product synthesized has to tracked by tracked by NMR.
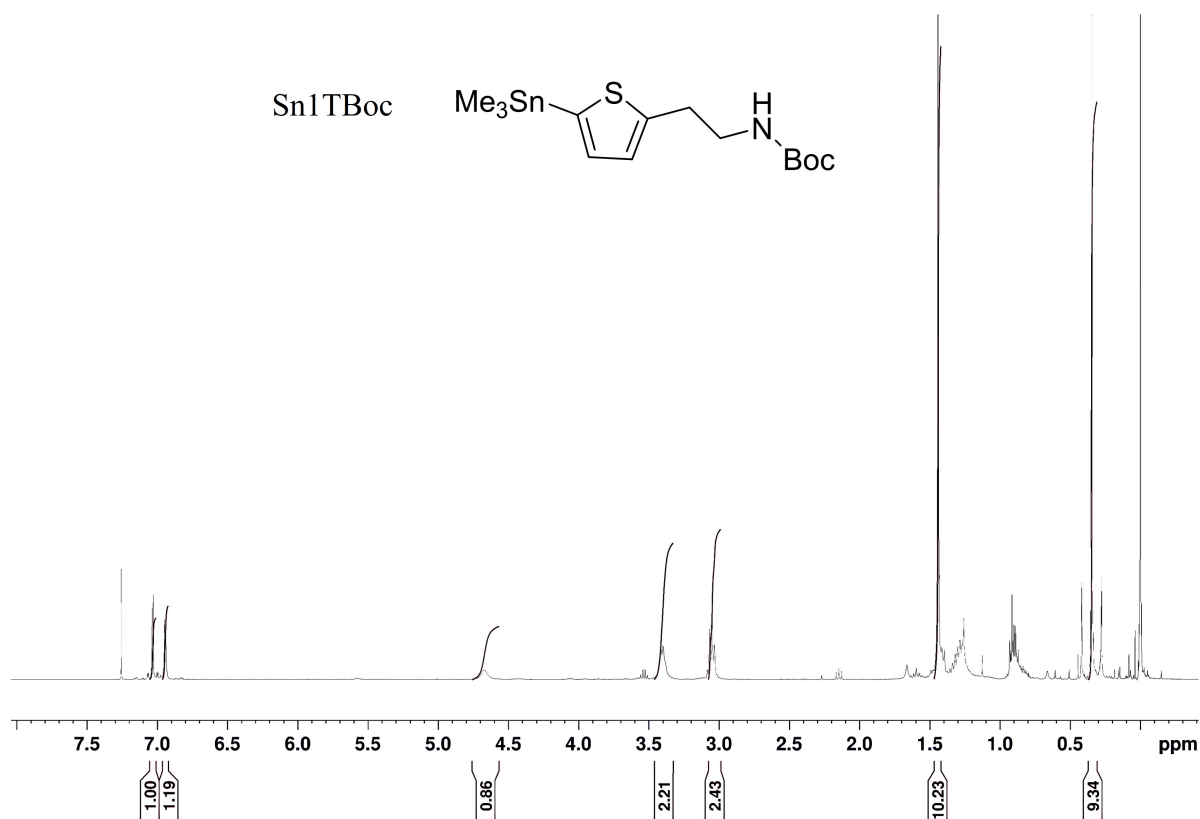
Figure 60: Full NMR spectrum for the molecule Sn1TBoc. This is intended to show all peaks present in the scan, considering possible impurities, standards and solvent peaks (not integrated), which are addressed in the text.

Figure 60 shows the full NMR spectrum of the Sn1TBoc synthesis. The spectrum displays non-integrated peaks that likely correspond to butane by-product created by the reagent n-butyllithium. That is, upon extraction the butane joined the organic phase and since no further purification took place, it is reasonable to assume it got carried through.

Its signals should appear between 1.5 - 0 ppm (hydrocarbon peaks) and they are indeed observed.

Hydrogen signal number	H$_2$	H$_3$	H$_6$	H$_5$	H$_4$	H$_7$	H$_1$
Integration value	1.00	1.19	0.86	2.21	2.43	10.23	9.34
Chemical shift (ppm)	7.03	6.94	4.68	3.41	3.05	1.45	0.35
Splitting pattern (J in Hz)	d (3.16)	d (3.12)	s	m	t (6.72)	s	s

Figure 61: Partial NMR spectrum for the molecule Sn1TBoc. The peaks have been cropped out from the complete spectrum (displayed in Figure 60) and zoomed in to show the splitting patterns more clearly. The peaks retain their chemical shift order. The hydrogen labels correspond to respective protons in the molecule drawn at the top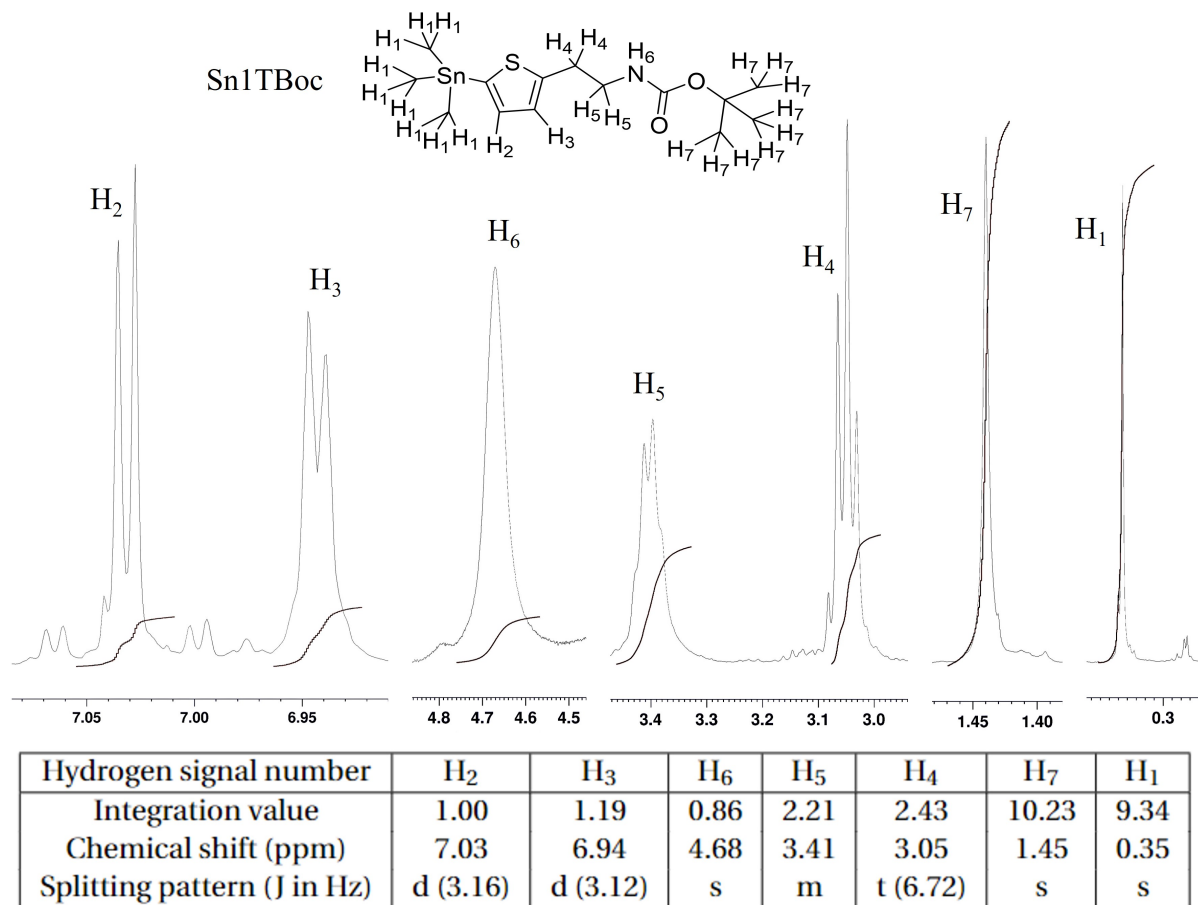. The integration values, chemical shift and splitting patterns and coupling constants are displayed in the table. A reference of splitting pattern abbreviation can be found in Table 1.

The zoomed in spectrum can be found in Figure 61. The first peak in the aromatic region was assigned to H$_2$, while the second was assigned to H$_3$. Both of these signals integrate for 1 proton and display approximately the same coupling constant. This proposed assignment matches the structure, but in order to fully confirm each individual proton, a 2D NMR would have to be performed. The same reasoning concerning the chemical shift and splitting patterns of the peaks matched to hydrogens 5 through 8 in 4py1TBoc (Figure 55), apply for protons 4 through 7 in Sn1TBoc. The only difference lies in the integration values especially because they can be used to calculate the amount

of product that was in fact synthesized.

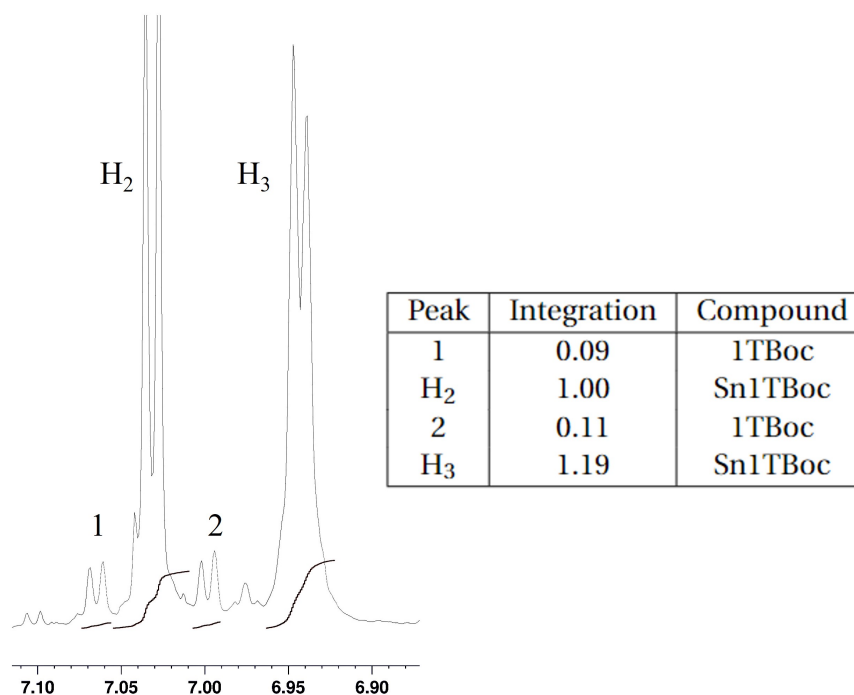| Peak	Integration	Compound
1	0.09	1TBoc
H_2	1.00	Sn1TBoc
2	0.11	1TBoc
H_3	1.19	Sn1TBoc

Figure 62: Purity assessment of Sn1TBoc via NMR analysis. The aromatic peaks have been cropped out from the complete spectrum (displayed in Figure 60), zoomed in and integrated to show the relative amounts of 1TBoc and Sn1TBoc. The integration values have been directly transcribed from TopSpin.

As stated before, some leftover starting material is expected. The signals coming from 1TBoc can be clearly observed close to the baseline in the aromatic region displayed in Figure 61 and their integration is shown in Figure 62. These value help determine the relative amounts of product and reactants. Since the integration values of the peaks corresponding to 1TBoc signals are 0.09 and 0.11, the reaction is calculated to contain about 10 % of starting material. Note that this direct comparison can be made since these signals both correspond to only one hydrogen in 1TBoc. This effect can also be observed in the upfield signals in Figure 61, since the integration values for the protons 4, 5 and 7, are slightly higher. That is, the larger integration values is interpreted as the signals for Sn1TBoc overlapping with those of 1TBoc. However, using the aromatic signals of 1TBoc to calculate the amount of starting material present is a better approach compared to the upfield signals since the aromatic peaks are more isolated and do not easily overlap

with other impurities. Therefore, considering the presence of leftover starting material and butane, Sn1TBoc is estimated to be synthesized by this reaction with a purity level of no more than 85 %.

Figure 63: Full NMR spectrum for the molecule Br1TBoc. This is intended to show all peaks present in the scan, considering possible impurities, standards and solvent peaks (not integrated), which are addressed in the text.

Another significant thiophene intermediate is Br1TBoc as it works as one of the coupling partners in the Suzuki reaction, creating the 2-ring ligands. Its full NMR spectrum is displayed in Figure 63. Water and dichloromethane (DCM) are present in the sample, as evidenced by the peaks at 5.30 and about 1.5 ppm. Also, minimal amounts of ethyl acetate and hexanes can be spotted at 1.26 ppm. The remaining signals, which correspond to Br1TBoc protons, have been expanded and are shown in detail in Figure 64.

Figure 64: Partial NMR spectrum for the molecule Br1TBoc. The peaks have been cropped out from the complete spectrum (displayed in Figure 63) and zoomed in to show the splitting patterns more clearly. The peaks retain their chemical shift order. The hydrogen labels correspond to respective protons in the molecule drawn at the top. The integration values, chemical shift and splitting patterns and coupling constants are displayed in the table. A reference of splitting pattern abbreviation can be found in Table 1.

The interpretation of this spectrum (Figure 64 follows closely the rationale used for Sn1TBoc as these molecule have the same number of hydrogens and in the positions. The major difference is that H_1 and H_2 can be distinguished: due to inductive effects promoted by the bromine atom, H_1 shifts downfield and is assigned the peak at 6.87 ppm. By exclusion, the second and last signal at 6.58 ppm in the aromatic region is determined to come from H_2. The remaining hydrogens follow the analysis described previously (see molecule 4py1TBoc), although in this spectrum the multiplet corresponding to H_4 is not as clear, likely due to some minor shimming issues.
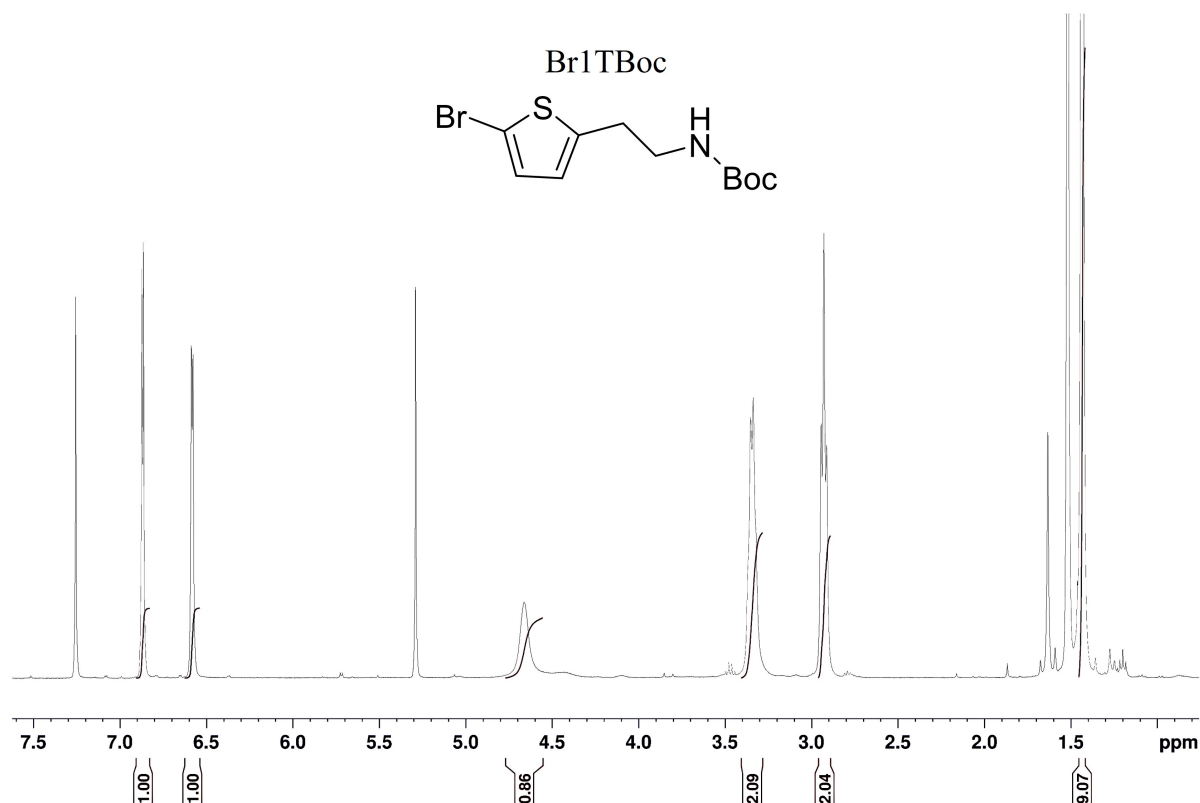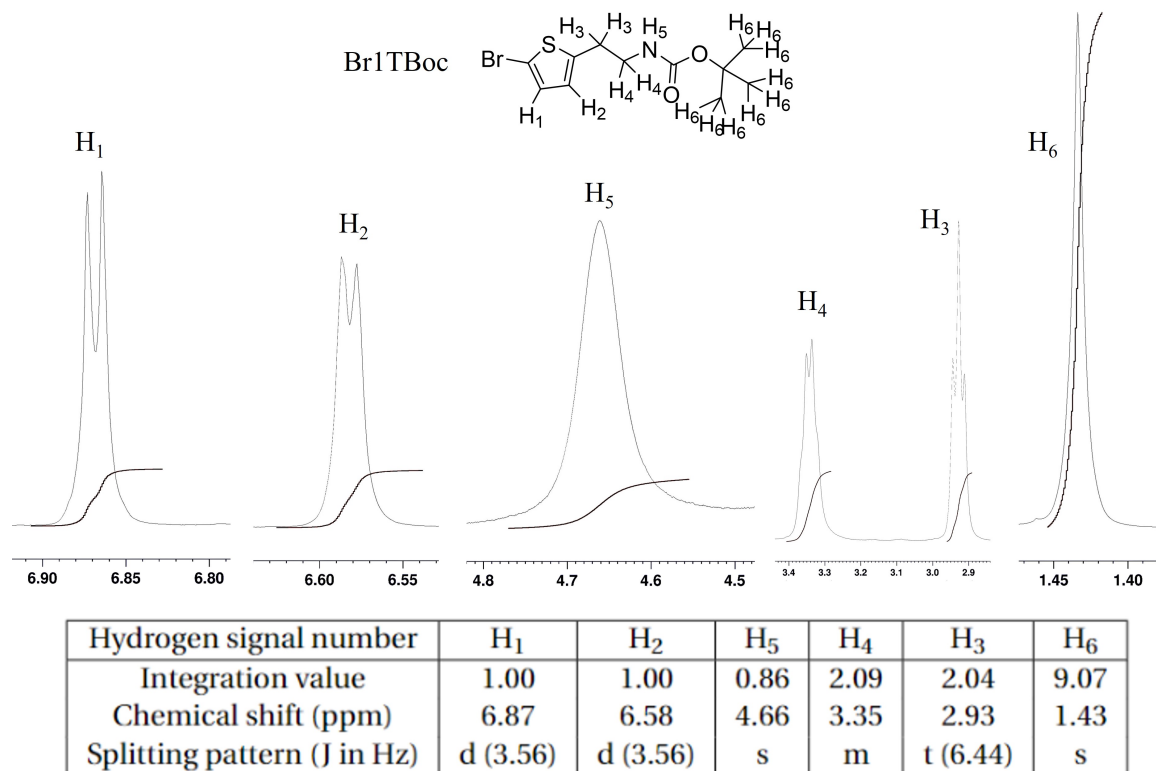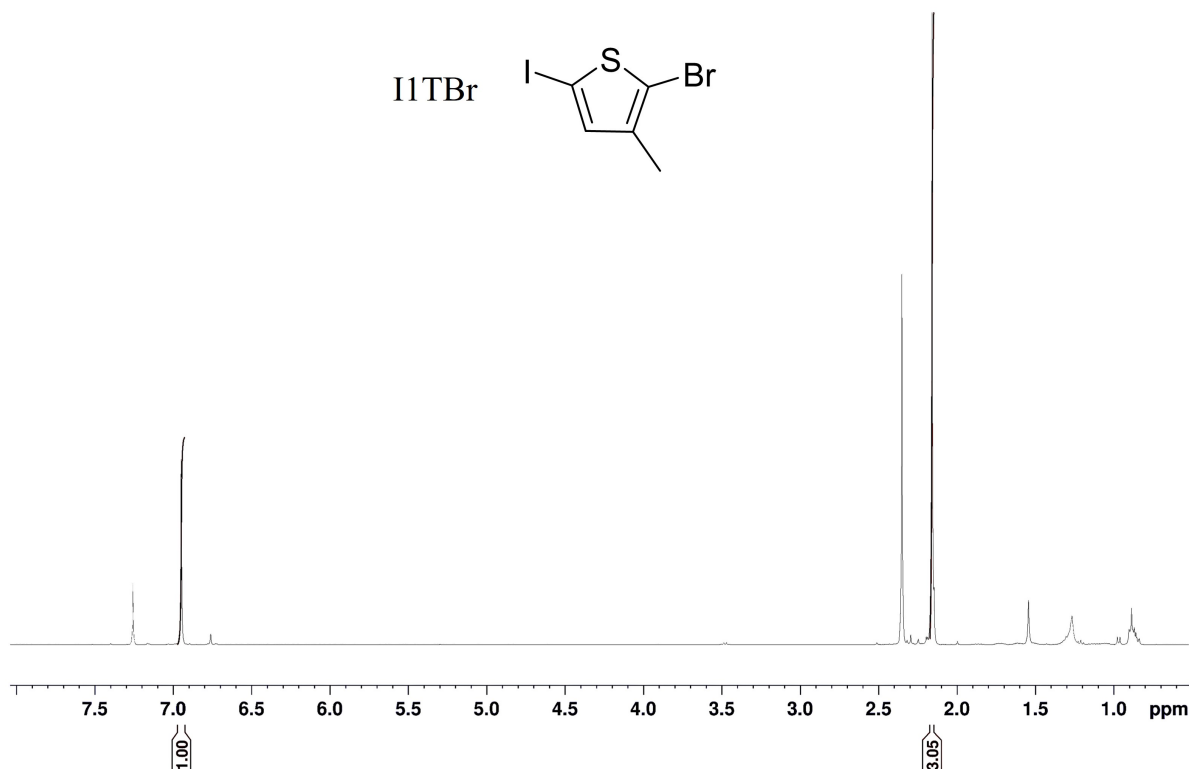
Figure 65: Full NMR spectrum for the molecule I1TBr. This is intended to show all peaks present in the scan, considering possible impurities, standards and solvent peaks (not integrated), which are addressed in the text.

The last intermediate thiophene ring to be analyzed is I1TBr, which is a highly desired molecule as it allows two sequential carbon-carbon coupling reactions (Suzuki and Stille) to take place. The full NMR spectrum of the compound is shown in Figure 65. In there, two unassigned peaks at 2.36 ppm and about 6.7 ppm (very tiny) can be found. Unfortunately, they correspond to leftover starting material, 1-bromo-2-methylthiophene, whose NMR, obtained from SciFinder, is printed in the Appendix section 6.1 for the reader's reference. Nonetheless, the remaining peaks indicate that the desired molecule was synthesized. The zoomed in NMR spectrum can be found in Figure 66.

Figure 66: Partial NMR spectrum for the molecule I1TBr. The peaks have been cropped out from the complete spectrum (displayed in Figure 65) and zoomed in to show the splitting patterns more clearly. The peaks retain their chemical shift order. The hydrogen labels correspond to respective protons in the molecule drawn at the top. The integration values, chemical shift and splitting patterns and coupling constants are displayed in the table. A reference of splitting pattern abbreviation can be found in Table 1.

In comparison to the previous molecules, I1TBr shows a much simpler NMR spectrum, as evidenced by the simple two singlets in Figure 66. H_1 is the only aromatic proton, with no hydrogen neighbors, thus coding for the signal at 6.95 ppm. H_2 corresponds to the methyl signal, also with no neighbors, which is much further upfield, matching the singlet at 2.16 ppm. The respective integration values also agree with the proposed structure. Therefore, even though some starting material is present in the sample, the desired molecule is confirmed by NMR.

3.1.3 3-ring ligand and relevant intermediates

For the synthesis of the 3-ring ligand 3py2TNH$_3$, the thiophene derivatives were used in coupling reactions, as shown in the synthetic scheme in Figure 34. And the products of these reaction are the synthetic intermediates, 3py1TBr and 3py2TBoc, whose NMR spectrum are described next. Lastly, the structure of the ligand 3py2TNH$_3$ is also addressed.
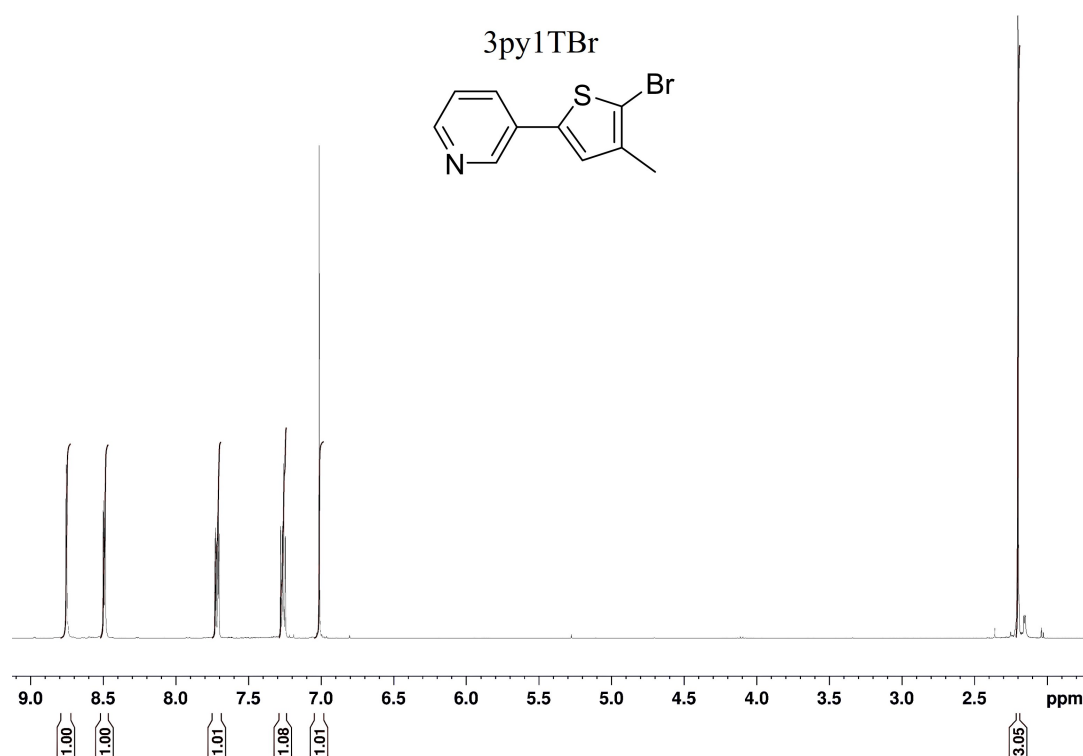
Figure 67: Full NMR spectrum for the molecule 3py1TBr. This is intended to show all peaks present in the scan, considering possible impurities, standards and solvent peaks (not integrated), which are addressed in the text.

The product of the first coupling (Suzuki reaction, in Figure 34) in the synthesis of the 3-ring ligand is the molecule 3py1TBr. Its full NMR displayed in Figure 67. The spectrum looks very clean, with little to no other residual solvent peaks. Note that the signal corresponding to deuterated chloroform is weak, since the sample was concentrated and is buried within the aromatic peaks of the material, although still visible when blown up. A detailed view of the peaks is provided in Figure 68.
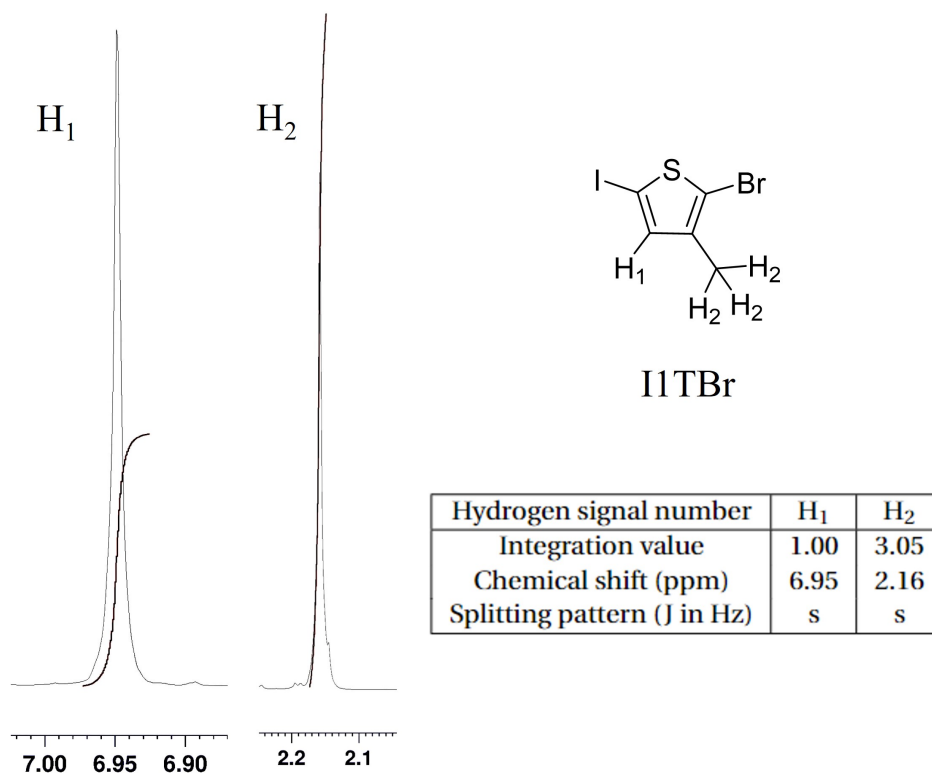
Figure 68: Partial NMR spectrum for the molecule 3py1TBr. The peaks have been cropped out from the complete spectrum (displayed in Figure 67) and zoomed in to show the splitting patterns more clearly. The peaks retain their chemical shift order. The hydrogen labels correspond to respective protons in the molecule drawn at the top. The integration values, chemical shift and splitting patterns and coupling constants are displayed in the table. A reference of splitting pattern abbreviation can be found in Table 1.
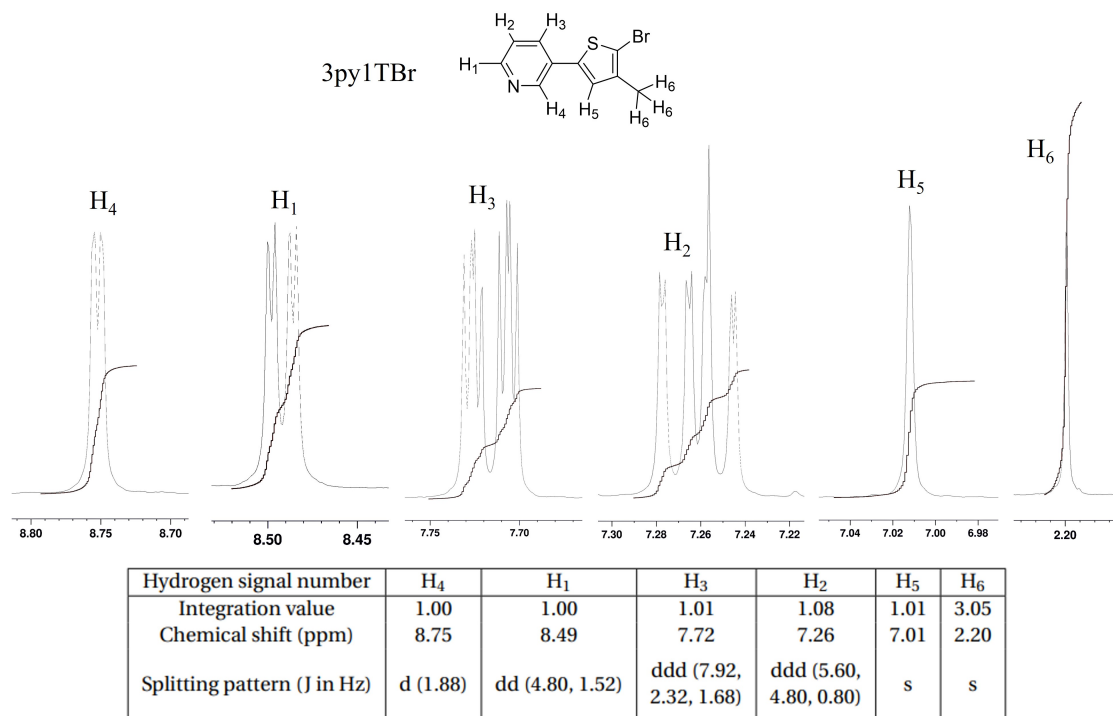
The protons whose signals appear most downfield in Figure 68 could belong either to H_4 or H_1, due to their closeness to the pyridine nitrogen. The decision to assign H_4 as the most downfield signal (8.75 ppm), while H_1 to the second-most downfield signal (8.49 ppm) is made taking into account the calculated splitting patterns. That is, H_1 is be split by its neighbors in *ortho* (H_2) and *meta* (H_3 and H_4) positions, considering long-range coupling, while H_4 is only split by its neighbors in *meta* (H_1 and H_3) and *para* (H_2) positions. This means that a more obvious splitting should appear in the signal coming from H_1, due to presence of stronger *ortho* coupling. This is observed in the second-most downfield signal (8.49 ppm) and consequently, this signal is interpreted to belong to proton one. In contrast, H_4 only displays weaker *meta* and *para* coupling partners, and the latter might not be even observed due to small J values. The peak that fits this splitting description is the one most downfield in the spectrum (at 8.75 ppm), and hence it is assigned to belong to proton 4.

To assign the remaining hydrogens in the pyridine ring, namely H_2 and H_3, the same rationale was followed; the only difference being that the hydrogens now compete for the third and fourth peaks in the spectrum. H_2 sits in between H_1 and H_3, indicating that it displays two strong *ortho* couplings and a small *para* splitting could also be observed due to the effect of H_4. In contrast, H_3 has only one neighbor in *ortho* position, H_2, while at the same time, H_1 and H_4 from their *meta* positions can create weaker, but still visible splittings. Given this scenario, H_3 is assigned the peak at 7.72 ppm, due to the presence of what is interpreted to be one larger *ortho* coupling (J value of 4.80 Hz), followed by two weaker *meta* couplings (J values of 2.32 and 1.68 Hz).

On the other hand, the peak assigned to H_2 at 7.26 ppm is also a doublet of doublet of doublets, but its overall shape looks much different. This is attributed to the fact that the two stronger *ortho* coupling patterns (J values of 5.60 and 4.80 Hz) create an initial doublet of doublets much more symmetrical compared to the peak in H_3, which has only one *ortho* coupling. Most excitingly, it is possible to see the weak *para* coupling of H_4 to H_2 (J value of 1.68 ppm) in the final splitting of the peaks around 7.26 ppm, creating the last small doublet in the ddd pattern. Note that the reason for one of the peaks within the signal for H_2 to be taller is the residual solvent peak of deuterated chloroform, which is used to run the NMR sample. Thus, it does not reflect the presence of another hydrogen in the molecule.

The last two hydrogens in the molecule, H_5 and H_6 are more easily assigned. H_5 is still an aromatic proton, but should appear more upfield compared to the previous hydrogens, since it does not belong in the pyridine ring. Additionally, it has no direct neighbors to produce a significant splitting pattern. Therefore, its signals is matched to singlet at 7.01 ppm. H_6 should also be a singlet, but come much further upfield, since it is not aromatic. Therefore, it is assigned the peak that integrates for 3 hydrogens at 2.20 ppm.

Nonetheless, one small detail should be mentioned. The reaction that produced this molecule hinged on the idea that Suzuki couplings seem to be more selective toward reacting with organoiodines ([70]). Therefore, the expectation is that only the bigger

halogen was used. By ^{1}H NMR only, one cannot fully determine whether this is the case or if the sample is a mixture of the desired molecule and a different product which has iodine handle (this would be produced if the bromine reacted instead). While it is true that the position of H$_5$ and H$_6$ would be "swapped", the difference in the chemical shift could be too small to detect (they would still be both singlets). Other techniques, such as ^{13}C or Liquid-Chromatography Mass-Spectrometry (LC-MS) or even 2D NMR could be used to determine which halogen or mix is present. Nonetheless, as long as one of handles were still available (and it is because there is no other hydrogen signal), the next coupling reaction can proceed.
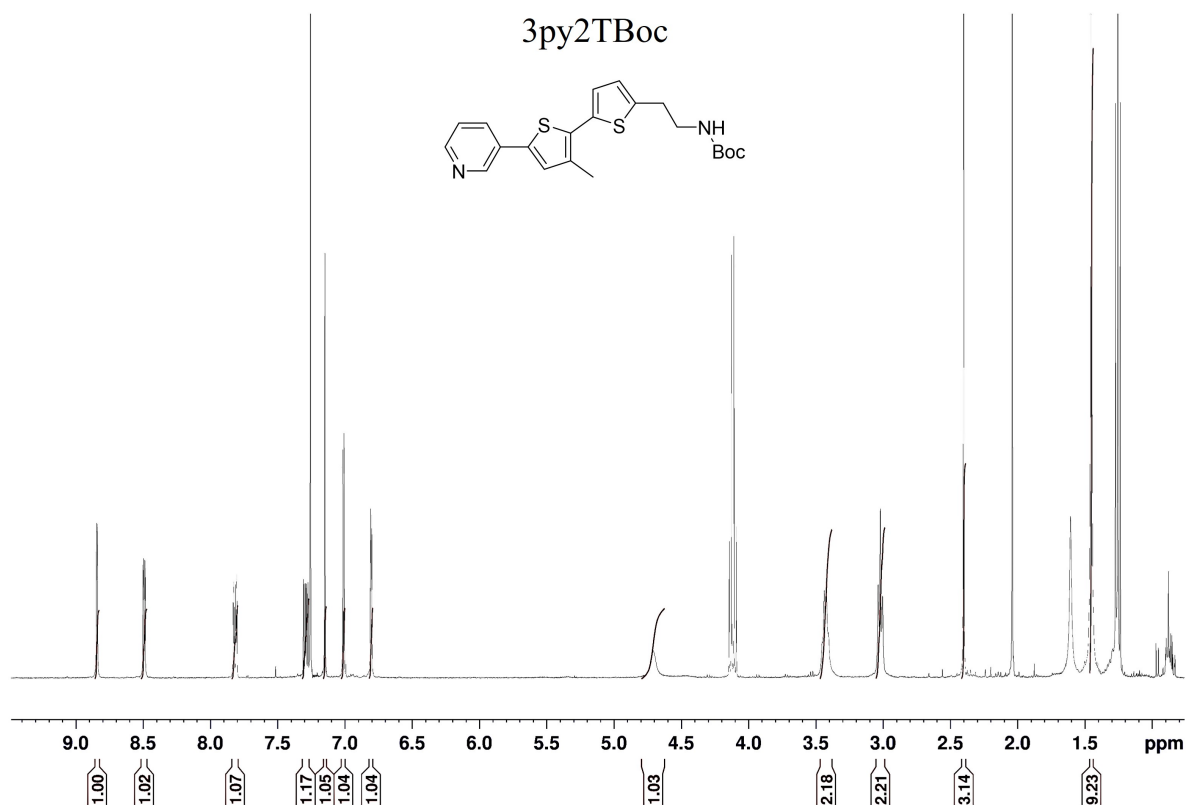
Figure 69: Full NMR spectrum for the molecule 3py2TBoc. This is intended to show all peaks present in the scan, considering possible impurities, standards and solvent peaks (not integrated), which are addressed in the text.

The next step was then to react 3py1TBr with Sn1TBoc in the Stille coupling to synthesize the BOC protected version of the desired 3-ring ligand, 3py2TBoc. The full NMR spectrum of this advanced intermediate is shown in Figure 69. Four peaks in this spectrum are not integrated and they correspond to residual solvent peaks: water is present at around 1.5 ppm and the three peaks of ethyl acetate are visible at 4.12 ppm, 2.05 ppm ad 1.26 ppm [83]. The zoomed in peaks are detailed in Figure 70.

The logic for assigning these protons is a combination of what has been done for the previous molecules. With respect to the aromatic protons in the pyridine ring, the order of peaks follows the assignment established for the molecule 3py1TBr. Thus, the first two signals at 8.84 and 8.49 ppm correspond to H_4 and H_1 respectively, due to their proximity to the nitrogen atom and their differences in splitting pattern. Next, protons H_3 and H_2 follow in sequence, for the same reasons detailed above. H_5 comes as singlet at 7.15 ppm,

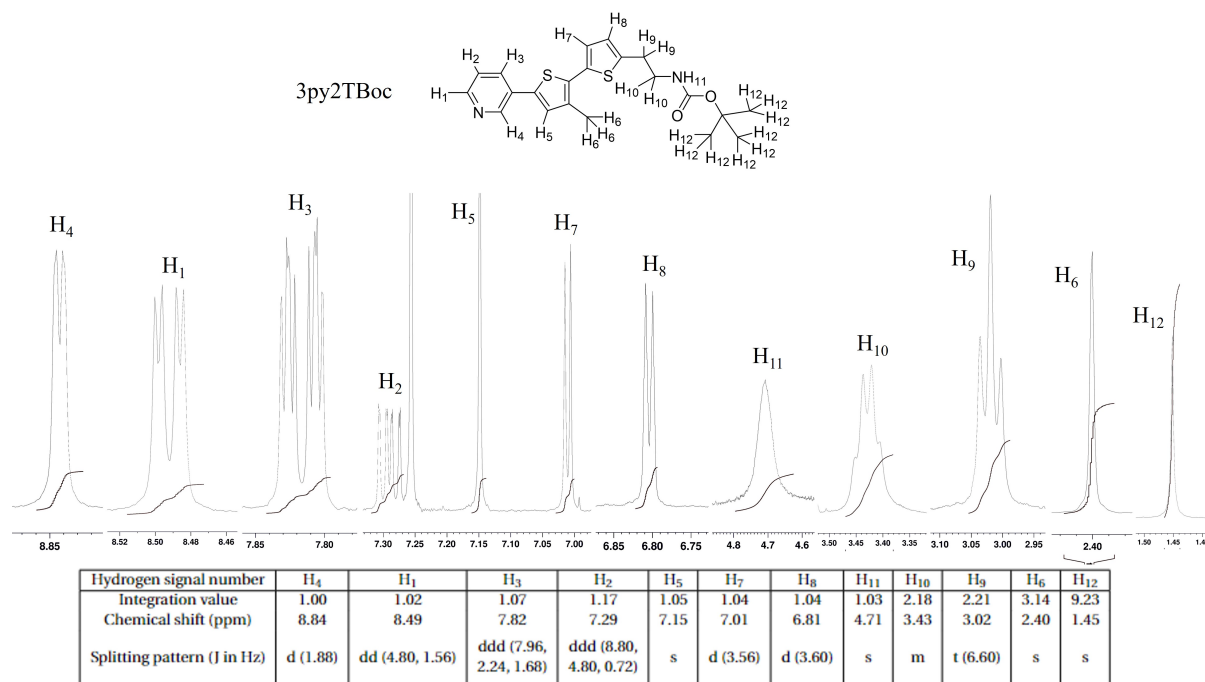| Hydrogen signal number	H$_4$	H$_1$	H$_3$	H$_2$	H$_5$	H$_7$	H$_8$	H$_{11}$	H$_{10}$	H$_9$	H$_6$	H$_{12}$
Integration value	1.00	1.02	1.07	1.17	1.05	1.04	1.04	1.03	2.18	2.21	3.14	9.23
Chemical shift (ppm)	8.84	8.49	7.82	7.29	7.15	7.01	6.81	4.71	3.43	3.02	2.40	1.45
Splitting pattern (J in Hz)	d (1.88)	dd (4.80, 1.56)	ddd (7.96, 2.24, 1.68)	ddd (8.80, 4.80, 0.72)	s	d (3.56)	d (3.60)	s	m	t (6.60)	s	s

Figure 70: Partial NMR spectrum for the molecule 3py2TBoc. The peaks have been cropped out from the complete spectrum (displayed in Figure 69) and zoomed in to show the splitting patterns more clearly. The peaks retain their chemical shift order. The hydrogen labels correspond to respective protons in the molecule drawn at the top. The integration values, chemical shift and splitting patterns and coupling constants are displayed in the table. A reference of splitting pattern abbreviation can be found in Table 1.

which is expected, since it is still bonded to the first thiophene ring but does have any neighboring protons.

The most significant change in the aromatic part of the spectrum compared to the previous intermediate is the presence of H$_7$ and H$_8$. They belong to the second thiophene ring just added in the coupling reaction. The signals corresponding to these protons are the most upfield within the aromatic region and match to doublets at 7.01 and 6.81 ppm. This assignment is reasonable when considering that they are far away from any other electron-withdrawing groups (either BOC or pyridine), and split each other through the same coupling constant, thus creating equivalent doublets. However, following the argument established in for the molecule 4py1TBoc, a more in depth analysis would be required in order to determine with certainty which of the signals correspond to H$_7$ or H$_8$. Therefore, the assignment of protons 7 and 8 displayed in Figure 70 is tentative. Nonetheless, both signals integrate for the correct number of hydrogens, leading to the

conclusion that the aromatic protons, in their entirety, are all present and in the correct location.

The hydrogens in the mid- and upfield part of the spectrum fit the description outlined for the molecule 4py1TBoc, with an adjustment of the overall hydrogen index number. H_{11} is the proton in the nitrogen of the carbamate group and matches the peak at 4.71 ppm, as a broad singlet. The alkyl hydrogens H_9 and H_{10} follow a triplet and multiplet pattern, respectively, the latter being shift downfield relative to the former due to its proximity to the carbamate. Finally, H_{12} corresponds to the *tert*-butyl group after the carbamate and is the most upfield signal, integrating for the correct number of hydrogens.

Considering the proton assignment above, it is fair to conclude that the desired advanced intermediate, 3py2TBoc, is correctly synthesized.

The last step of the synthesis plan is to deprotect the previous molecule, 3py2TBoc, and create the desired iodide salt. The full NMR spectrum of the 3py2TNH$_3$ ligand is shown in Figure 71. The signals that have not been integrated correspond to diethyl ether, at around 1 and 3.4 ppm [83] and water. Usually, the water signal is expected to appear at 3.33 ppm in deuterated DMSO, but in this spectrum it is believed that it appears at about 4 ppm. The reason for such drastic downfield shift is hypothesized to be the presence of leftover hydroiodic acid from the deprotection. The individual peaks corresponding to the molecule are displayed in detail in Figure 72.
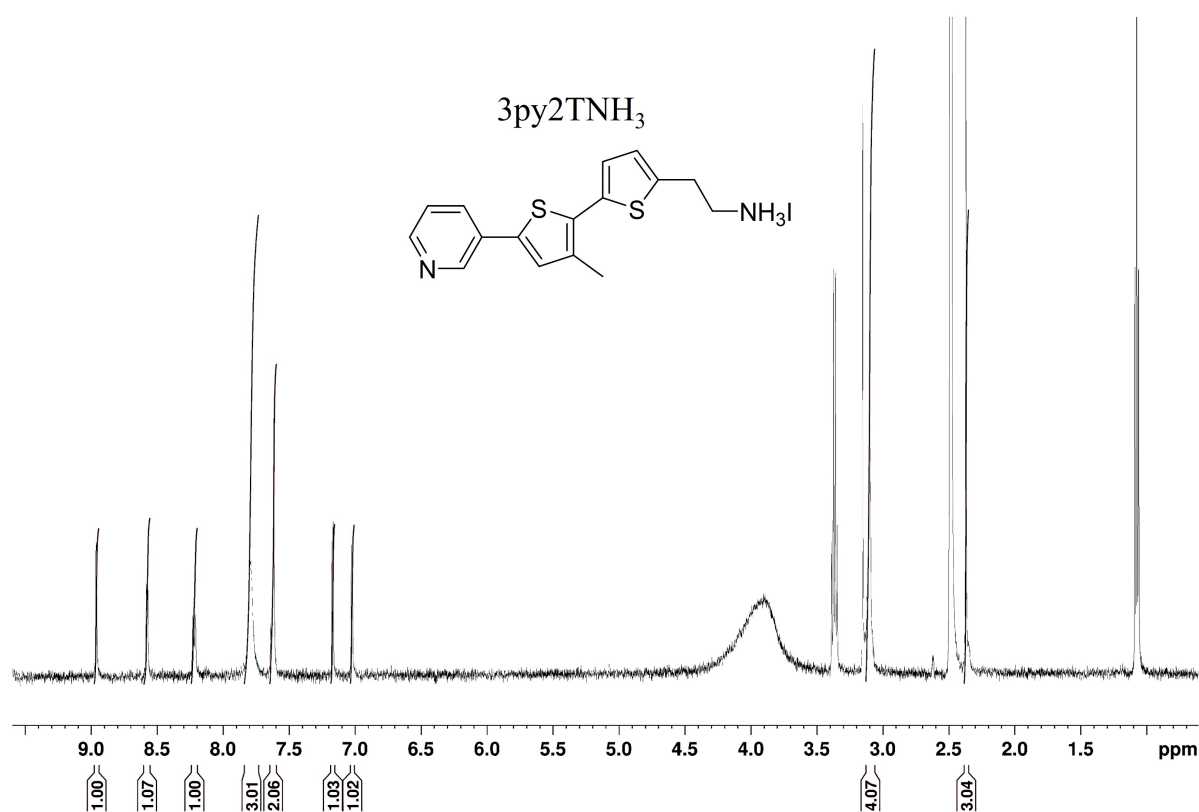

Figure 71: Full NMR spectrum for the molecule 3py2TNH$_3$. This is intended to show all peaks present in the scan, considering possible impurities, standards and solvent peaks (not integrated), which are addressed in the text.
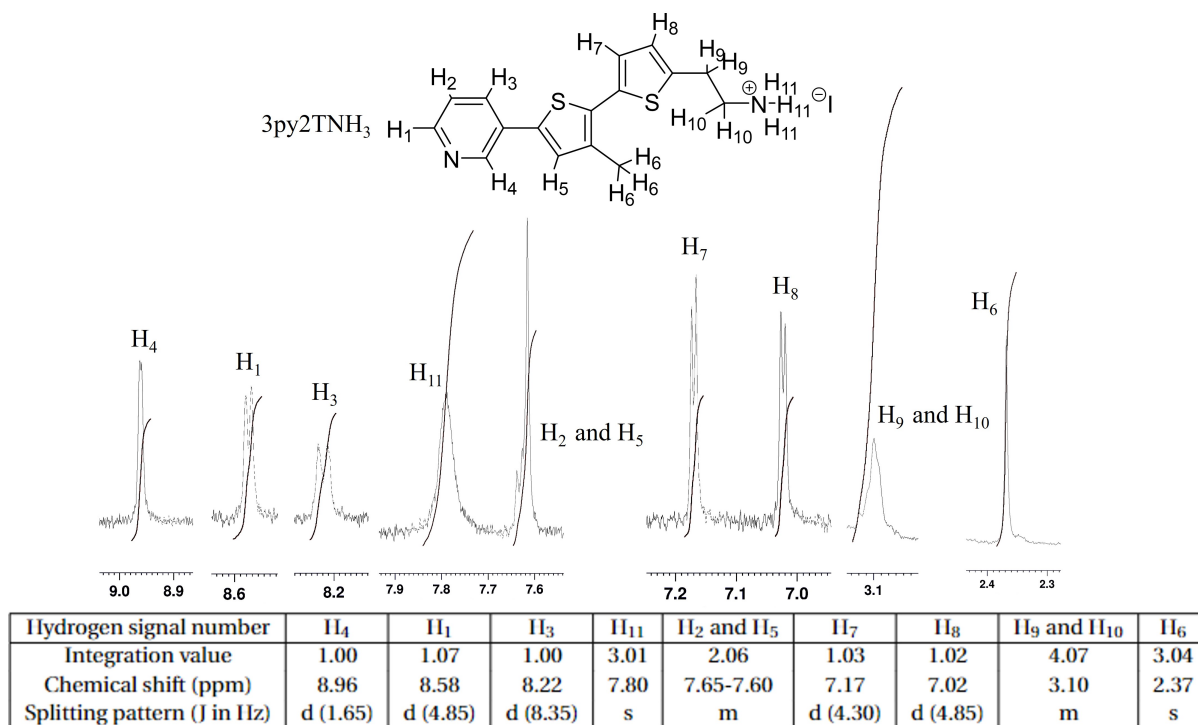
Figure 72: Partial NMR spectrum for the molecule 3py2TNH$_3$. The peaks have been cropped out from the complete spectrum (displayed in Figure 71) and zoomed in to show the splitting patterns more clearly. The peaks retain their chemical shift order. The hydrogen labels correspond to respective protons in the molecule drawn at the top. The integration values, chemical shift and splitting patterns and coupling constants are displayed in the table. A reference of splitting pattern abbreviation can be found in Table 1.

Unfortunately, the NMR sample for this spectrum was not as concentrated as previous ones, so the peaks became smaller, closer to the baseline and overall less defined. Nonetheless, it is possible to analyze it. Naturally, the peak assignment closely resembles that of 3py2TBoc. Thus, the first three signals indicated in Figure 72 correspond to H$_4$ (8.96 ppm), H$_1$ (8.58 ppm) and H$_3$ (8.22 ppm). Notice that this assignment has been directly transferred from the previous intermediate, since the splitting patterns are not visible, and therefore, it is only tentative. While that is true, no significant change has been performed in the aromatic side of the molecule; so it is reasonable to assume that, if the reaction happened as predicted, then these protons stayed the same.

The hydrogen that undergoes the biggest change in the reaction and in the spectrum is H$_{11}$, since its signal shifts significantly downfield, appearing at 7.80 ppm and acquired a new integration value of three, due to the protonation of the nitrogen atom. This effect is rationalized by placement of a positive charge in the nitrogen, leading to an increase of its

electronegativity and a stronger electron withdrawal effect on these protons, as observed before with 4py1TNH$_3$.

The next two aromatic peaks more easily determined are those belonging to H$_7$ and H$_8$ because they have specific characteristics: they appear as two doublets most upfield within the aromatic region (considering the trend established by the intermediate 3py2TBoc) and within a small chemical shift range, since both hydrogens experience fairly similar magnetic environments. The two peaks with those features appear at 7.17 and 7.02 ppm and they are respectively assigned to H$_7$ and H$_8$. Note that for the same reasons described for the molecule 3py2TBoc, this assignment is tentative.

Thus, this leaves only one peak to be assigned within the aromatic region, namely the multiplet spanning 7.65 - 7.60 ppm. By exclusion, the signal is interpreted to be an overlap between the peaks from H$_2$ and H$_5$, considering that these two hydrogens yielded signals in between H$_3$ and H$_7$ in the previous intermediate (see Figure 70). The signal shape is also not symmetrical, which might support this explanation (there is a hidden overlap that cannot be distinguished). However, the exact reason for the chemical shifts to have changed in such a way to lead to an overlap remains unknown. Nonetheless, the multiplet integrates for 2 hydrogens, and protons 2 and 5 are the only ones missing in the aromatic region; so this peak is tentatively assigned to belong H$_2$ and H$_5$.

In the upfield region of the spectrum, the four alkyl protons, H$_9$ and H$_{10}$, are combined into the multiplet showing at 3.10 ppm. Note that this effect is consistent with what was observed in the previous spectrum of the salt 4py1TNH$_3$. That is, in both cases the alkyl hydrogens, in the salt, have yielded only one signal. Lastly, the hydrogens from methyl substituent in the middle thiophene, H$_6$, are observed at 2.37 ppm. The singlet splitting pattern and integration are consistent with the proposed structure.

While some of the signals in this NMR spectrum might lead to further questions, the overall number of hydrogens and their relative chemical shifts indicate that all functional groups and substituents are present and that the desired protonation took place. Therefore, the 3-ring ligand, 3py2TNH$_3$ is deemed successfully synthesized.

This brings an end to the NMR and Chemistry-related discussion. The next task is to use the ligands, whose structures are confirmed, to make novel 2D-perovskites. The following sections are devoted to describe how these novel hybrid materials are characterized and to show the metrics that describe how well the solar cells made with them are performing.
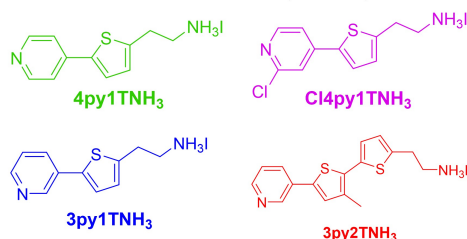
3.2 Characterizing novel 2D-perovskites in thin films

After structural confirmation, the novel pyridine-based ligands were spun-coated into thin films in the presence of lead iodide. Note that **these data were collected by Jiaonan Sun (from the Department of Chemical Engineering at Purdue University)** and are reproduced with authorization, in order to give the reader a sense of how the synthesis of the ligands is combined with the material investigations. The data are also analyzed to so that the all the information given in the Introduction can be placed into context.

These films, as shown in next few sections, show indication of 2D perovskite formation. Therefore, it is time to move on to step 2 of the data analysis and characterize these materials.
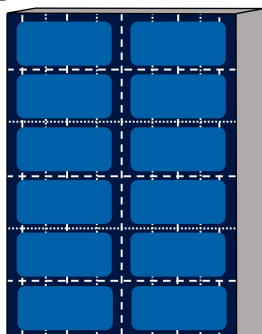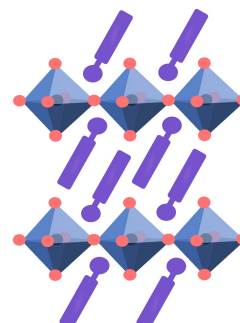
Data analysis

Figure 73: Data analysis - Step 2: Characterizing novel 2D-perovskites in thin films.

3.2.1 UV-Vis spectroscopy

UV-Vis spectroscopy is used to obtain the absorption wavelength pattern of the thin films produced with the novel ligands. As shown in Figure 74, all ligands show a peak absorption within the range of 500 to 545 nm.
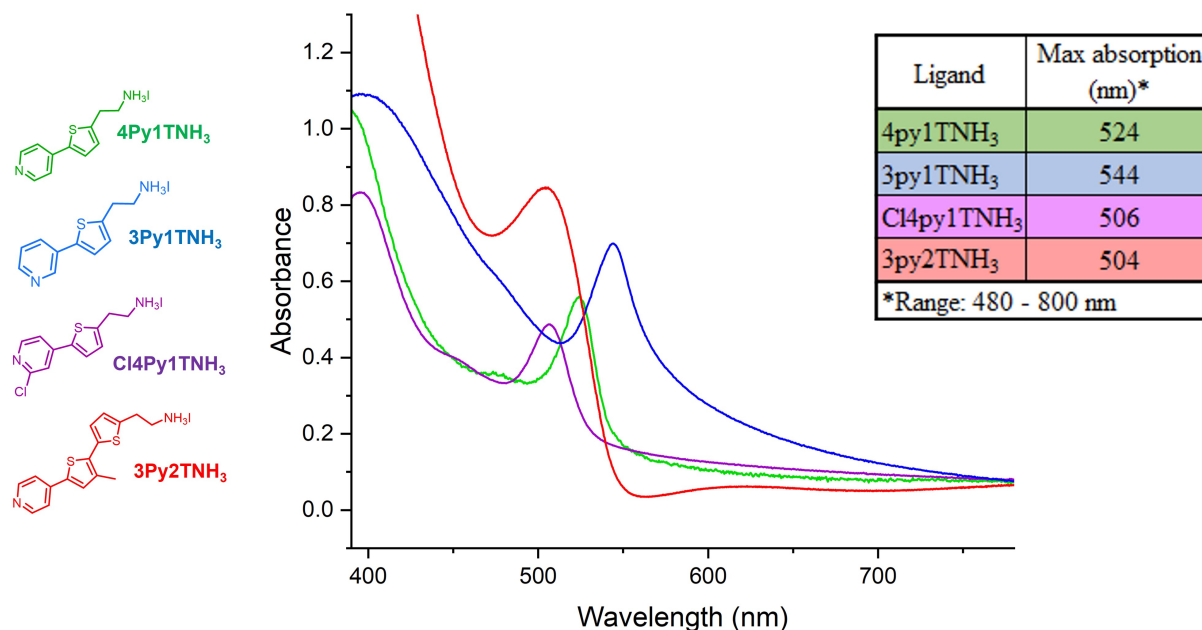

Figure 74: UV-Vis spectra of perovskite thin films for all ligands. The presence of absorption peaks is indicative that the novel ligands synthesized in this study are capable of forming desired 2D-perovskites. In addition, the maximum absorption wavelength is closely related to energy of the semiconductor band gap, although it is not a direct comparison [85].

The very presence of these absorption peaks is indicative that the novel ligands are capable of forming 2D-perovskites, when allowed to anneal with the lead iodide in the thin films! Therefore, new 2D-pervoskites that encompass thiophene and pyridine-based ligands are assembled! This is consistent with the empirical observation that upon fabrication, the thin films turned orange (an indicative of perovskite formation). Moreover, these absorbances lie within the characteristic wavelength range for n=1 2D-perovskites, since no red shift is observed (this would indicate that possible n=2 or n=3 materials were formed). Therefore, true 2D materials are synthesized.

But the most imporant point of obtaining an UV-Vis spectrum is to detect the maximum absorption wavelength, since it carries an energy that can be used to approximate

the band gap energy of the perovskite semiconductor. It is not a one to one match, as described by Makula and colleagues [85], but it is possible, after some adjustments (that are beyond the scope of this study), to extract the band gap energies of these new materials!

This should sound quite amazing, especially considering that in the Introduction, the whole concept of perovskites having semiconducting band structures was derived from the atomic orbitals. That is, the absorbances shown in Figure 74 indicate that the electronic bands, which might have sounded like an extremely theoretical concept, can be quite neatly observed in practical measurements.

Note that a small optimization was necessary for the $3py2TNH_3$. Only when the thin films are coated with a higher concentration of the ligand the 2D-perovskite absorbance peak at 504 nm is visible. Otherwise, the peak becomes hidden in the rise of the absorbance produced by the ligand itself.

One of the main goals of this research is to use the novel pyridine-based ligands to trigger new 2D-perovskite formation. According to the UV-Vis spectra obtained in Figure 74, all thin films display a peak at the desired range and therefore, contribute to the interpretation that the novel ligands synthesized in this study, namely $Cl4py1TNH_3$, $4py1TNH_3$, $3py1TNH_3$ and $3py2TNH_3$ are capable of fulfilling that goal.

3.2.2 Photoluminescence

In addition to the UV-Vis absorbance measurements, which allows the investigation of the band gap energy of 2D perovskites, a very useful piece of characterization comes with emission spectroscopy, one of them being photoluminescence (PL). The PL spectra for the thin films fabricated with all four novel ligands were recorded and they are shown in Figure 75
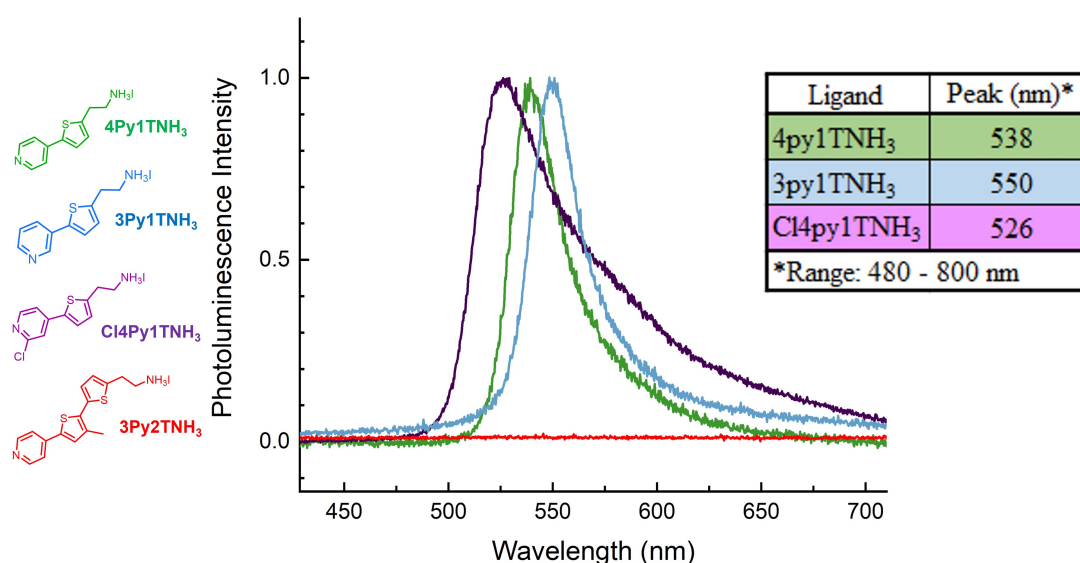

Figure 75: Pholuminescence spectra of thin films with all four ligands synthesized in this study. The table displayed next to the spectrum shows the wavelength in which the photoluminescence intensity is at a maximum for each thin film - ligand combination, at the exception of 3py2TNH$_3$, which did not show any results different than baseline.

Before analyzing the data, it is very imporant to remind the reader of the quantum wells structure that was developed in section 1.4.2. That is, for type I energy alignments (Figure 21), the formation of carriers takes place in the ligand orbitals; but due to the specific energy mismatch in that the LUMO of the ligand is higher in energy compared to the conduction band of the perovskite (while the opposite is true for the HOMO-VB mismatch), the carriers migrate to the perovskite bands and hence recombine in the inorganic material. Upon that process, a photon of light is emitted. For ligands 4py1TNH$_3$, 3py1TNH$_3$ and Cl4py1TNH$_3$, there *is* a photoluminescence maximum intensity which indicates that not only that recombination is happening and that the carriers are moving

through the bands of the different materials, but also that the energy alignment between the novel ligands and perovskite is of type I!

Conversely, for type II energy alignments (Figure 22), it was said that the holes formed in the HOMO of the ligand do not transfer to the perovskite valence band because they become stuck in the quantum well, while the electrons migrate to the conduction band as they become more stabilized in the process. This causes the carries to be present in the bands of different materials, which prevents their recombination. Therefore, there should not be a photon that can be observed in emission spectroscopy. This is exactly what is observed in the spectrum of ligand 3py2TNH$_3$, such that, the quenched photoluminescence spectra of the 3-ring ligand indicates that its energy alignment with the perovskite is of type II.

Note that this pattern is consistent with the increased conjugation of the 3-ring ligand. Recall that, by using the analogy of Frost circles (Figure 28), it is easy to see that the increased conjugation of a given aromatic molecule leads to the shortening of its HOMO-LUMO gap. When this idea is applied in the case of the ligand 3py2TNH$_3$ and its type II quantum well energy alignment, it is hypothesized that its HOMO-LUMO gap shrunk causing the HOMO to be above the perovskite valence band, creating the energy mismatch observed. Conversely, then the LUMO should have become lower in energy as well, which might have happened. However, this led to no overwhelmingly different energy mismatch between the LUMO and the perovskite conduction band, still supporting the type II arrangement.

Still on the characterization of the material's band structure, another detail should be mentioned: there is redshift between the absorbance and emission wavelengths (see the legends in Figures 74 and 75): 14 nm, 6 nm, and 20 nm for the ligands 4py1TNH$_3$, 3py1TNH$_3$ and Cl4py1TNH$_3$, respectively. This is known as the Stokes shift and it is very common when comparing absorption and emission spectra [86]. In semiconductor materials, these shifts can help characterize and fine tune the very edges of the valence and conduction bands. And this is imporant because the relative energy of the bands will

heavily influence the semiconductor properties, such as excitation and carrier generation processes, (as was highlighted in section 1.2.3) and, of course, modulate the bang gap energy.

These spectroscopy techniques serve well when trying to electronically characterize the new hybrid materials. However, the physical structure of the perovskite can also be investigated, which is detailed in the next section.

3.2.3 X-ray diffraction

Understanding the physical structure of the perovskite through crystallography is also a very active area of research [23, 24, 59] and for that, X-ray diffractometers are routinely used. A pictogram of this instrument is given in Figure 76 and small description of how it works is given in the caption.
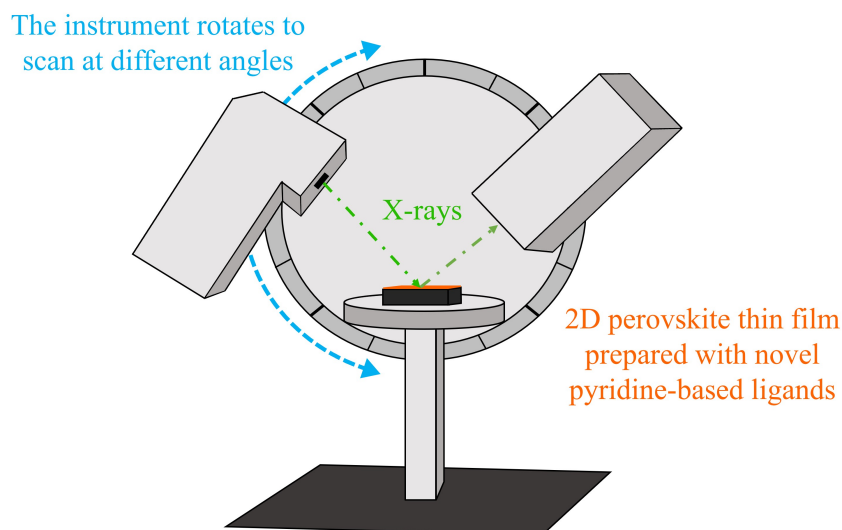

Figure 76: X-ray diffractometer pictogram. An X-ray diffractometer sends very high energy photons (in the X-ray range) to a given solid lattice (a new 2D-perovskite, for instance). And it does so in several different angles. However, the X-rays will bounce back after interacting with the lattice, generating the diffraction pattern. The angles in which peaks are generated are very particular, since the scattered X-rays must have interacted constructively with each other when leaving the solid lattice. Since the angles in which these X-rays were sent are recorded, one can calculate the spacing of the lattice using the Bragg's diffraction law [18].

So far, only one ligand, Cl4py1TNH$_3$ has been analyzed through X-ray diffraction and the pattern obtained is shown in Figure 77. As observed in Panel A, the peaks appear in the spectrum at regular intervals. This indicates that the solid under analysis has a consistency in its structure, given by the unit cell (section 11), which signals a lattice formation. This lattice is attributed to the formation of a novel hybrid perovskite, which is assembled with the ligand Cl4py1TNH$_3$. Panel B works as a control and shows that when only the ligand is spun-coated into the film, a small residual peak is observed, which quickly stops yielding any diffraction signal. Therefore, it helps assign the very first peak present in Panel A and conversely, to determine that more prominent diffraction pattern

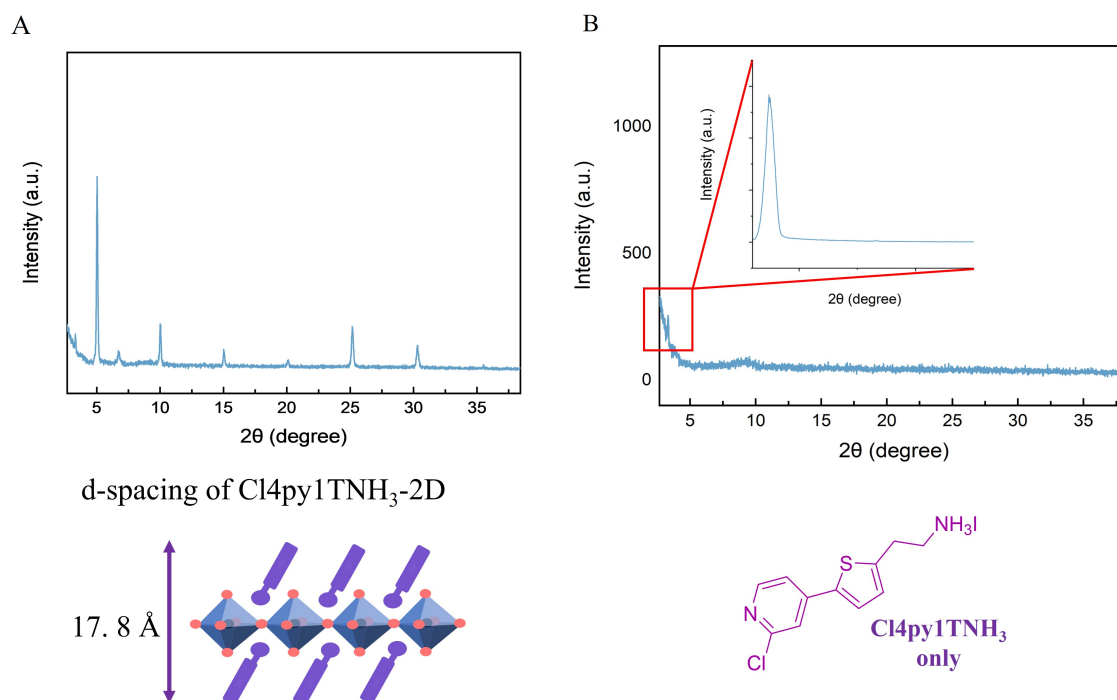observe does not arise from any ligand-only crystallization process.

Figure 77: X-ray diffraction pattern for 2D perovskite with ligand Cl4py1TNH$_3$. Panel A shows the 2D-perovskite diffraction pattern. Panel B shows the same scan performed with only the ligand spun-coated on the film.

Lastly, using the diffraction angles obtained in Panel A, the lattice spacing, d, can be calculated using the Bragg's diffraction law ($2dsin\theta = n\lambda$)[18]. The size of the novel 2D perovskite formed in the presence of Cl4py1TNH$_3$ is of 17.8 $\mathring{A}$. The 2D-perovskites employing the other ligands are still under analysis.

This brings an end to thin film characterization data. Therefore, it is time to move on to the solar cell efficiency parameters.

3.3 Solar cell devices

This section is devoted to show the solar cell electronic parameters that help evaluate the efficiency and practical use of the new semiconductor materials assembled in this study.

Data analysis

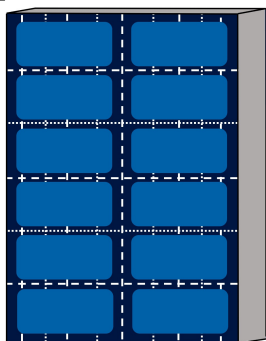1. Confirming **structure of ligands** and intermediates (**NMR**)
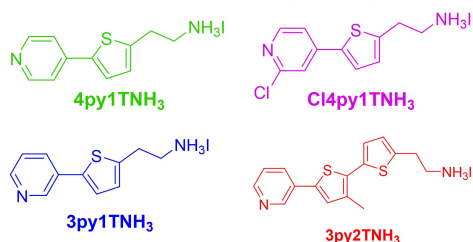
2. **Characterizing** novel 2D-perovskites **thin films** via:

a. UV-Vis analysis

b. XRD analysis

c. Photoluminescence analysis

3. Comparing **electronic parameters** of **perovskite solar cells**

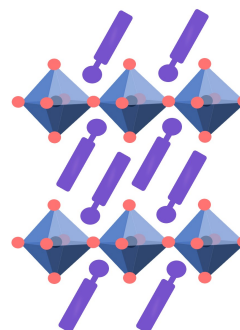4. Confirming **2D perovskite** structure in **single crystals**

Figure 78: Data analysis - Step 3: Comparing electronic parameters of PSCs.

In addition to the thin films, solar cell devices were prepared. They are characterized in terms of their power conversion efficiencies (PCEs), fill factors (FFs), open-circuit voltage (V_{OC}) and short circuit current (J_{SC}), which are parameters extracted from the J-V curves, as highlighted in Methods section 2.5.
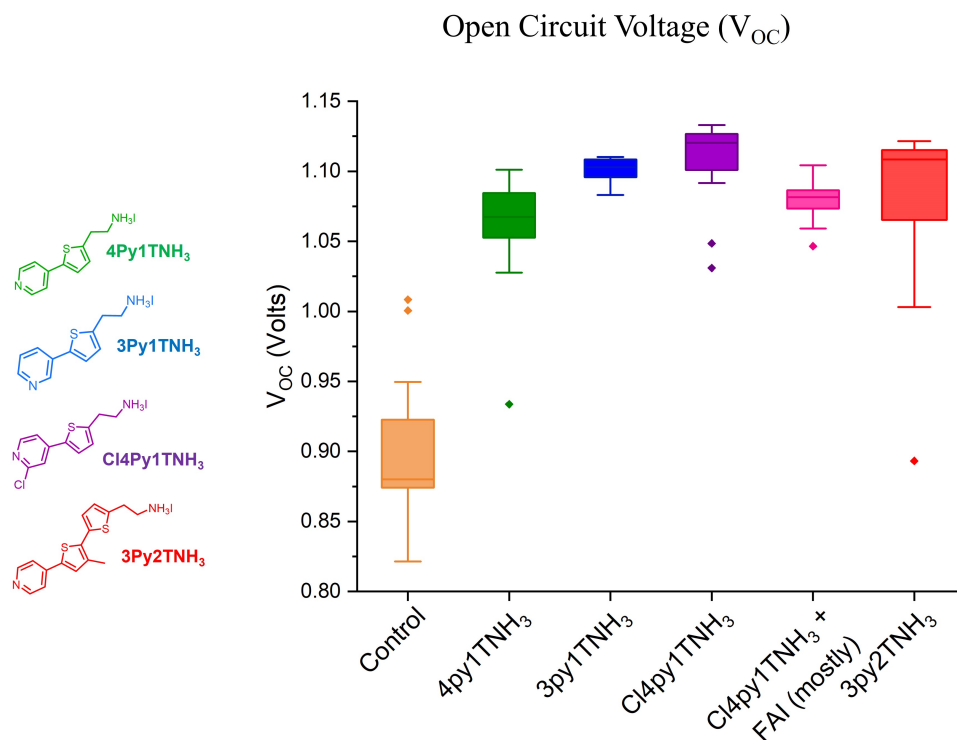

Figure 79: Solar cell devices performance - Open Circuit voltage. The entry in pink refers to a set of PSCs that have been prepared with the Cl4py1TNH$_3$ ligand and FA cations, which might have lead to the formation of quasi-2D perovskites.

The acquired V_{OC}'s, J_{SC}'s, FFs and PCEs are shown in Figures 79, 80, 81 and 82 respectively. These measurements are placed in this study to give the reader a sense of the performance of the devices and to show how the synthesis developed in this study fits into the larger picture of perovskite solar cell characterization. But a detailed discussion about these parameters is set aside since these data were collected by Jiaonan Sun.

However, it is still important to highlight a couple of features of these solar cells, especially concerning their power conversion efficiency.

Figure 80: Solar cell devices performance - Short Current density. The entry in pink refers to a set of PSCs that have been prepared with the Cl4py1TNH$_3$ ligand and FA cations, which might have lead to the formation of quasi-2D perovskites.

Figure 81: Solar cell devices performance - Fill Factor. The entries in pink refers to a set of PSCs that have been prepared with the Cl4py1TNH$_3$ ligand and FA cations, which might have lead to the formation of quasi-2D perovskites.
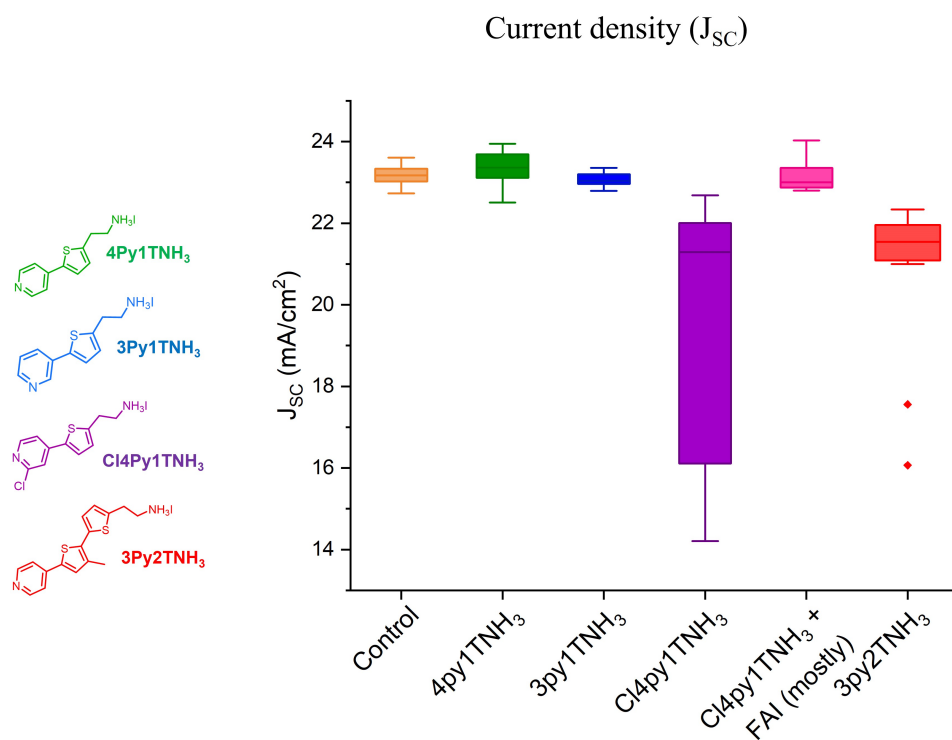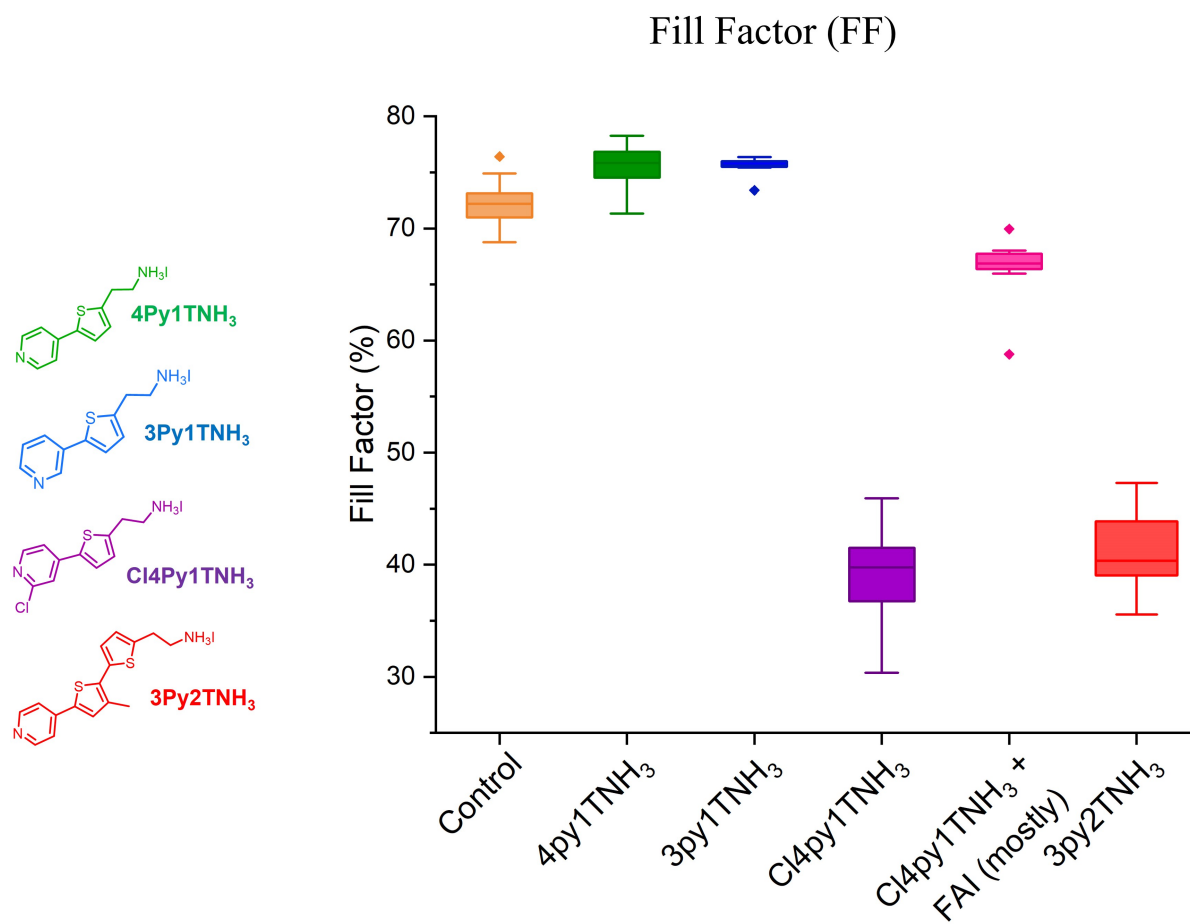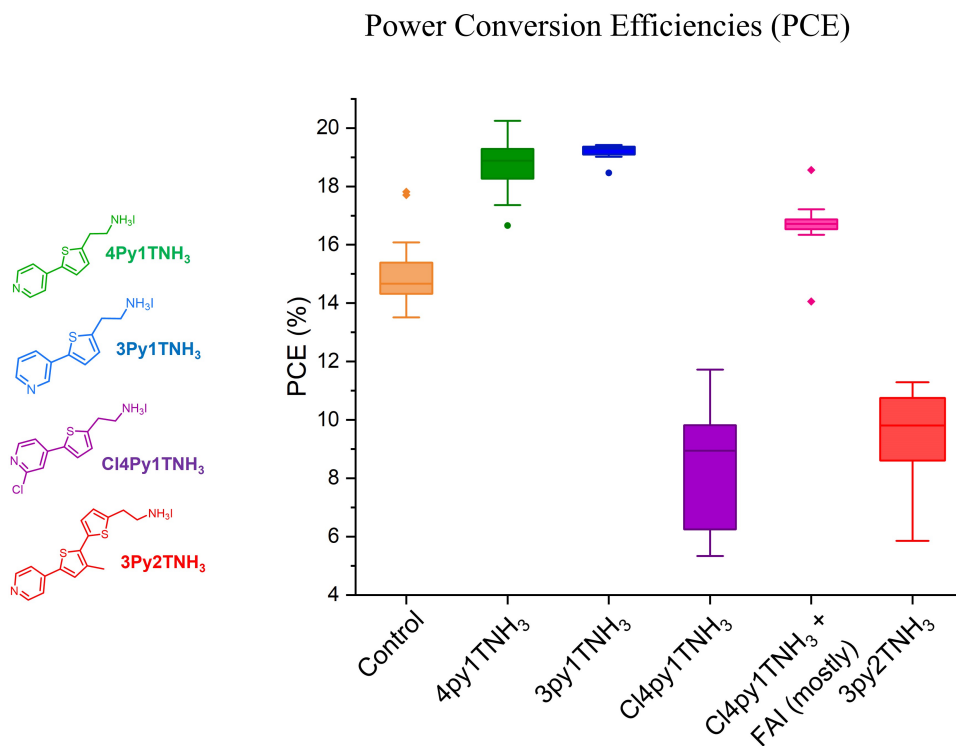
Power Conversion Efficiencies (PCE)

Figure 82: Solar cell devices performance - Power Conversion Efficiency. The entry in pink refers to a set of PSCs that have been prepared with the Cl4py1TNH$_3$ ligand and FA cations, which might have lead to the formation of quasi-2D perovskites.

As shown in Figure 82, the PSCs containing type I 2D-perovskite assembled with ligands 4py1TNH$_3$ and 3py1TNH$_3$ perform better than the control. This is attributed to the greater efficiency of the novel pyridine-based ligands developed in this study. In contrast, the efficiency of the cells employing the ligand Cl4py1TNH$_3$ is much lower. A possible explanation for such drastic decrease is the presence of leftover hydroiodic acid in the ligand sample, as given by the downfield shift of the water peak in the NMR spectrum of the ligand (Appendix section Figure 85). The acid, when in contact with the other layers in the solar cell, could lead to a faster degradation of the devices rendering them less efficient. But note that when this ligand is spun coated into a perovskite in the presence of smaller cations (likely forming quasi-2D perovskites in the process), the efficiency is rescued. In this situation, the leftover acid could more favorably interact with the smaller cations, avoiding its dispersion and degradation of the remaining layers. Therefore, the lower efficiency of PSCs employing the ligand Cl4py1TNH$_3$ is attributed to a lack of

purification of the ligand.

In addition, the type II material, formed with ligand 3py2TNH$_3$, has a much lower efficiency, even compared with the control. While undesired, this is consistent with the type II quantum well design, in which direct recombination does not take place. Meaning that the carriers are continuously stuck in the well, creating even less opportunities for current generation, which ultimately leads to a lower PCE.

Note that even though all ligands formed quantum wells, in type I, some carrier movement occurs given that their generation and recombination can synchronize. But in type II, this process is more prone to stop since the carriers are more frequently stabilized in the wells of different materials. Therefore, the observed trend in PCE, with the exception of the Cl4py1TNH$_3$ material, is consistent with the electronic characterization conducted before.

Therefore, it is reasonable to say that the devices prepared with the novel ligands show promise for future application of perovskite solar cells.

3.4 Single crystals

<div style="text-align: center;">

Data analysis

</div>

1. Confirming **structure of ligands** and intermediates (**NMR**)
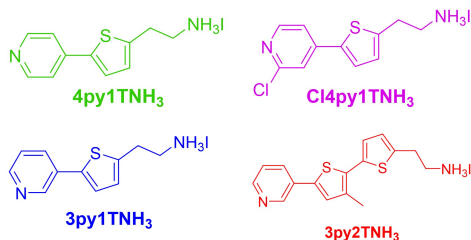
4py1TNH₃

Cl4py1TNH₃

3py1TNH₃

3py2TNH₃

2. **Characterizing** novel 2D-perovskites **thin films** via:

a. UV-Vis analysis

b. XRD analysis

c. Photoluminescence analysis

2D perovskite

3. Comparing **electronic parameters** of **perovskite solar cells**
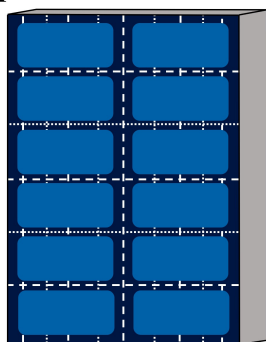
4. Confirming **2D perovskite** structure in **single crystals**

Figure 83: Data analysis - Step 4: Obtaining single crystals of novel 2D-materials

Perovskite single crystals are extremely important pieces of data in order to confirm the structure and lattice arrangement of these novel materials. However, to date, single crystals of the 2D-perovskites formed with novel pyridine-based ligands synthesized in this study have not been achieved.

4 Conclusion

This thesis has come a long way, especially when taking into account the many different areas it spans: physics, inorganic and organic chemistries and electronics.
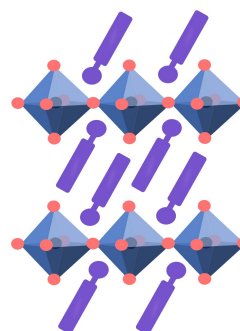
In the Introduction, a Chemistry-based view on materials science was presented. This is imporant because one of the main concepts in this field, the material's band structure, is traditionally presented from a Physics perspective, which requires a mathematical sophistication that can be overwhelming. Instead, this concept was rationalized using ideas that are familiar to chemists, such as electronegativity, energies of valence and molecular orbitals and their associated bonding and antibonding interactions. Therefore, it also helps highlight the interdisciplinary feature of materials science and the valuable contributions that each of its different branches can provide.

Next, a deeper dive into the chemical and electronic structures of metal-halide perovskites was given, so that the theoretical discussion previously introduced was tailored to the materials under investigation. Moreover, the advantages and disadvantages of the use of these semiconductors were also detailed, in light of their modern applications in solar cells. This opened up possible windows for modifications and research questions.

However, the defined purpose of this research was fully realized when the chemical composition of 2D-perovskites was presented. That is, their unique lattice arrangement provided the opportunity to use synthetic organic chemistry to design novel ligands to probe structure-function relationships between the semiconductors and their effectiveness as the primary light absorbers in solar cells. Therefore, the primary goal of this research was determined: to synthesize novel pyridine-based ligands so that 2D-perovskites, destined for solar cell applications, can be assembled.

The next step was to develop and execute a plan to synthesize the desired novel pyridine-based ligands. And according to the NMR data displayed in section 3.1, the desired structures are confirmed.

Lastly, these ligands had to be assembled into the perovskites and even though the work

was not performed by the author, presenting it and the resulting data put the synthetic chemistry into context. That is, by showing how these ligands led to the formation of novel perovskites and solar cells with promising efficiencies, made the chemical manipulations more tangible and rewarding. Most excitingly, the characterization of these materials allowed one to see that all theory developed in the Introduction was not in vain (!), since the absorption and emission spectra speak directly to the band gap and energy alignments of semiconductors.

Within materials science, this work contributes to the expansion of the ligand library available for 2D perovskites. Moreover, as they continue to be studied, more structure-function relationships will be hopefully drawn, hence advancing the understanding of perovskites and semiconductors and their possible impacts on solar cell applications.

Lastly, this work fits into a larger picture of climate change and renewable energy. As the world moves further into the consequences caused by climate change, there is an increasing need to switch to sustainable energy sources that do not rely fossil fuels. One of the most promising candidates is solar energy. It is in hopes of the more widespread use of greener solar powering that these perovskites solar cells and their materials are studied with such passion across many universities and national labs.

References

(1)   Administration, U. E. I. What is U.S. electricity generation by energy source?, 2023, `https://www.eia.gov/tools/faqs/faq.php?id=427&t=3` (accessed 09/04/2023).

(2)   NASA Scientific Consensus: Earth's Climate Is Warming, Climate change data - mention and references therein., `https://climate.nasa.gov/scientific-consensus/` (accessed 09/18/2023).

(3)   Barnes, C. et al. Climate change more than doubled the likelihood of extreme fire weather conditions in Eastern Canada, 2023, `https://mcusercontent.com/854a9a3e09405d4ab19a4a9d5/files/ba799979-2d04-ed82-4252-296e5f3e7ea0/Scientific_report_Eastern_Canada_wildfires.pdf`.

(4)   Borunda, A. Some of Canada's wildfires likely made worse by human-driven climate change, 2023, `https://www.npr.org/2023/08/22/1195154996/some-of-canadas-wildfires-likely-made-worse-by-human-driven-climate-change#:~:text=Food-,Climate%20change%20made%20some%20of%20Canada's%20wildfire%20weather%20much%20worse,according%20to%20a%20new%20study` (accessed 09/18/2023).

(5)   McGuinness, J.; Rohloff, K.; O'Shea, C. NASA Clocks July 2023 as Hottest Month on Record Ever Since 1880, 2023, `https://www.nasa.gov/press-release/nasa-clocks-july-2023-as-hottest-month-on-record-ever-since-1880` (accessed 09/18/2023).

(6)   Lenssen, N. J.; Schmidt, G. A.; Hansen, J. E.; Menne, M. J.; Persin, A.; Ruedy, R.; Zyss, D. *Journal of Geophysical Research: Atmospheres* **2019**, *124*, 6307–6326, `https://data.giss.nasa.gov/gistemp/references.html` (accessed 09/18/2023).

(7) Administration, U. E. I. The United States consumed a record amount of renewable energy in 2020, 2021, `https://www.eia.gov/todayinenergy/detail.php?id=48396` (accessed 09/04/2023).

(8) Kabir, E.; Kumar, P.; Kumar, S.; Adelodun, A. A.; Kim, K. H. *Renewable and Sustainable Energy Reviews* **2018**, *82*, 894–900, `https://www.sciencedirect.com/science/article/pii/S1364032117313485?casa_token=t49IuNIypbgAAAAA:h_9oynDXxQhrR-W5-WqdkaYwhD9N_WgWIGJGfRb4ZrQf4vHQnVR1f46bZIOhaOuUq08AHRmObA`.

(9) Office, S. E. T. Solar Investment Tax Credit: What Changed?, 2022, `https://www.energy.gov/eere/solar/articles/solar-investment-tax-credit-what-changed` (accessed 09/19/2023).

(10) Administration, U. E. I. Solar generation was 3 per cent of U.S. electricity in 2020, but we project it will be 20 per cent by 2050, 2021, `https://www.eia.gov/todayinenergy/detail.php?id=50357` (accessed 09/18/2023).

(11) Mohamed, M. A. A. In ed. by Lehmann, S.; Waer, H.; Al-Qawasmi, J., The Center for the Study of Architecture in Arab Region (CSAAR Press): 2010, `https://repository.effatuniversity.edu.sa/bitstream/handle/20.500.14131/402/006-2010_Traditional%20ways%20of%20dealing%20with%20climate%20in%20Egypt.pdf?sequence=1`.

(12) Of Energy, U. D. The history of solar, 2002, `https://www1.eere.energy.gov/solar/pdfs/solar_timeline.pdf` (accessed 09/19/2023).

(13) Chapin, D. M.; Ridge, B.; Fuller, C. S.; Pearson, C.; Pearson, G. L. Solar Energy Converting Apparatus, 1954, `https://image-ppubs.uspto.gov/dirsearch-public/print/downloadPdf/2780765`.

(14) Shockley, W.; Queisser, H. J. *Journal of Applied Physics* **1961**, *32*, 510–519, `http://metronu.ulb.ac.be/npauly/art_2014_2015/shockley_1961.pdf`.

(15) Laboratory, N. R. E. Perovskite Solar Cells, 2022, `https://www.nrel.gov/pv/perovskite-solar-cells.html#:~:text=Perovskite%20materials%20offer%20excellent%20light,cost%2C%20industry%2Dscalable%20technology.` (accessed 09/19/2023).

(16) Duffy, J. A., *Bonding, energy levels and bands in inorganic solids*; Longman Group: 1990.

(17) Yu, P. Y.; Cardona, M. In 1st ed.; Springer: 1944; Chapter 2, pp 14–101.

(18) Kittel, C., *Introduction to solid state physics*, 4th ed.; John Wiley and Sons, Inc: 1971.

(19) Miessler, G. L.; Fischer, P. J.; Tarr, D. A. In 5th ed.; Pearson: 2014; Chapter 5, pp 117–168.

(20) Yu, P. Y.; Cardona, M. In 1st ed.; Springer: 1944; Chapter 6, pp 234–332.

(21) Kim, J. Y.; Lee, J. W.; Jung, H. S.; Shin, H.; Park, N. G. *Chemical Reviews* **2020**, *120*, 7867–7918.

(22) Lin, Z.-Y.; Sun, J.; Shiring, S. B.; Dou, L.; Savoie, B. M. *ChemRxiv* **2023**, `https://chemrxiv.org/engage/chemrxiv/article-details/6439620f73c6563f14d8d2e1.`

(23) Ma, K.; Sun, J.; Atapattu, H. R.; Larson, B. W.; Yang, H.; Sun, D.; Chen, K.; Wang, K.; Lee, Y.; Tang, Y.; Bhoopalam, A.; Huang, L.; Graham, K. R.; Mei, J.; Dou, L. *Science Advances* **2023**, *9*, DOI: `10.1126/sciadv.adg0032`, `https://www.science.org/doi/10.1126/sciadv.adg0032.`

(24) Zhao, X.; Liu, T.; Loo, Y. L. *Advanced Materials* **2022**, *34*, DOI: `10.1002/adma.202105849`, `https://onlinelibrary.wiley.com/doi/epdf/10.1002/adma.202105849.`

(25) Varma, P. R. In Summary of perovskite proeprties.; Elsevier: 2018, pp 197–229.

(26)   Gao, Y.; Wei, Z.; Hsu, S. N.; Boudouris, B. W.; Dou, L. *Materials Chemistry Fron-tiers* **2020**, *4*, 3400–3418, `https://pubs.rsc.org/en/content/articlelanding/2020/qm/d0qm00233j`.

(27)   Xing, G.; Mathews, N.; Sun, S.; Lim, S. S.; Lam, Y. M.; Grätzel, M.; Mhaisalkar, S.; Sum, T. C. *Science* **2013**, *342*, 344–347, `https://pubmed.ncbi.nlm.nih.gov/24136965/`.

(28)   Kitazawa, N.; Watanabe, Y.; Nakamura, Y. *Journal of Materials Science* **2002**, *37*, 3585–3587, `https://www.scopus.com/record/display.uri?eid=2-s2.0-0036734584&origin=inward&txGid=cefd894eb404bfa787325c708826d9ce`.

(29)   Sun, J.; Wang, K.; Ma, K.; Park, J. Y.; Lin, Z.-Y.; Savoie, B. M.; Dou, L. *Journal of the American Chemical Society* **2023**, *145*, 20694–20715, `https://pubs.acs.org/doi/10.1021/jacs.3c02143`.

(30)   Chen, Y.; Sun, Y.; Peng, J.; Tang, J.; Zheng, K.; Liang, Z. *Advanced Materials* **2018**, *30*, 1703487.

(31)   Choi, W.-G.; Na, S.; Park, C.-G.; Moon, T. *Solar Energy* **2019**, *178*, 56–60, `https://www.sciencedirect.com/science/article/pii/S0038092X1831168X`.

(32)   Watthage, S. C.; Song, Z.; Phillips, A. B.; Heben, M. J. *Perovskite Photovoltaics: Basic to Advanced Concepts and Implementation* **2018**, 43–88.

(33)   Weber, D. *Zeitschrift für Naturforschung B* **1978**, *33*, 1443–1445.

(34)   Weber, D. *Zeitschrift für Naturforschung B* **1979**, *34*, 939–941.

(35)   Yamada, K.; Kawaguchi, H.; Takashi, M.; Okuda, T.; Ichiba, S. *The Chemical Society of Japan* **1990**, *63*, 2521–2525, `https://www.journal.csj.jp/doi/pdf/10.1246/bcsj.63.2521`.

(36) Philippe, B.; Jacobsson, T. J.; Correa-Baena, J. P.; Jena, N. K.; Banerjee, A.; Chakraborty, S.; Cappel, U. B.; Ahuja, R.; Hagfeldt, A.; Odelius, M.; Rensmo, H. *Journal of Physical Chemistry C* **2017**, *121*, VBM comes from I 5p/Br 4p, 26655–26666.

(37) Targhi, F. F.; Jalili, Y. S.; Kanjouri, F. *Results in Physics* **2018**, *10*, 616–627.

(38) Clementi, E.; Raimondi, D. L. *The Journal of Chemical Physics* **1963**, *38*, 2686–2689.

(39) Clementi, E.; Raimondi, D. L.; Reinhardt, W. P. *The Journal of Chemical Physics* **1967**, *47*, 1300–1307.

(40) Kojima, A.; Teshima, K.; Shirai, Y.; Miyasaka, T. *Journal of the American Chemical Society* **2009**, *131*, 6050–6051, `https://pubs.acs.org/doi/10.1021/ja809598r`.

(41) William, E. *University Of Science And Technology Of China Team Breaks The Certified World Record For The Steady-State Efficiency Of Perovskite Cells-IT HOME*; tech. rep.; University of Science and Technology of China, 2023.

(42) Saparov, B.; Mitzi, D. B. *Chemical Reviews* **2016**, *116*, 4558–4596, `https://pubs.acs.org/doi/10.1021/acs.chemrev.5b00715`.

(43) Snaith, H. J. *The Journal of Physical Chemistry Letters* **2013**, *4*, 3623–3630, `https://pubs.acs.org/doi/10.1021/jz4020162`.

(44) Espinosa, N.; Serrano-Luján, L.; Urbina, A.; Krebs, F. C. *Solar Energy Materials and Solar Cells* **2015**, *137*, 303–310.

(45) Celik, I.; Song, Z.; Cimaroli, A. J.; Yan, Y.; Heben, M. J.; Apul, D. *Solar Energy Materials and Solar Cells* **2016**, *156*, 157–169.

(46) Lin, Y.; Bai, Y.; Fang, Y.; Chen, Z.; Yang, S.; Zheng, X.; Tang, S.; Liu, Y.; Zhao, J.; Huang, J. *The Journal of Physical Chemistry Letters* **2018**, *9*, 654–658, `https://pubs.acs.org/doi/10.1021/acs.jpclett.7b02679`.

(47)   Chen, B.; Wang, S.; Song, Y.; Li, C.; Hao, F. *Chemical Engineering Journal* **2022**, *430*, I need to get this from Science Direct, 132701.

(48)   Ahangharnejhad, R. H.; Song, Z.; Mariam, T.; Gardner, J. J.; Liyanage, G. K.; Almutawah, Z. S.; Anwar, B. M.; Junda, M.; Podraza, N. J.; Phillips, A. B.; Yan, Y.; Heben, M. J. *ACS Applied Energy Materials* **2021**, *4*, 7571–7578, `https://pubs.acs.org/doi/epdf/10.1021/acsaem.1c00816`.

(49)   Jiang, Q.; Rebollar, D.; Gong, J.; Piacentino, E. L.; Zheng, C.; Xu, T. *Angewandte Chemie* **2015**, *127*, 7727–7730.

(50)   Boyd, C. C.; Cheacharoen, R.; Leijtens, T.; McGehee, M. D. *Chemical Reviews* **2019**, *119*, 3418–3451, `https://pubs.acs.org/doi/epdf/10.1021/acs.chemrev.8b00336`.

(51)   Jin, I. S.; Park, S. H.; Kim, K. S.; Jung, J. W. *Journal of Alloys and Compounds* **2020**, *847*, 156512, `https://www.sciencedirect.com/science/article/abs/pii/S0925838820328760`.

(52)   Li, G.; Song, J.; Wu, J.; Song, Z.; Wang, X.; Sun, W.; Fan, L.; Lin, J.; Huang, M.; Lan, Z.; Gao, P. *ACS Energy Letters* **2021**, *6*, 3614–3623, `https://pubs.acs.org/doi/10.1021/acsenergylett.1c01649`.

(53)   *Nature Chemistry* **2019**, *11*, 1151–1157, `https://www.nature.com/articles/s41557-019-0354-2`.

(54)   Duffy, J. A. In 1st ed.; Longman Scientific and Technical: 1990; Chapter 7, pp 174–191.

(55)   Bastard, G., *Wave mechanics applied to semiconductor heterostructures*, 1st ed.; Halsted Press: 1988.

(56)   Rombach, F. M.; Haque, S. A.; Macdonald, T. J. *Energy and Environmental Science* **2021**, *14*, 5161–5190, `https://pubs.rsc.org/en/content/articlepdf/2021/ee/d1ee02095a`.

(57) Lucarelli, G.; Brown, T. M. *Frontiers in Materials* **2019**, *6*, DOI: `10.3389/fmats.2019.00310`.

(58) Dkhili, M.; Lucarelli, G.; Rossi, F. D.; Taheri, B.; Hammedi, K.; Ezzaouia, H.; Brunetti, F.; Brown, T. M. *ACS Applied Energy Materials* **2022**, *5*, 4096–4107.

(59) Sun, J.; Ma, K.; Lin, Z.-Y.; Tang, Y.; Varadharajan, D.; Chen, A. X.; Atapattu, H. R.; Lee, Y. H.; Chen, K.; Boudouris, B. W.; Graham, K. R.; Lipomi, D. J.; Mei, J.; Savoie, B. M.; Dou, L. *Advanced Materials* **2023**, *35*, DOI: `10.1002/adma.202300647`, `https://onlinelibrary.wiley.com/doi/10.1002/adma.202300647`.

(60) Floyd, T. L.; Buchla, D. M.; Snyder, G. D. In 9th ed., Electronics TB has the definitions for conductors, insulators and semiconductors in the beginning of Chapter 2. ¡br/¿Also has some stuff on Solar panels in page 38. Cjapter 2 voltage section¡br/¿Also has IV curve explanation; Pearson: 2021.

(61) Hong, X.; Ishihara, T.; Nurmikko, A. U. *The American Physical Society* **1992**, *45*, 6961–6964.

(62) Mao, L.; Wu, Y.; Stoumpos, C. C.; Wasielewski, M. R.; Kanatzidis, M. G. *Journal of the American Chemical Society* **2017**, *139*, 5210–5215.

(63) Chen, Z.; Liu, M.; Li, Z.; Shi, T.; Yang, Y.; Yip, H. L.; Cao, Y. *iScience* **2018**, *9*, 337–346.

(64) Mishra, A. et al. *Chemistry of Materials* **2021**, *33*, 6412–6420.

(65) Lédée, F.; Audebert, P.; Trippé-Allard, G.; Galmiche, L.; Garrot, D.; Marrot, J.; Lauret, J. S.; Deleporte, E.; Katan, C.; Even, J.; Quarti, C. *Materials Horizons* **2021**, *8*, 1547–1560.

(66) Mao, L.; Ke, W.; Pedesseau, L.; Wu, Y.; Katan, C.; Even, J.; Wasielewski, M. R.; Stoumpos, C. C.; Kanatzidis, M. G. *Journal of the American Chemical Society* **2018**, *140*, I was given permission to use one of the Figures on Nov 11th. See

email from Professor from Northwestern Uni (sent from Drew), 3775–3783, `https://pubs.acs.org/doi/10.1021/jacs.8b00542`.

(67) Ma, K.; Atapattu, H. R.; Zhao, Q.; Gao, Y.; Finkenauer, B. P.; Wang, K.; Chen, K.; Park, S. M.; Coffey, A. H.; Zhu, C.; Huang, L.; Graham, K. R.; Mei, J.; Dou, L. *Advanced Materials* **2021**, *33*, DOI: `10.1002/adma.202100791`.

(68) Klein, D. R. In 2nd ed.; Wiley: 2015; Chapter 18, pp 832–873.

(69) Prize, T. N. The Nobel Prize in Chemistry in 2010, `https://www.nobelprize.org/prizes/chemistry/2010/summary/` (accessed 09/25/2023).

(70) De. Meijere, A.; Diederich, F. In Protecting group part - Protection of the amino group with a t-butoxycarbonyl (Boc), benzyloxycarbonyl (Cbz), or p-methoxybenzyloxycarbonyl group (191) allows smooth hydroboration of allylic amines with 9-BBN and subsequent cross-coupling with organic halides for the synthesis of amine derivatives [254, 256, 274]¡br/¿¡br/¿Page 45¡br/¿; Wiley-VCH: 2004, p 916, `https://onlinelibrary.wiley.com/doi/epdf/10.1002/9783527619535.ch2`.

(71) Miyaura, N.; Yamada, K.; Suzuki, A. *Tetrahedron Letters* **1979**, 3437–3440, `http://hdl.handle.net/2115/44006`.

(72) Milstein, D.; Stille, J. K. *Journal of the American Chemical Society* **1978**, *100*, 3636–3638.

(73) Cordovilla, C.; Bartolomé, C.; Martínez-Ilarduya, J. M.; Espinet, P. *ACS Catalysis* **2015**, *5*, 3040–3053.

(74) Barakat, M. Z.; Mousa, G. M. *Journal of Pharmacy and Pharmacology* **1952**, *4*, A possible mechanism is on your tablet., 115–117, `https://onlinelibrary.wiley.com/doi/abs/10.1111/j.2042-7158.1952.tb13121.x#:~:text=The%20fact%20that%20N%2Dbromosuccinimide,the%20detection%20of%20these%20compounds.&text=N%2DBromosuccinimide%20(2%20g.,benzyl%20alcohol%20(4%20ml.).`

(75) Panda, J.; Sahoo, J.; Dutta, J.; Biswal, H. S.; Sahoo, G. Spectroscopic and Computational Study of Organocatalytic Umpolung of Bromocations: An Accelerated Stereoselective Dibromination Protocol, 2023, `https://chemrxiv.org/engage/chemrxiv/article-details/63c2c2cb1f125840d19dba28`.

(76) Gilman, H.; Shirley, D. A. *Journal of the American Chemical Society* **1949**, *71*, 1870–1871.

(77) Dkhili, M.; Lucarelli, G.; Rossi, F. D.; Taheri, B.; Hammedi, K.; Ezzaouia, H.; Brunetti, F.; Brown, T. M. *ACS Applied Energy Materials* **2022**, *5*, 4096–4107.

(78) Liu, J.; Liu, W.; Aydin, E.; Harrison, G. T.; Isikgor, F. H.; Yang, X.; Subbiah, A. S.; Wolf, S. D. *ACS Applied Materials and Interfaces* **2020**, *12*, 23874–23884, `https://pubs.acs.org/doi/full/10.1021/acsami.0c03660`.

(79) Liu, J.; Liu, W.; Aydin, E.; Harrison, G. T.; Isikgor, F. H.; Yang, X.; Subbiah, A. S.; Wolf, S. D. *ACS Applied Materials and Interfaces* **2020**, *12*, 23874–23884, `https://www.nature.com/articles/26936`.

(80) Mott, N. F.; Gurney, R. W., *Electronic processes in ionic crystals*, 1st ed.; Oxford University Press: 1940.

(81) Jain, A.; Kapoor, A. *Solar Energy Materials and Solar Cells* **2004**, *81*, 269–277.

(82) Solak, E. K.; Irmak, E. *RSC Advances* **2023**, *13*, 12244–12269.

(83) Fulmer, G. R.; Miller, A. J.; Sherden, N. H.; Gottlieb, H. E.; Nudelman, A.; Stoltz, B. M.; Bercaw, J. E.; Goldberg, K. I. *Organometallics* **2010**, *29*, 2176–2179, `https://pubs.acs.org/doi/10.1021/om100106e`.

(84) Klein, D. R. In 2nd ed.; Wiley: 2015; Chapter 23, pp 1102–1150.

(85) Makuła, P.; Pacia, M.; Macyk, W. *The Journal of Physical Chemistry Letters* **2018**, *9*, 6814–6817, `https://pubs.acs.org/doi/10.1021/acs.jpclett.8b02892`.

(86) Skoog, D. A.; Holler, F. J.; Crouch, S. R. In 7th ed.; Cengage Learning: 2018; Chapter 15, pp 361–388.

6 Appendix

6.1 Remaining NMR spectra

Below are the remaining the NMR spectra for the molecules Cl4py1TBoc, Cl4py1TNH$_3$, 3py1TBoc and 3py1TNH$_3$. The coupling information, chemical shifts and integration values are present in the Methods section (2.1) and a sample analysis was also described in the Results and Discussion section (section 3.1). And the NMR for one of the starting materials: 1-bromo-2-mehylthiophene.
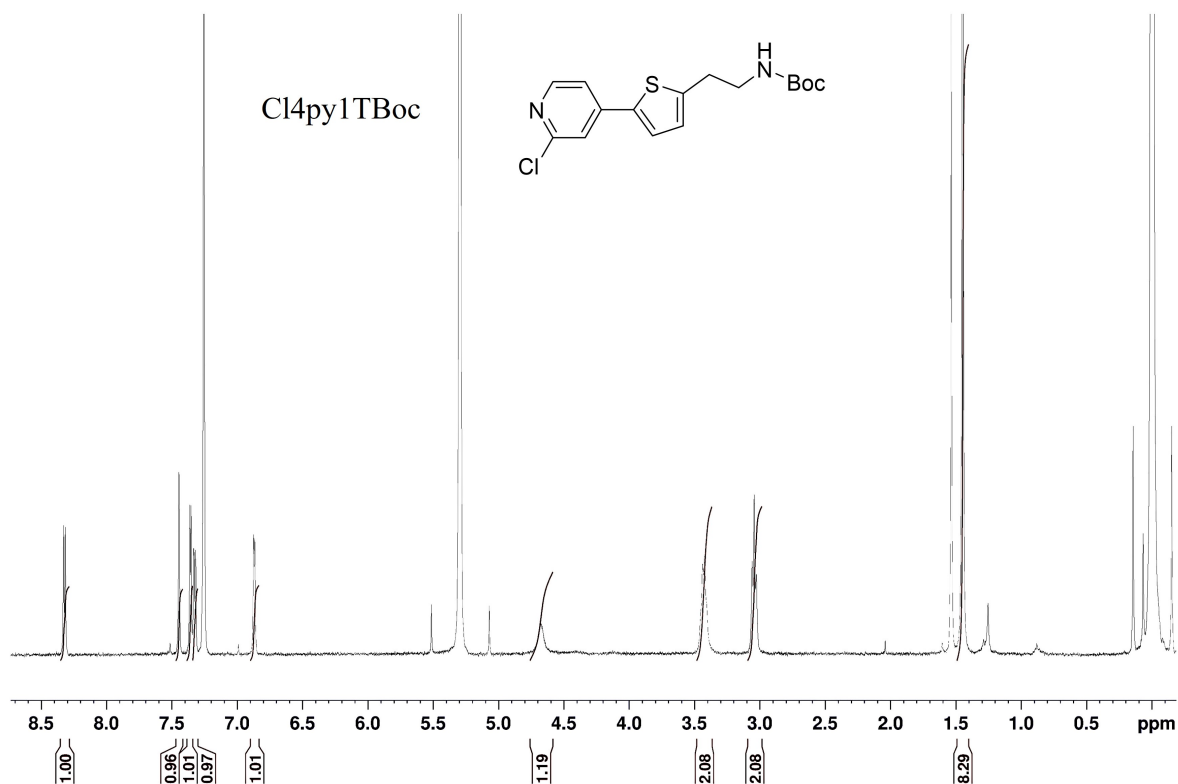

Figure 84: Full NMR spectrum for the molecule Cl4py1TBoc. This is intended to show all peaks present in the scan, considering possible impurities, standards and solvent peaks (not integrated). Individual hydrogens have not been assigned, but the number of peaks and integration values indicate that the desired molecule was synthesized.
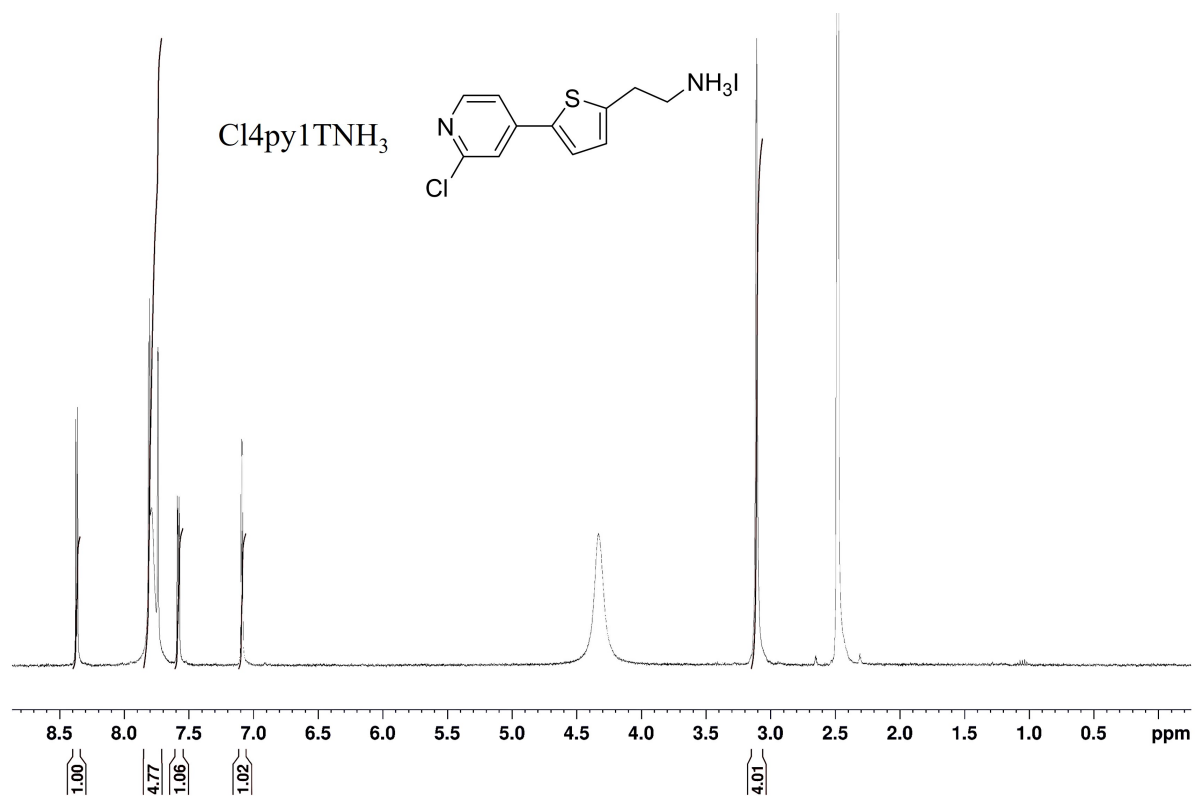
Figure 85: Full NMR spectrum for the molecule Cl4py1TNH$_3$. This is intended to show all peaks present in the scan, considering possible impurities, standards and solvent peaks (not integrated). Individual hydrogens have not been assigned, but the number of peaks and integration values indicate that the desired molecule was synthesized.
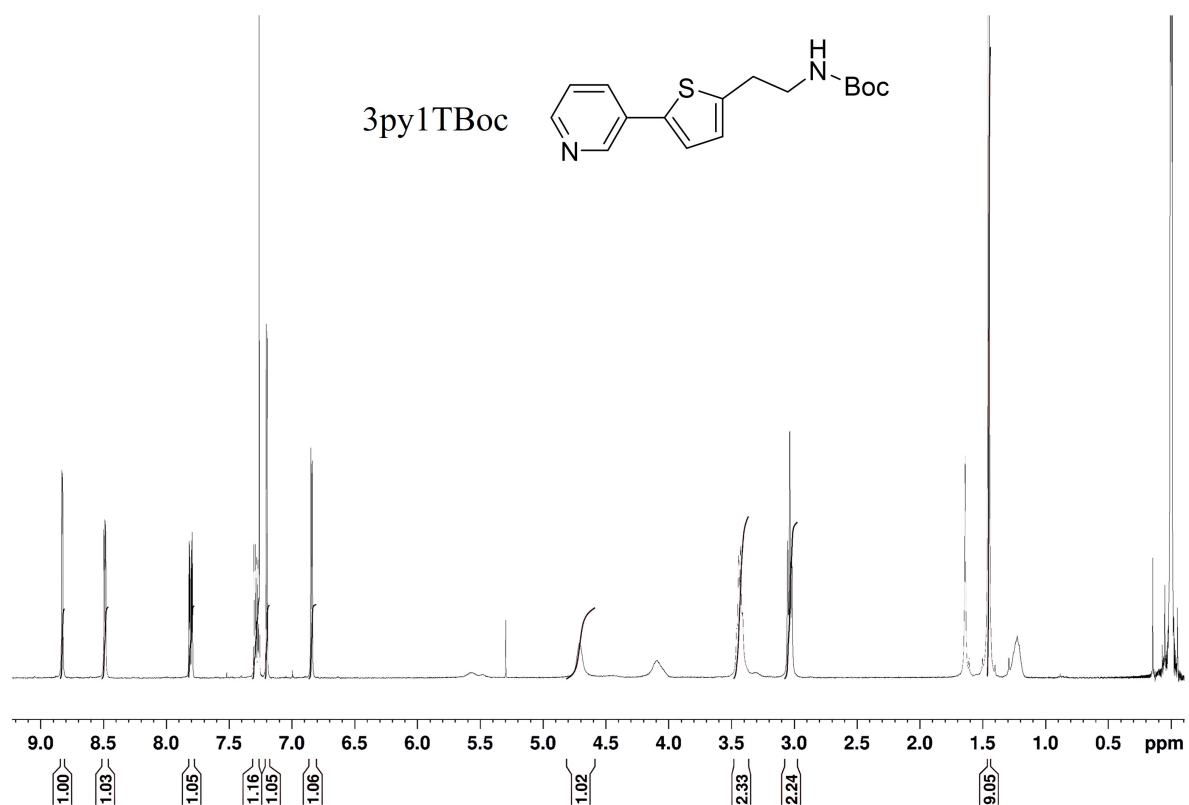
Figure 86: Full NMR spectrum for the molecule 3py1TBoc. This is intended to show all peaks present in the scan, considering possible impurities, standards and solvent peaks (not integrated). Individual hydrogens have not been assigned, but the number of peaks and integration values indicate that the desired molecule was synthesized.
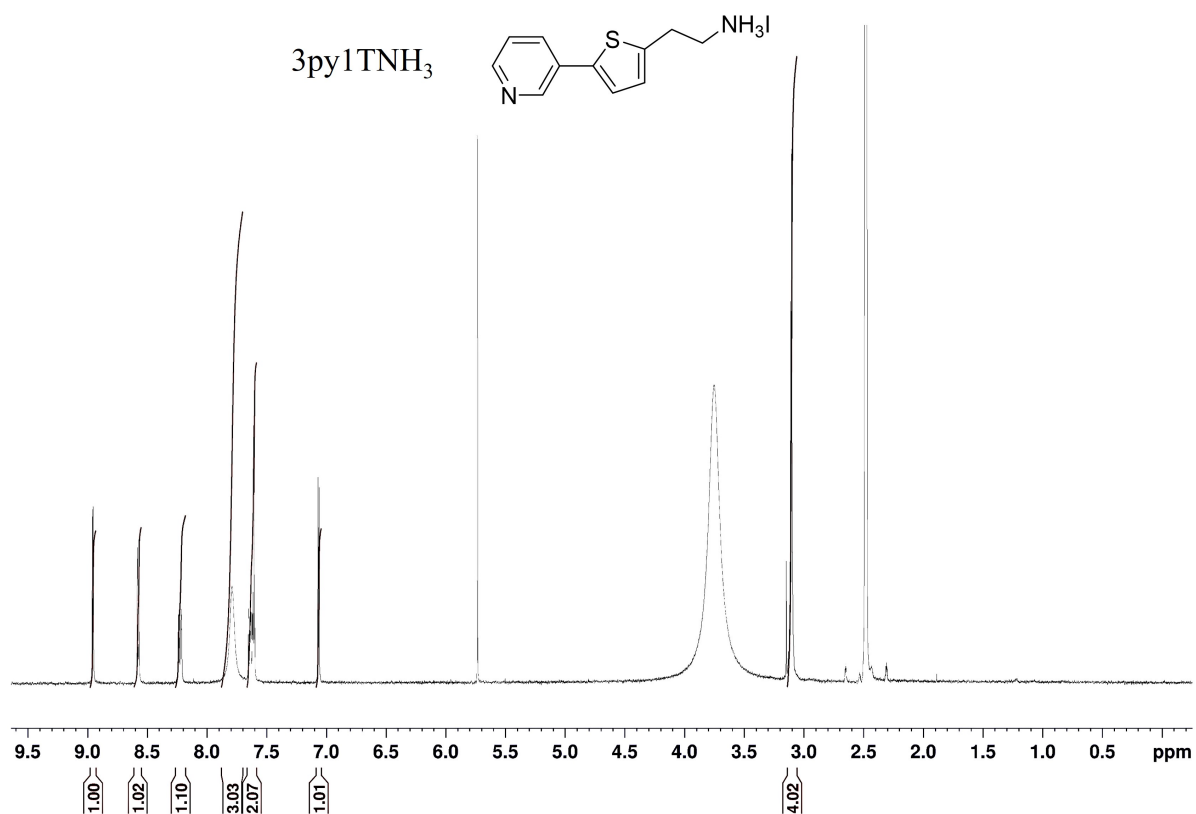
Figure 87: Full NMR spectrum for the molecule 3py1TNH$_3$. This is intended to show all peaks present in the scan, considering possible impurities, standards and solvent peaks (not integrated). Individual hydrogens have not been assigned, but the number of peaks and integration values indicate that the desired molecule was synthesized.
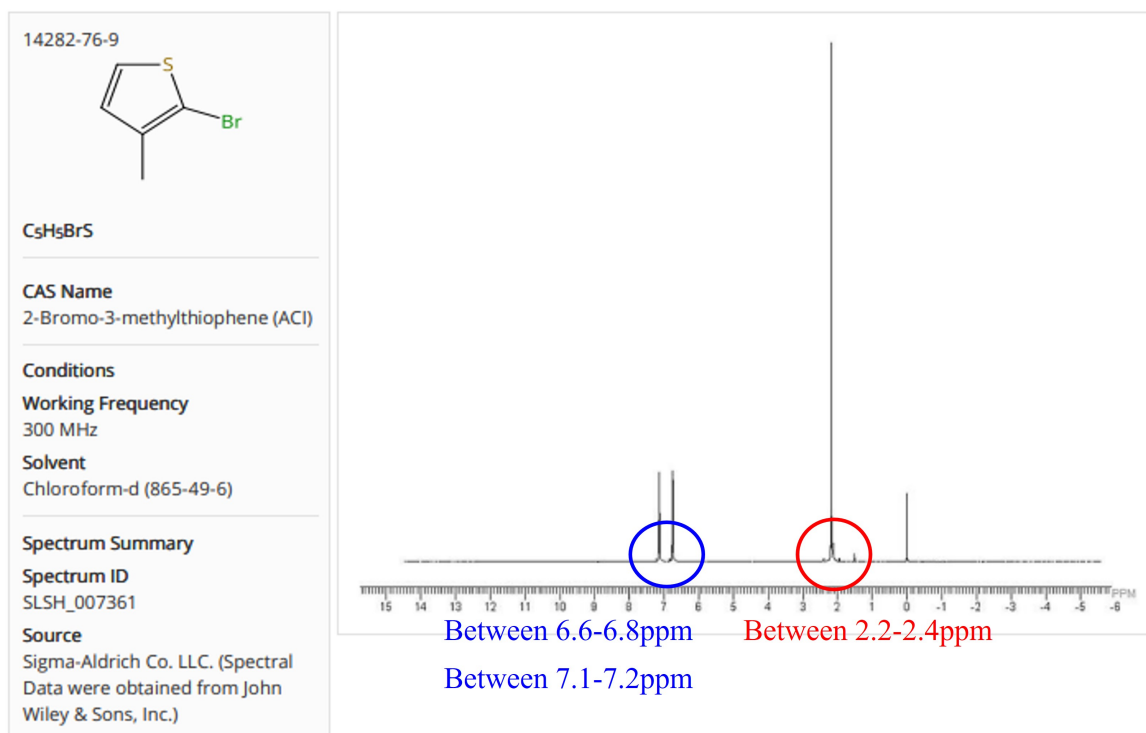
Figure 88: NMR of one commercial staring material: 1-bromo-2-methylthiophene. This spectrum was obtained directly from SciFinder so that the chemical shift of the peaks were determined. Their range has been added to the spectrum.

6.2   You're curious!

Upon writing this document, I came across mechanistic details and several different questions (and answers) that were not actually necessary to include in the main text. That is, they were not fundamental to get my message of synthesis, mechanism or analysis across. Nonetheless, I thought they were cool, so I took the liberty to include them here for fun.

The first one happened when I tried to break down the mechanism of the N-bromosuccinimide reaction, in the second step of the synthesis of Br1TBoc shown in Figure 36. As noted, the reaction could take two different pathways: either through radical formation or electrophilic aromatic substitution. In the caption of Figure 38, I mention that the attack on the bromine atom by the thiophene is due to the umpolung effect. And this is actually quite interesting! This effect was discovered by Dieter Seebach, a German chemist, and umpolung stands for "inverse polarity". That is: normally one would expect that a N-Br bond would be close to non-polar covalent, since the electronegativity difference between N and Br is actually small (if we use the values from either Pauli or Allred-Rochow electronegativity tables). And this is bad news, since in EAS reactions, a very potent electrophile must be present, otherwise the aromatic ring will not attack (too great of an energy barrier to form sigma complex). However, it all comes down to the resonance structure presented in Figure 38A, where the oxygen atoms draw electron density from the nitrogen. This effectively leads to a distortion of the "non-polar covalent" bond between N and Br, in which the electron distribution is skewed toward the nitrogen. This creates an umpolung effect, *greatly* polarizing the bromine. Let me say that again: an atom which is usually considered to hold negative charges well has become a great electrophile, due to those amide bonds. How cool. You can check out an electrostatic potential map in this paper: reference number [75]. So, because of the umpolung effect, the bromine becomes a suitable electrophile for EAS, which allowed me to synthesize Br1TBoc, and eventually the desired ligands for new 2D perovskites.

Another problem that could be potentially faced in this reaction is the conversion of an unprotected amine by NBS. In the actual synthesis, this was taken care of due to the presence of the Boc protecting group, but I thought it would be fun to include the mechanism of the side reaction. It would likely proceed through radical intermediates, oxidizing the amine to an imine and then converting in to an aldehyde [74]. The curved arrow formalism is presented in Figure 89.
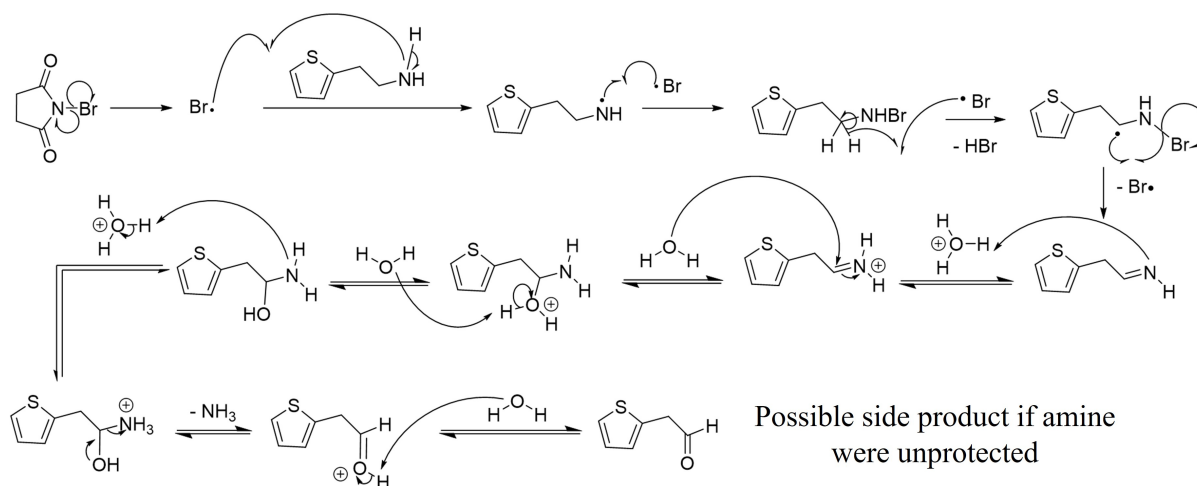

Figure 89: Mechanism NBS side product reaction. As noted, the reaction would start via a radical addition of bromine to the amine, which would be oxidized to an imine. The conversion from imine to aldehyde follows an acid-catalyzed mechanism, since one of the by-products of the reaction is hydrobromic acid. Water was employed to promote all necessary proton transfers, and it is technically available in the reaction, since none of the materials (flask and solvents) were scrupulously dried. The mechanism follow the path proposed by Barakat & Mousa [74]

In the same way, the reaction employing N-iodosuccinimide (NIS), follows the same principles. However, the effect is even more pronounced since the reaction is carried out in the presence of acetic acid. That is, in the mechanism, displayed in Figure , one of the carbonyls become protonated, which leads to a resonance structure with only one positive charge.
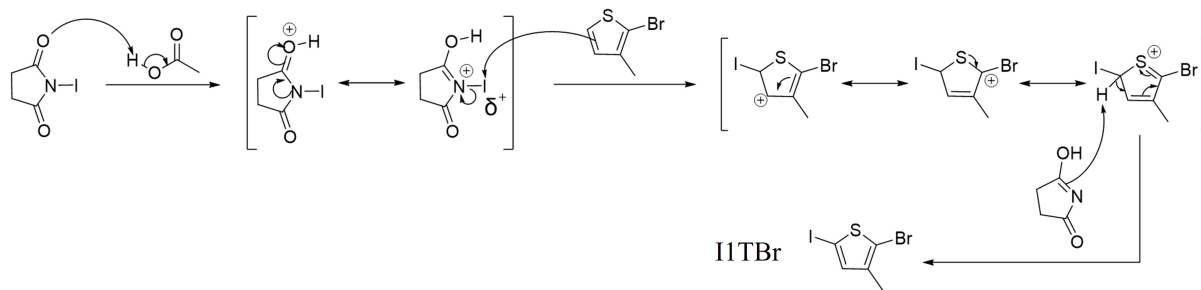
Figure 90: Mechanism NIS reaction employed in the synthesis of I1TBr. In the first step, the acetic acid protonates the succinimide, further driving the umpolung effect present in the iodine [75]. Next, the electronically-rich thiophene derivative attacks the halogen leading to the formation of a sigma complex. The last proton transfer restores the aromaticity (driving force of reaction) and creates the desired product.